

2023-05-01

A Method For Measuring The Spectral Emissivity Of Metal Powders At Different Temperatures And Applications In Laser Powder Bed Fusion

Emmanuel Levario
University of Texas at El Paso

Follow this and additional works at: https://scholarworks.utep.edu/open_etd



Part of the [Mechanical Engineering Commons](#)

Recommended Citation

Levario, Emmanuel, "A Method For Measuring The Spectral Emissivity Of Metal Powders At Different Temperatures And Applications In Laser Powder Bed Fusion" (2023). *Open Access Theses & Dissertations*. 3814.

https://scholarworks.utep.edu/open_etd/3814

This is brought to you for free and open access by ScholarWorks@UTEP. It has been accepted for inclusion in Open Access Theses & Dissertations by an authorized administrator of ScholarWorks@UTEP. For more information, please contact lweber@utep.edu.

A METHOD FOR MEASURING THE SPECTRAL EMISSIVITY OF METAL POWDERS AT
DIFFERENT TEMPERATURES AND APPLICATIONS IN LASER POWDER BED FUSION

EMMANUEL LEVARIO

Master's Program in Mechanical Engineering

APPROVED:

Ryan B. Wicker, Ph.D., Chair

Cesar A. Terrazas, Ph.D.

Amit J. Lopes, Ph.D.

Stephen L. Crites, Jr., Ph.D.
Dean of the Graduate School

Copyright ©

by

Emmanuel Levario

2023

DEDICATION

This thesis is dedicated to my friends and family, who, without a doubt, this would not be possible without. To my parents and siblings for providing the foundation for all my achievements, to my extended family for their endless support, to my friends and to those I love, thanks for sticking around.

A METHOD FOR MEASURING THE SPECTRAL EMISSIVITY OF METAL POWDERS AT
DIFFERENT TEMPERATURES AND APPLICATIONS IN LASER POWDER BED FUSION

by

EMMANUEL LEVARIO, B.S. METALLURGICAL AND MATERIALS ENGINEERING

THESIS

Presented to the Faculty of the Graduate School of

The University of Texas at El Paso

in Partial Fulfillment

of the Requirements

for the Degree of

MASTER OF SCIENCE

Department of Aerospace and Mechanical Engineering

THE UNIVERSITY OF TEXAS AT EL PASO

May 2023

ACKNOWLEDGEMENTS

An acknowledgement of the Keck Center is an acknowledgement of Dr. Wicker whose guidance and opportunity led me somewhere I never thought I would be, fulfilling a passion that has grown since being a part of the lab. The valuable resources at the Keck Center, including the staff and advisors, are what allowed this research to be possible. I would also like to thank those who guided me, particularly within the Keck Center. To Cesar A. Terrazas, for being one of the first people I communicated with regarding an opportunity at the Keck Center and then guiding me well into my degree, and finally, continuing his support even when it wasn't as convenient. Alfonso Fernandez, the relatively short amount of time we spent together was more than enough to ignite the passion I now have for this field of research. To Ralph Felice whose weekly collaboration with the Keck Center not only advanced the research but helped motivate it as well. Jorge Mireles, who made the extra effort to not only be one of the most knowledgeable advisors I've ever had, but one I could look forward to speaking or meeting with. To Amit Lopes for taking valuable time to serve on my thesis committee, and to my parents Manuel Levario and Veronica Nunez for supporting the decisions I made to get to this point even at the cost of time spent with family. I only hope these efforts can justify time lost with a bright future to look forward to.

ABSTRACT

Radiation thermometry monitoring methods used in powder bed fusion additive manufacturing (PBF-AM) are becoming increasingly more popular for quality assurance and repeatability. The dynamic nature of the PBF process and a lack of accuracy of metrics being captured for temperature monitoring lend great difficulty in the successful implementation of in-situ monitoring. There is currently no data on the emissivity, a metric used in non-contact temperature measurements, for metal powders used in AM. This work describes a method for measuring the spectral emissivity for metal powder sizes commonly used in AM using a multi-wavelength (MW), FMPI Spectropyrometer, calibrated within the spectral range of 1080nm to 1650nm to determine the feasibility of implementing IR thermography to capture true temperature measurements *in situ* and provide new information for metal-based AM process simulations and process parameter optimization. The method was developed utilizing an inert glovebox environment and a custom design of an induction heater. The focus of this research was to understand the emissive behavior of metal AM powders at different temperatures using MW pyrometry as a characterization tool. This was done by employing a multi-wavelength pyrometer, internally designed heater, and a glovebox. The objectives of this research can be described as developing an experimental setup and procedure that:

- (1) Mitigates, or eliminates, radiative environment influence
- (2) Captures the spectral emissivity of metal powders used in AM, using Inconel 718 powders at different temperatures utilizing a multi-wavelength pyrometer
- (3) Provides emissivity/absorptivity data and determines the feasibility of implementing infrared thermography in laser powder bed fusion processes

Initially, a custom design of an LC-150 Standard Glovebox System (LC Technology Solutions, MA, USA) was made to include two viewports at the top of the system that would allow for a direct line of sight for the pyrometer. A fixture attached to one of the viewports housed the pyrometer's optic with a silicon carbide tube affixed to the other end that extended down towards the target (powder). This unobstructed line of sight allowed for the SpectroPyrometer from FAR Associates (Macedonia, OH, USA) to be positioned normal to the sample surface. Prior to the heating of the powders, a calibration using a NIST traceable blackbody was performed. Measurements of three different powder diameter ranges of Inconel 718 (15-53 μm , 45-105 μm , and 45-150 μm) using their apparent and tap densities were captured as they were progressively heated in steps of 400°C, then 500°C, and finally 600°C. Values of the spectral emissivity captured during experimentation were like those of the Thermophysical Properties Research Center (TPRC) Data Series Vol. 7, the largest database of emissivity values, and reasons for deviation are given within the work. The results showed instances in which a graybody assumption would be valid, an assumption (along with the actual value for emissivity) needed for accurate temperature measurements via IR thermography. Future work will include a higher range of temperatures and different powder alloys commonly used in PBF-AM.

TABLE OF CONTENTS

DEDICATION.....	iii
ACKNOWLEDGEMENTS.....	v
ABSTRACT.....	vi
TABLE OF CONTENTS.....	viii
LIST OF TABLES.....	x
LIST OF FIGURES.....	xi
CHAPTER 1: INTRODUCTION.....	1
1.1 Project Overview.....	1
1.2 W.M. Keck Center for 3D Innovation.....	2
1.3 Additive Manufacturing.....	3
1.4 Research Motivation.....	4
1.5 Summary of Results.....	6
1.6 Thesis Outline.....	8
CHAPTER 2: LITERATURE REVIEW.....	9
2.1 Additive Manufacturing.....	9
2.2 Heat Transfer.....	11
2.3 Radiation Properties of Surfaces.....	15
2.4 Thermal Emission.....	20
2.5 Blackbody Radiation.....	22
2.6 Pyrometry.....	23
2.7 Process Monitoring.....	28
CHAPTER 3: METHODOLOGY AND PROCEDURES.....	33
3.1 Introduction.....	33
3.2 Material.....	33
3.3 Heater.....	39
3.4 FMPI Measurement Methodology.....	52
3.5 FMPI Calibration.....	53
3.6 Experimental Setup.....	57

CHAPTER 4: RESULTS AND DISCUSSIONS	62
4.1 Introduction.....	62
4.2 Data Analysis Methods.....	63
4.3 Order of Experiments.....	64
4.4 Particle Size Distribution.....	70
4.5 Silicon Carbide Tube Influence	71
4.6 Emissivity Results.....	74
CHAPTER 5: INTEGRATION OF A MULTI-WAVELENGTH PYROMETER AND L-PBF MACHINE.....	108
5.1 Integration of Tertiary Scan Head and Pyrometer	108
5.2 Calibration.....	118
5.3 Demonstration of Data Acquisition	120
PCHAPTER 6: CONCLUSIONS AND RECOMMENDATIONS.....	126
6.1 Conclusions.....	126
6.2 Recommendations.....	129
REFERENCES	131
VITA.....	140

LIST OF TABLES

Table 1.1 Size distribution for powders according to manufacturer.....	7
Table 3.1 Inconel 718 elements and their percentages for PSD - 1 and PSD - 2	37
Table 4.1 Numbers assigned to each experiment run	64
Table 4.2 Output of random sequence generator	66
Table 4.3 Output sequence of experiments for other operators	67
Table 4.4 Numbers assigned to each operator/PSD/Run combination	68
Table 4.5 Order of experiments for each operator/PSD combination	69
Table 4.6 Average signal strength for each acquisition of data	75
Table 4.7 Results for separate operator run for each sample preparation method.....	76
Table 4.8 Temperatures reached for PSD – 1	77
Table 4.9 Hypothesis testing results for chi-squared test	78
Table 4.10 Results of Tukey's HSD test calculated in R-studio	88
Table 4.11 Results of Tukey HSD test calculated in R-studio	90
Table 4.12 Average temperatures of locations	93
Table 4.13 Tukey's HSD test results using R-studio	95
Table 4.14 Results of Bartlett test.....	96
Table 4.15 T.test results comparing sample preparation methods.....	97
Table 4.16 Max temperatures reached during data acquisition for PSD - 1 experiment runs	103
Table 4.17 Results of emissivity values measured from different operators	103
Table 4.18 Results of two-sample t-test.....	106

LIST OF FIGURES

Figure 1.1 General AM workflow	4
Figure 2.1 The absorption, reflection, and transmission of incident radiant energy by a material	17
Figure 2.2 Blackbody spectrum at different temperatures.....	21
Figure 2.3 Illustration of a blackbody cavity	22
Figure 2.4 Pyrometers and the number of wavelengths they utilize.....	25
Figure 2.5 FMPI schematic; US patent 5772323 and 6379038B (Felice, 2012).....	28
Figure 2.6 e.g., Co-axial setup for laser energy source.....	29
Figure 2.7 e.g., Off-axis setup for PBF process (Fernandez et al. 2021).....	29
Figure 3.1 SEM image of PSD - 1 at 150x	35
Figure 3.2 SEM image of PSD - 2 at 150x	35
Figure 3.3 SEM image of PSD - 3 at 150x	36
Figure 3.4 Image of tungsten filament emitting while current is passed through.....	40
Figure 3.5 Heater components and assembly	41
Figure 3.6 Blown-up image of CAD for original heater design	41
Figure 3.7 Illustration of influence from top hat.....	42
Figure 3.8 Image of crucible and CAD w/ dimensions	43
Figure 3.9 IR image of heater with heated sample	44
Figure 3.10 Illustration showing emission and reflection interaction within glovebox	45
Figure 3.11 CAD image of assembled SiC Tube Holder/Optic Fixture	47
Figure 3.12 Assembly images of optic fixture.....	49
Figure 3.13 Fixture with and without supporting the SiC tube	50
Figure 3.14 CAD and dimensions of pyrometer optic assembly	52

Figure 3.15 Orientation and placement of pyrometer optic, fixture, and SiC tube in glovebox...	52
Figure 3.16 Optical alignment of pyrometer alignment laser and blackbody aperture	54
Figure 3.17 Illustration of FMPI calibration setup	55
Figure 3.18 Image of aperture influence experiment.....	56
Figure 3.19 Pyrometer optic/SiC tube fixture affixed to optic	56
Figure 3.20 Hall Flowmeter with funnel and crucibles	57
Figure 3.21 Fully assembled FMPI optic fixture and SiC tube holder	58
Figure 3.22 Aligning of pyrometer optic and powder surface.....	59
Figure 3.23 Alignment of laser with target.....	59
Figure 3.24 Fully assembled fixture and tube with alignment laser visibly unobstructed	60
Figure 4.1 Example of .log and .DAT files extracted from FMPI and put into Excel.....	63
Figure 4.2 Particle size distribution results for each powder.....	70
Figure 4.3 Powder surface temp. v SiC tube temp. for PSD – 2 (Apparent).....	72
Figure 4.4 Powder surface temp. v SiC tube temp. for PSD – 3 (Apparent).....	72
Figure 4.5 Powder surface temp. v SiC tube temp. for PSD – 3 (Tap).....	73
Figure 4.6 Powder surface temp. v SiC tube temp. for PSD - 1 (Tap)	73
Figure 4.7 Box and whisker plots of all values for each particle size distribution.....	77
Figure 4.8 Box and whisker plots excluding outliers	79
Figure 4.9 Depth analysis image of PSD - 1 tap density surface at 150x.....	81
Figure 4.10 Depth analysis image of PSD - 2 tap density surface at 150x.....	81
Figure 4.11 Depth analysis image of PSD - 3 tap density surface at 150x.....	82
Figure 4.12 Depth analysis image of PSD - 1 apparent density surface at 150x.....	83
Figure 4.13 Depth analysis image of PSD - 2 apparent density surface at 150x.....	84

Figure 4.14 Depth analysis image of PSD - 3 apparent density surface at 150x	84
Figure 4.15 Plot of emissivity vs PSD	86
Figure 4.16 Plot of Tukey's HSD test results for run comparison	88
Figure 4.17 Plot of Tukey's HSD test results for temperature comparison	90
Figure 4.18 Confidence interval plot for emissivity at each temperature.....	91
Figure 4.19 Thermal analysis w/ thermal gradient legend.....	92
Figure 4.20 Measurement locations on sample surface	93
Figure 4.21 Plot of Tukey's HSD test for particle size distribution.....	95
Figure 4.22 Illustration of waviness and surface roughness.....	98
Figure 4.23 PSD - 1 apparent density depth analysis image highlighting artificial cavity.....	99
Figure 4.24 .DAT file plotted for PSD - 1 at 400°C, for each sample preparation and 1 minute into data acquisition	100
Figure 4.25 .DAT file plotted for PSD - 1 at 500°C, for each sample preparation and 1 minute into data acquisition	100
Figure 4.26 .DAT file plotted for PSD - 1 at 600°C, for each sample preparation and 1 minute into data acquisition	101
Figure 4.27 Results of Probability Plot.....	104
Figure 4.28 Results of Analysis of Variance	105
Figure 4.29 Interval Plot for Analysis of Means.....	106
Figure 5.1 Image of mirror reflectivity setup.....	109
Figure 5.2 Illustration of mirror reflectivity setup	109
Figure 5.3 Plot of counts v wavelength with mirror at different angles	110
Figure 5.4 Plot of counts v wavelength with custom coating mirrors at different angles	111

Figure 5.5 Illustration of experimental setup with mirror at different angles.....	111
Figure 5.6 CAD of scan head highlighting openings.....	112
Figure 5.7 CAD of scan head w/ back plate removed	113
Figure 5.8 CAD of final design of FMPI optic fixture	114
Figure 5.9 CAD of fully assembled fixture with scan head.....	114
Figure 5.10 Fully assembled FMPI fixture with labels.....	115
Figure 5.11 CAD of individual FMPI optic fixture components.....	116
Figure 5.12 Images showing installation of FMPI optic fixture into custom scan head	117
Figure 5.13 Illustration and image of calibration being performed within Aconity MIDI+.....	119
Figure 5.14 .DAT file from calibration with notch filter in place	121
Figure 5.15 Close-up of .DAT file at 1080nm.....	121
Figure 5.16 Illustration of experiment scan strategy	122
Figure 5.17 Plotted .DAT file of laser experiment at ~1945°C	123
Figure 5.18 Plotted .DAT file of laser experiment at ~905°C	123
Figure 5.19 Plotted .DAT file of laser experiment at ~802°C	124

CHAPTER 1: INTRODUCTION

1.1 PROJECT OVERVIEW

Beginning in 1987 with stereolithography (SL), the first materials used in commercial additive manufacturing (AM) were polymers (Campbell et al., 2022). Since then, AM has expanded into seven different process categories and the range of materials that can be processed has grown with it (Attaran, 2017). Rapid prototyping, mass customization, and reduced labor are some examples of advantages seen in AM (Attaran, 2017). AM is described as a layer-by-layer process in which materials are joined together from 3D computer model data, usually computer-aided design (CAD), (Gibson et al., 2021). AM is classified in seven different process categories that include: material extrusion, vat photopolymerization, sheet lamination, binder jetting, material jetting, powder bed fusion, and directed energy deposition. From these processes, the materials used in powder bed fusion (PBF) and directed energy deposition (DED), or metal powders, will be the focus of this research. AM aspires to achieve highly accurate parts from the original design without any defects typically arising during processing such as porosity, lack of fusion, balling, keyholing, or any dimensional deformation. *In situ* monitoring of the process allows for continuous feedback of sensor data and possible control of the process using that data, which is the intent of the National Institute of Standards and Technology to improve repeatability (Vlasea et al., 2015). Targeted corrective measures during the process would improve the part quality and its repeatability; demonstrated by Demir et al., a co-axial setup using a visible light camera and a near-infrared camera monitored thermal effects and used polishing-type remelting passes to reduce or remove defects. Radiation thermometry methods have been previously used to monitor the PBF process to allow for the further understanding of the dynamic process. This research proposes the use of a multi-wavelength (MW) pyrometer as a tool to characterize the emissivity of metal

powders typically used in metal-based AM to better understand their emissive behavior and improve upon industry sectors like non-contact temperature monitoring techniques, metal AM-based process simulations and process parameter optimization.

1.2 W.M. KECK CENTER FOR 3D INNOVATION

All efforts and work necessary for this thesis were done at the W.M. Keck Center for 3D Innovation (Keck Center) at the University of Texas at El Paso. Originally founded as a biomedical research laboratory in 2000 through a grant from the W.M. Keck Foundation, the laboratory has since grown to specialize and contribute to the innovation of AM altogether. Currently, the Keck Center is home to more than 100 machines ranging from commercial to research use with state-of-the-art machines like the AconityMIDI+, Arcam A2X, and more recent additions like the SLM 280 and RenAM 500Q. Alongside the recent additions of machines, the center itself expanded to a 17,000 square-foot off-campus research facility in which more space was provided for research, economic development, and training alike (W.M. Keck Center, 2022). The center not only ranges in AM abilities with its distinct processing methods, but in visitors from industry professionals to K-12 students. Through an agreement with UTEP in 2018, Aconity3D GmbH, one of the world's emerging leaders in laser-based 3D printing equipment, plans to help the community through attracting high-profile engineering jobs for students and, by means of meaningful research, improve upon the broader technology via the collaborative efforts of UTEP, Aconity3D GmbH, government agencies, and industry. There is no shortage of diversity nor creativity within the center with approximately sixty members across various multi-disciplinary projects. Efforts are still being made in collaboration with public and private entities alike to not only expand the center but advance the entire AM industry.

1.3 ADDITIVE MANUFACTURING

AM has existed a relatively short time compared to other manufacturing methods and techniques. For example, numerical control (NC) machines originated in the 1940s, giving current subtractive manufacturing methods of manufacturing about forty years before AM came to be (Alvarez, 2002). Despite its recent emergence, AM has already expanded into the previously mentioned seven different process categories ranging not only in their methods but in their materials as well, including biomaterials due to AM's advancements in printing precision, speed, and the ability to print complex structures (Bhatia & Sehgal, 2021). The growth in AM partly lies in its advantages in the industry with things like high design flexibility, rapid prototyping/manufacturing and other applications in which design factors can be better addressed through these processing techniques (Attaran, 2017). Automotive, aerospace, and medical industries have already taken advantage of AM for its cost-effectiveness, part consolidation, and mass customization, respectively (Campbell et al., 2012).

The layers that make up a part for manufacturing come from a 3D model that is designed using computer-aided-design (CAD) software. In lieu of traditional instructions for the manufacturing of a component, the CAD models serve as layer-by-layer blueprints (Paul et al., 2018). Software for each AM technique gives instructions for the machines to follow, bridging the gap between design and production. The software replicates the CAD file according to the resolution required for the part to be manufactured, as well as the process used by the machine. Outside of the CAD model and slicing software, there are steps taken in the build setup, printing, and post processing to include as much detail of the original design as possible. Figure 1.1 shows a general workflow for manufacturing a part using AM.

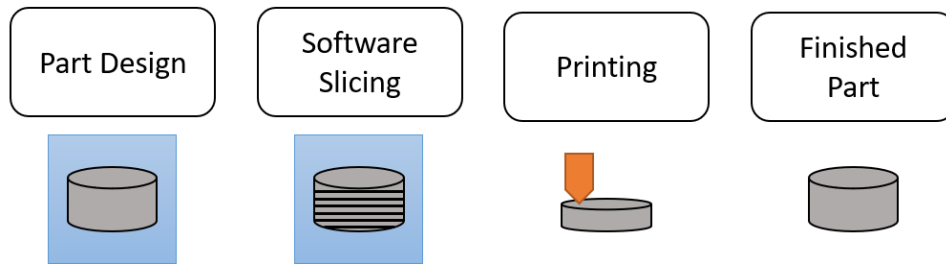


Figure 1.1 General AM workflow

The general AM workflow encompasses the steps taken to fabricate a part from design conceptualization, to final product. However, the different AM process categories employ different techniques that all carry implications of how the layers are bonded, the material used and its properties, accuracy, and overall cost of the machine and process (Gibson et al., 2021). Metals, polymers, and ceramics can all be processed using AM (Tofail et al., 2018); however, AM processes are not universal in the materials they can successfully process.

The focus of this research is on metal powders, specifically those used in powder bed fusion (PBF) and directed energy deposition (DED). L-PBF typically uses fine powders ($15\mu\text{m}$ - $53\mu\text{m}$ particle sizes) that let the process achieve layer thicknesses of about $30\mu\text{m}$ - $50\mu\text{m}$, leading to finer features (Balbaa et al., 2021). The EB-PBF process uses powders ranging in sizes of $45\mu\text{m}$ - $106\mu\text{m}$ to reduce instances of “smoking” in which electrons in the build envelope can accumulate on irradiated particles and can cause them to repel each other (Cordero et al., 2017). Lastly, DED uses the biggest particle sizes of the three (50 - $150\mu\text{m}$) which are required for effective powder feeding (Iams et al., 2022).

1.4 RESEARCH MOTIVATION

A significant limitation in AM is the occurrence of defects that can stem from all processes. The underlying physical phenomena in PBF are difficult to observe since these occur on such small scales not covered by observation and measuring devices (Markl & Körner, 2016). For example,

typical melt pools produced in L-PBF can range in diameters of 100 - 400 μ m and scan speeds of up to 1700mm/s mean that a high resolution and sampling rate of monitoring devices are necessary to capture transient signatures during processing. More limitations include limited modeling approaches, phase changes of the material, and heat and mass transfer associated with each process which make the optimization of parameters difficult (Bikas et al., 2016). Furthermore, anisotropy manifests itself in almost all AM printing technologies due to the layer-by-layer approach AM takes to manufacture parts. Despite this, annealing L-PBF printed Inconel 718 has shown to result in an isotropic microstructure regardless of scanning strategy (Newell et al., 2019). Similarly, Liu et al. demonstrated that increased energy density in an L-PBF machine enhanced the anisotropy on yielding strength in Inconel 718 samples. These are some examples in which undesired consequences of the process can be mitigated or removed altogether. In a review done by Kim et al., AM techniques began using in-situ sensors and cameras to acquire processing data for real-time monitoring, ultimately capable of a closed-loop feedback system. Non-contact temperature monitoring methods implemented within PBF and DED processes do not hinder the freedom of the process and solve quality issues related to the heterogeneous distribution of powder bed temperature in L-PBF and melt pool temperatures for DED (Kim et al., 2018).

For modern non-contact temperature measurement methods that rely on emissivity for true temperature measurements, accuracy becomes an issue in AM processes where material, environment, and the nature of the process itself have a strong influence on the emissivity (Forrest & Murphy, 2016)/(DeWitt & Nutter, 1988). Furthermore, data for emissivity in handbooks is usually presented for specific surface conditions ('polished', 'white hot', etc.) and not related to processing conditions found in PBF (Forrest & Murphy, 2016). Understanding the emissive behavior of the target would lead to improvements in current temperature monitoring techniques,

to data available for the absorptivity of metal powders for process simulations, and for process parameter optimization via understanding of the absorptivity of the powders. The use of an expert-system multi-wavelength pyrometer, FMPI SpectroPyrometer (FMPI), capable of delivering emissivity-independent temperature measurements will enable the study and understanding of the emissivity/absorptivity of metal powders and further the growth of AM via implementation of monitoring techniques for quality assurance and improved understanding of the thermal history. Knowledge of the emissive behavior of metals has potential as input data for current monitoring techniques that require a set emissivity, as well as utilizing the device to monitor surface temperature and characterize the spectral emissivity during processing as it was demonstrated by Fernandez et al. 2021.

1.5 SUMMARY OF RESULTS

The ability to accurately acquire emissivity data using the FMPI and glovebox was demonstrated using a heater specifically designed to heat metal AM powder samples. This design reduced influence from the components of the heater, insulated the samples, and heated different metal powder size distributions. The FMPI produces a temperature, tolerance, exposure time, and signal strength continuously until the software is stopped, meaning that there is uninterrupted data acquisition throughout the experiment. The manufacturer of the FMPI (FAR Associates) defines these metrics under certain conditions; temperature and tolerance are closely related. The tolerance is the standard deviation of the calculated temperature of the target within a ~ 2.7 mm diameter target area. The exposure time is the time it takes for the FMPI's photodetector to become saturated (above 20,000 counts) and provide a measurement, ranging from 4 μ s to 8s. Lastly, the signal strength can be equivalent to the emissivity of the target given the following caveats:

1. The target being measured is isothermal throughout the field of view (~2.7mm diameter spot for this FMPI configuration).
2. The optical path is calibrated without influence from unaccounted sources of absorption or emission.
3. There is no influence from the reflective environment.

provided that the target is not influenced by external factors (i.e., environmental influence or optical path obstructions). The novel method developed and to be described provided information the industry currently lacks on the thermal emissive behavior of metal powders. A design of experiments approach for the emissivity values acquired was used to capture statistical variation of measurements as there is currently no source of information on the emissivity of metal powders.

Table 1.1 Size distribution for powders according to manufacturer

	SD	D10	D50	D90
Particle Size Distribution - 1 (PSD - 1)	15-53 μ m	25 μ m	40 μ m	53 μ m
Particle Size Distribution - 2 (PSD - 2)	45-106 μ m	52 μ m	73 μ m	105 μ m
Particle Size Distribution - 3 (PSD - 3)	45-150 μ m	52 μ m	85 μ m	137 μ m

The initial goal of capturing accurate emissivity measurements for metal powders used in AM was straightforward. However, the methods and procedures to be described are the result of several iterations of calibration and measurement techniques, heater designs, and experiment designs. Calibration techniques that remove optical influence, measurement techniques that capture the same area of different samples and remove radiative environment influence from results, heater design iterations that mitigate radiative influence and provide repeatable heating, and experiments that can be repeated all encompass this research so that this method may lead to

the foundation for emissivity values the industry currently does not have. Recommendations and future work aim to improve upon the repeatability of the method, possibly leading to a standardized test method for capturing this data that will require far fewer measurements if the method is executed properly, and extending the range of temperatures the powder reaches to capture the behavior through phase changes.

1.6 THESIS OUTLINE

The following chapters contain literature reviews, experiment descriptions and design iterations, methods for analysis, results, and potential future research ideas that are believed to be beneficial to the AM industry. In Chapter 2, a brief review of topics related to heat transfer and pyrometry are included to provide background for an overview of monitoring techniques. Chapter 3 is dedicated to describing the method and experimental setup using the glovebox, heater designs, and FMPI. Chapter 4 presents and explains results gathered from the experiments. Chapter 5 covers the integration of the FMPI on an L-PBF machine with custom designs for a scan head, a fixture for the optic, calibration techniques and demonstration of use. Lastly, Chapter 6 provides conclusions derived from results from this research and presents recommendations for future work.

CHAPTER 2: LITERATURE REVIEW

Background in AM technologies, focusing on those which use metal powders as feedstock, and radiation heat transfer will be the focus of this chapter. While comparisons to emissivity values in literature are made, this research and results will deviate from emissivity data in literature being that what is available is for a different surface morphology and so a true comparison cannot be made. However, the variation in emissivity with variables like surface roughness and temperature can help validate trends.

2.1 ADDITIVE MANUFACTURING

The different AM process categories are all similar in the layer-by-layer approach of joining material to manufacture a part. The processes themselves can also be described as 3D Printing (3DP), rapid prototyping (RP), direct digital manufacturing (DDM), rapid manufacturing (RM), and solid freeform fabrication (SFF) (Abdulhameed et al., 2019). Originally developed with polymer materials in mind, AM has grown into seven categories recognized by ISO/ASTM 52900:2015-standards (*ISO - ISO/ASTM 52900:2015 - Additive Manufacturing — General Principles — Terminology*, 2015) and they include: material extrusion, vat photopolymerization, sheet lamination, binder jetting, powder bed fusion, and directed energy deposition. Some of the first materials to be used in AM resulted in parts that were quite weak or would easily warp (Gibson et al., 2021). As the technology was further understood, materials were developed specifically for AM processes. These new materials have resulted in parts that are much more accurate, stronger, longer lasting, and more comparable to parts produced via traditional manufacturing methods (Gibson et al., 2021).

In AM, 3D model data is sliced using data processing software specific to the AM technology intended to be used for its fabrication. The processes deviate into the seven that are

known for a variety of reasons. Material extrusion, an AM technology used commonly for polymeric materials, processes materials in the form of pellets or wires by feeding them through an extruder that maintains the continuous flow of material as it is liquefied. Vat photopolymerization uses a vat of resin that is exposed to a laser source of a specific wavelength, activating the photopolymers that bond the material together. Sheet lamination processes its feedstock by adding sheets of material and cutting the sheet to make the intended CAD model. Directed energy deposition (DED) and powder bed fusion (PBF) can both utilize metal powder feedstock, but DED does not require a powder bed. DED systems, instead, are either wire-fed or powder-blown. For both, a high energy laser/electron beam is used to either melt the metal wire or metal powder onto a substrate. Similarly, PBF technology employs either a high-energy laser beam or an electron beam to fuse specific areas within a powder bed. The powder bed can consist of polymer materials as well, but the processing environment and parameters are different from those of metal powder feedstock. PBF can be further split into two categories depending on the energy source used: laser powder bed fusion (L-PBF) in which a laser source is used, or electron beam powder bed fusion (EB-PBF) where an electron beam is used. A few other differences in the process lie in their environment and feedstock. First, L-PBF utilizes an inert argon environment to mitigate oxidation of the metal powder as it is processed since it does not have the vacuum environment like that of EB-PBF. The feedstocks differ slightly as well with L-PBF utilizing metal powders with size distributions of 15 μm -45 μm , compared to 45-105 μm sizes for that of EB-PBF. This research encompasses all sizes of metal powders used in metal-based AM, including those used for DED (45-150 μm).

The use of a MW pyrometer to capture the emissive behavior of powders being heated will show instances in which other non-contact temperature measurement methods may accurately be

implemented for true temperature measurements. Difficulties arise when acquiring temperature data using the electromagnetic spectrum for PBF and DED processes in which a laser source is used, where its working wavelength (1070nm) interferes with the spectrum used for analysis. The approach and methods taken to ensure accurate measurements are discussed in greater detail in Chapter 3. The following sections of this chapter will give some examples of monitoring techniques currently being used, as well as the background needed to ensure accurate temperature measurements for the methods to be described.

2.2 HEAT TRANSFER

As described by Bergman et al., 2011, heat transfer refers to the movement of thermal energy from one location to another, driven by a variance in temperature. Understanding the physical mechanisms that underlie the different heat transfer modes allows for the use of rate equations that quantify the amount of energy being transferred per unit time (Bergman et al., 2011). This area is consistent with the research to better understand the emissive behavior of metal AM powders in metal-based PBF processes. The three different types of heat transfer processes include conduction, convection, and radiation. The mode of heat transfer depends upon the thermal gradients and whether it exists within a stationary medium, surface and fluid, or between two surfaces. Conduction refers to the heat transfer that occurs within a stationary medium, which may be a fluid or a solid (Bergman et al., 2011). Convection is used to describe heat transfer between a solid object and a flowing fluid. Lastly, thermal radiation occurs in the absence of an intervening medium (fluid or solid). All surfaces of a finite temperature emit energy in the form of electromagnetic waves. Understanding these phenomena of heat transfer will allow for the use of equations that can describe the rate at which energy is transferred via these modes. Several

variables in each situation dictate the heat transfer, and each mode comes with different variables to consider.

Within different stationary mediums (solids, liquids, gases), the way the particles interact differs. However, the interactions of particles can all be described in the same way. The more energetic particles that would be associated with a higher temperature will collide with neighboring particles, transferring the energy to the less energetic particles. Heat transfer equations, therefore, can be quantified in terms of rate equations to compute the amount of energy that can be transferred per unit time. Since the experiments take place within an inert argon environment, the powders are being heated conductively, and the emitted spectrum is being measured, all three areas of heat transfer are of interest.

2.2.1 Thermal Conductivity

Thermal conductivity quantifies the speed at which energy is transmitted through the process of diffusion (Bergman et al., 2011). Ultimately, this depends on the material's atomic physical structure since this can dictate how efficiently heat can be transferred. A high thermal conductivity means the material can efficiently transfer heat, while a material that cannot transfer heat efficiently has a low thermal conductivity, making it an insulator. Metals, for example, transport thermal energy through migrating free electrons and lattice vibrational waves. Pure metals, like zinc and silver, have higher thermal conductivities than other materials like plastics or gases which can be considered insulators. Metal powders have also been found to have a reduced thermal conductivity compared to their bulk material counterparts. This was attributed to the air gaps within the powder, as thermal conductivity increased with increasing metal powder bulk density and particle diameter (Alkahari et al., 2012).

2.2.2 Conduction Heat Transfer

Conduction heat transfer refers to the transfer of thermal energy from one system into another. The rate equation for this mode of heat transfer is known as Fourier's Law and for one-dimensional heat transfer having a temperature distribution of $T(x)$, the equation is expressed as

$$q_x'' = -k \frac{dT}{dx} \quad \boxed{2-1}$$

The heat flux, q_x'' , is the heat transfer rate in the x-direction within the medium per unit area perpendicular to the direction of transfer and thermal conductivity, k , is a transport property specific to the medium. Under steady-state conditions where temperature distribution is linear, the thermal gradient, dT/dx , can be expressed as

$$\frac{dT}{dx} = \frac{T_2 - T_1}{L} \quad \boxed{2-2}$$

Equation 2-2 expresses the total length of the medium as L , where x is a specific location along its length. Given that heat transfer is in the direction of decreasing temperature, T_2 is less than T_1 , and so it follows that dT/dx becomes negative as T decreases with increasing x and ensures that the heat transfer is positive in the positive x direction.

2.2.3 Convection Heat Transfer

Convection heat transfer is governed first by the energy transfer due to molecular motion as previously described, but energy is also transferred by the motion of the fluid (Bergman et al., 2011). The interaction between the fluid and the surface it moves across contributes to heat transfer; therefore, it is important to distinguish between convection, which refers to the cumulative transport of energy, and advection, which is the transport due to bulk fluid motion. The fluid-surface interaction develops a region in which the velocity varies from zero, at the surface, to a finite value associated with the flow, u_∞ . Similarly, in the presence of a thermal gradient between the surface and flow. There will be a region of the fluid in which the temperature varies

from T_s , at $y=0$, to T_∞ , at the outer flow. These two regions are not related except for being a consequence of the interaction between surface and fluid, but convective heat transfer will occur from the surface to the outer flow if $T_s > T_\infty$. At the interface of between the surface and flow ($y=0$), convection heat transfer, as opposed to advection, is the only mechanism by which heat transfer occurs.

Convection heat transfer can further be classified according to how the flow is created. Forced convection, as the name implies, is when the flow is caused externally via atmospheric winds or pumps to name examples. When the flow is induced by differences in density caused by temperature variations in the fluid, it is referred to as free convection. Regardless of the nature of the convection heat transfer process, the rate equation is known as Newton's law of cooling and is expressed as

$$q'' = h(T_s - T_\infty) \quad \boxed{2-3}$$

where q'' is the convective heat flux and is proportional to the thermal gradient between the surface (T_s) and fluid (T_∞). The parameter h is the convection heat transfer coefficient and, like the k value described in conduction heat transfer, depends on conditions at the region where the surface and fluid interact, the nature of the fluid motion (convection or advection), and several fluid thermodynamic and transport properties. Heat always transfers from higher temperatures (higher energy) to lower temperatures (lower energy) regardless of heat transfer coefficient, the fluid and surface interaction, or transport properties.

2.2.4 Radiation Heat Transfer

Thermal radiation is energy emitted by any matter that is at a nonzero temperature in the form of electromagnetic waves (photons) due to the changes in the electronic configuration of the atoms or molecules (Bergman et al., 2011). Unlike the previous modes of heat transfer, radiation

does not require a material medium and even occurs most efficiently in a vacuum (Bergman et al., 2011). Unless the particles of an object are at a fixed position (absolute zero), the atoms constituting the object will always be moving, thereby emitting from the thermal energy bounded by its surface. While the previously mentioned modes of heat transfer use a medium, radiation heat transfer relies on a material's surface and its radiative properties. The radiative properties of a surface that transfer heat are the driving forces behind typical non-contact temperature measurements and can influence the accuracy. Assumptions are made to account for these complexities in measurements without negatively impacting the accuracy or integrity. The research will show the understanding and quantified measurements of emissivity to improve upon conventional non-contact temperature methods, and why the FMPI proves to be beneficial for this purpose.

The surface emissive power is the measure of the amount of energy released per unit area. An upper limit to this emissive power is shown by the Stefan-Boltzmann law as

$$E_b = \sigma T_s^4 \quad \boxed{2-4}$$

where T_s is the absolute temperature (K) of the surface and σ is the Stefan-Boltzmann constant ($5.67 \times 10^{-8} \text{ W/m}^2 \cdot \text{K}^4$). A surface that can be described as such is called an ideal radiator or blackbody. However, the heat flux emitted by a real surface is only a fraction of that of a blackbody at the same temperature, given by

$$E = \epsilon \sigma T_s^4 \quad \boxed{2-5}$$

where ϵ is the surface emissivity and is a value between 0 and 1.

2.3 RADIATION PROPERTIES OF SURFACES

A blackbody is an idealized surface that absorbs all incident radiant energy. However, real-world materials do not behave as such and, instead, behave as either gray-body or non-gray-body

with most materials behaving as the latter. Instead of absorbing all incident radiant energy, like that of a blackbody, the energy will either be transmitted, absorbed, or reflected by the body (Bass et al., 1995). Due to the conservation of energy, the total radiant energy is split amongst these three processes. A body can be described as opaque or transparent, meaning light may either pass through the body, or not. Light cannot pass through an opaque body, while the degree of radiant energy that passes through a transparent body is described by its transmissivity. Transmission is used to describe the process by which incident radiant energy leaves a surface or medium from a side other than the incident side (Bass et al., 1995). Absorption of incident radiant energy denotes radiant flux energy being converted to another form of energy, usually heat (Bass et al., 1995). Lastly, reflection is when a fraction of the radiant flux incident on a surface is returned into the same hemisphere whose base is the surface which contains the incident radiation; reflections can either be specular (in the mirrored direction), or diffuse (scattering into the hemisphere) (Bass et al., 1995). Typically, it is a combination of both specular and diffuse reflections that make up the reflection process. The application of the conservation of energy allows for the statement that the sum of the transmission, denoted by τ , absorption, α , and reflection, ρ , is equal to unity and can be represented as

$$\alpha + \tau + \rho = 1$$

2-6

Figure 2.1 shows the absorption, reflection, and transmission of radiant energy, denoted as G , on a material.

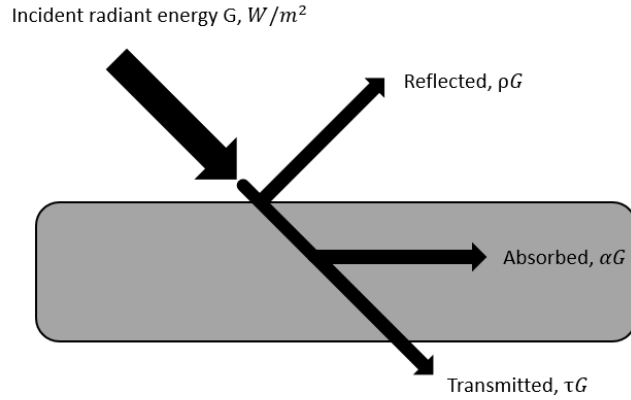


Figure 2.1 The absorption, reflection, and transmission of incident radiant energy by a material

The mathematical expressions for the absorbed, reflected, and transmitted energy are as follows:

$$\alpha = \frac{\text{Absorbed radiation}}{\text{Irradiation}} = \frac{G_{abs}}{G} \quad \boxed{2-7}$$

$$\rho = \frac{\text{Reflected radiation}}{\text{Irradiation}} = \frac{G_{ref}}{G} \quad \boxed{2-8}$$

$$\tau = \frac{\text{Transmitted radiation}}{\text{Irradiation}} = \frac{G_{tra}}{G} \quad \boxed{2-9}$$

G is the radiation flux incident on the surface, G_{abs} , G_{ref} , G_{tra} are the absorbed, reflected, and transmitted radiation values, respectively. While still maintaining unity, equation 2-10 describes the relationship between absorptivity and reflectivity for an opaque body with

$$\alpha + \rho = 1 \quad \boxed{2-10}$$

The above equation can only be used independent of hemispherical properties since the incident radiant energy is the total radiation flux on the surface from all directions and across all wavelengths (Bass et al., 1995). It can also be noted that when an object is in thermal equilibrium,

the absorptivity is exactly equal to the emissivity. To account for the wavelength and direction, equations 2-11 and 2-12 represent the spectral directional absorptivity and spectral directional reflectivity as:

$$\alpha_{\lambda,\theta}(\lambda; \theta, \phi) = \frac{I_{\lambda,abs}(\lambda; \theta, \phi)}{I_{\lambda,i}(\lambda; \theta, \phi)} \quad \boxed{2-11}$$

$$\rho_{\lambda,\theta}(\lambda; \theta, \phi) = \frac{I_{\lambda,ref}(\lambda; \theta, \phi)}{I_{\lambda,i}(\lambda; \theta, \phi)} \quad \boxed{2-12}$$

The equation can further be reduced by assuming the incident radiant energy is coming from all directions, the spectral hemispherical absorptivity and reflectivity can then be defined using G_λ to represent the spectral irradiation incident on the surface, $G_{\lambda,abs}$ for the absorbed portion and $G_{\lambda,ref}$ for the reflected portion (Cengel & Ghajar, 2014) as:

$$\alpha_\lambda(\lambda) = \frac{G_{\lambda,abs}(\lambda)}{G_\lambda(\lambda)} \quad \boxed{2-13}$$

$$\rho_\lambda(\lambda) = \frac{G_{\lambda,ref}(\lambda)}{G_\lambda(\lambda)} \quad \boxed{2-14}$$

Lastly, like a gray surface for which its properties are independent of wavelength, the average values of absorptivity and reflectivity can be expressed as:

$$\alpha = \frac{\int_0^\infty \alpha_\lambda G_\lambda d\lambda}{\int_0^\infty G_\lambda d\lambda} \quad \boxed{2-15}$$

$$\rho = \frac{\int_0^\infty \rho_\lambda G_\lambda d\lambda}{\int_0^\infty G_\lambda d\lambda} \quad \boxed{2-16}$$

These equations show the dependence absorptivity and reflectivity have on several factors, namely direction and wavelength. This is important to understand for accurate assumptions and predictions of emissivity.

2.3.1 The Electromagnetic Spectrum

The electromagnetic spectrum is the range of all electromagnetic radiation. These types are categorized by their wavelength into sets referred to as bands which include gamma rays, X-rays, ultraviolet light, visible light, infrared light, and radio waves. The sets span across several wavelength values, sometimes including orders of magnitude above where they begin. Thermal cameras utilize infrared radiation in the spectral range of $\sim 0.74\mu\text{m}$ to $14\mu\text{m}$ for temperature measurements (Manullang et al., 2021). The infrared band range can further be categorized into near infrared ($0.74\mu\text{m} - 1\mu\text{m}$), short wave infrared ($1\mu\text{m} - 3\mu\text{m}$), medium wavelength infrared ($3\mu\text{m} - 5\mu\text{m}$), and long wavelength infrared ($8\mu\text{m} - 14\mu\text{m}$). The FMPI used in this research operates within the spectral range of $0.9\mu\text{m}$ to $1.7\mu\text{m}$, which is within the near infrared band.

2.3.2 Emissivity

Emissivity (ϵ) is the ratio of radiation emitted of a real body to that of a blackbody at the same temperature (Cengel, 2007). Any real surface has a distinct ability to emit energy, meaning it can be influenced and is highly dependent upon surface characteristics (Barreira et al., 2021a). Furthermore, changes to the surface, chemistry, phase, and temperature of the surface can have an impact (Fernandez et al., 2021). This, coupled with potential influences from the measurement environment, implies that non-contact temperature measurement methods cannot be universally adopted if the nature by which they acquire these measurements is dependent on the surface being measured. It is therefore necessary to distinguish between surfaces and targets that exhibit different behaviors. Graybodies are non-blackbody emitters (real bodies) for which the emissivity is constant regardless of the wavelength (Barreira et al., 2021a). A blackbody corresponds to $\epsilon=1$, while a graybody will have a value of emissivity that is between 0 and 1. The emissivity of a surface varies with the surface temperature, wavelength, and the direction of the emitted radiation

(Cengel, 2007). Surfaces may be idealized as diffuse or specular, which correspond to the way radiation is reflected. Diffuse reflection occurs when the intensity of the reflected radiation is the same in all directions (hemispherical) regardless of the incident radiation angle. Specular reflection, oppositely, occurs when all reflected radiation depends upon and is correspondent with the incident angle. Mirror-like surfaces are a good example of specular reflection, although no surface is entirely specular or diffuse and is often a combination of the two. Emissivity depends upon the nature of the surface in this context as well, a highly specular surface means emissivity will vary depending on the angle at which it is being observed while a diffuse surface means the emissivity is independent of this viewing angle. A graybody, therefore, assumes a diffuse reflection since the definition implies the emissivity is independent of direction. The largest body of emissivity data comes from the TPRC (Purdue University) and will be referenced to throughout this work to compare values from experiments (*Thermophysical Properties of Matter - The TPRC Data Series. Volume 7. Thermal Radiative Properties - Metallic Elements and Alloys*, 1970).

2.4 THERMAL EMISSION

Radiation travels in the form of waves (electromagnetic waves) and comes from the vibration of atoms in a material/body approximately $1\mu\text{m}$ from the exposed surface (Bergman et al., 2011). Since radiation is viewed as traveling via electromagnetic waves, frequency and wavelength are used to describe its properties. The oscillation of the atoms dictates the wavelength of energy emitted. The more the atoms oscillate, the more energetic the waves are and is described in Wien's Displacement Law show in equation 2-17 as

$$\lambda_{max} = \frac{b}{T} \quad \boxed{2-17}$$

The equation states that as temperature increases, the wavelength at which the peak emittance occurs decreases. The following Figure shows the blackbody spectrum at different temperatures.

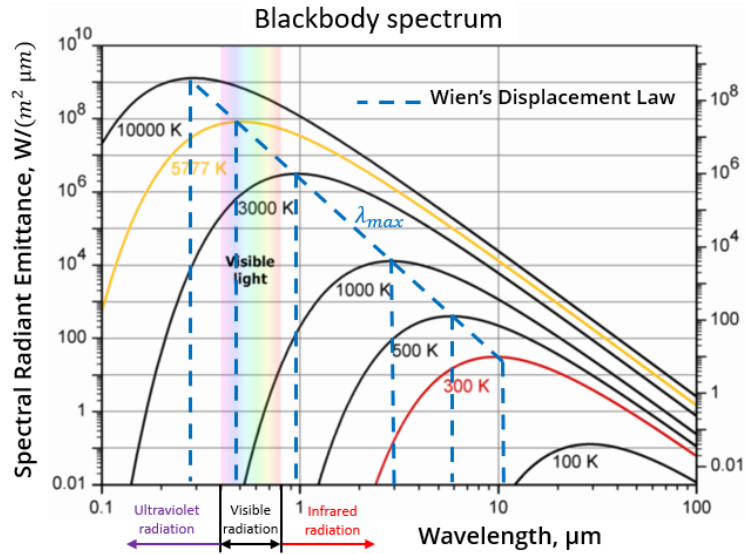


Figure 2.2 Blackbody spectrum at different temperatures

Electromagnetic waves travel at the speed of light in a vacuum, $c_0 = 2.9979 \times 10^8 \text{ m/s}$, and are characterized by their wavelength (Cengel, 2007). Radiation can be viewed as the propagation of a collection of particles termed photons or quanta (Bergman et al., 2011). This implies that there is no average of energy form the emitted wavelengths, but instead an uneven distribution dependent upon the wavelength. Since radiation travels as electromagnetic waves, wave properties like frequency and wavelength are attributed to it. The wavelength is derived from the speed of light and the frequency, shown in equation 2-18 with

$$\lambda = \frac{c}{\nu} \quad \boxed{2-18}$$

Wavelength is expressed as nanometers ($1 \times 10^{-9} \text{ m}$), nm, or micrometers ($1 \times 10^{-6} \text{ m}$), μm . The frequency of an electromagnetic wave is dependent only upon the source as it comes from the oscillation of the atoms and is expressed in hertz (Hz) which is the number of oscillations per second. Both the magnitude of the radiation at any wavelength and the spectral distribution vary with the nature and temperature of the emitting surface (Bergman et al., 2011).

2.5 BLACKBODY RADIATION

The net radiative flux can be simplified by expressing the various intensities in terms of the intensity associated with a perfectly emitting and absorbing surface, a blackbody, as well as the emissivity, absorptivity, and reflectivity of the surface (Bergman et al., 2011). A blackbody absorbs all incident radiant energy regardless of wavelength and direction and emits independent of direction, making it a diffuse emitter. The blackbody serves as a standard by which the radiative properties of real surfaces can be compared to, meaning no other surface can emit more energy than it. The most accurate approximation utilizes a cavity with a uniform temperature on its inner surface. If radiation enters the cavity through a small aperture, it will likely be reflected within the cavity before it exits the same aperture and eventually becomes almost entirely absorbed by the cavity and thus the blackbody behavior can be approximated. An illustration of this is shown in Figure 2.3.

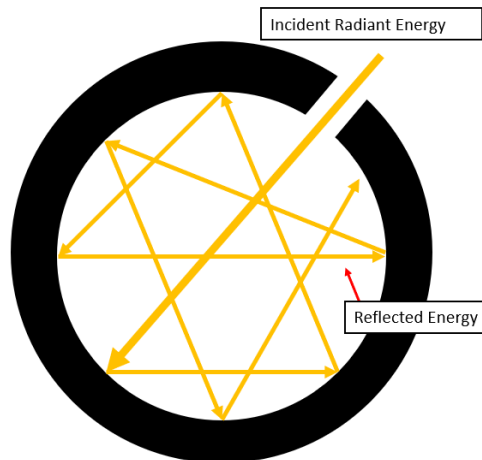


Figure 2.3 Illustration of a blackbody cavity

Blackbody radiation is present within the cavity regardless of whether the surface of the cavity exhibits high reflectivity or absorption (Bergman et al., 2011). Due to all the reflections within the

cavity, the surface can be said to be diffuse in nature (independent of direction). The blackbody spectral intensity was determined by Max Planck and is expressed as

$$I_{\lambda,b}(\lambda, T) = \frac{2hc_0^2}{\lambda^5 e^{\left(\frac{hc}{\lambda k_B T}\right)} - 1} \quad \boxed{2-19}$$

where $h = 6.626 \times 10^{-34} \text{ J} \cdot \text{s}$ and $k_B = 1.381 \times 10^{-23} \text{ J/K}$ and are the Planck and Boltzmann constant, respectively. T is the absolute temperature of the blackbody (K).

2.6 PYROMETRY

Consisting of single-color, two-color, and multi-color pyrometers, pyrometers are capable of remotely measuring temperature. The “color” refers to the wavelengths used to capture the radiation intensity. A single-color pyrometer adds up all the thermal radiation intensity in the range of wavelengths the photodetector operates at and relates the intensity to a temperature using the equation

$$I_{\lambda_1} = \varepsilon_{\lambda_1} L_{\lambda_1} \quad \boxed{2-20}$$

Where the signal, I , is calculated from the target emissivity at the measurement wavelength, ε_{λ_1} , and the radiant energy at measurement wavelength equivalent to a blackbody at equal temperature, L_{λ_1} , and thus correlated to a temperature given the raw intensity of the target. Similarly, a two-color pyrometer operates in the same ways, though the measurements are taken at two different wavelengths or ranges of wavelengths. A two-color pyrometer assumes the emissivities at the chosen wavelengths are similar, or at least have a linear relationship so that a slope adjustment for emissivity can account for the discrepancies in measurements. The intensities gathered at the different wavelengths are:

$$I_{\lambda_1} = \varepsilon_{\lambda_1} L_{\lambda_1} \quad \boxed{2-21}$$

$$I_{\lambda_2} = \varepsilon_{\lambda_2} L_{\lambda_2} \quad \boxed{2-22}$$

The two emissivity values can then be canceled out or accounted for using the following equation:

$$\frac{1}{T_{new}} = \frac{1}{T_{old}} + \left(\frac{\lambda_1 \lambda_2}{14388(\lambda_2 - \lambda_1)} \right) \ln \left(\frac{\varepsilon_{\lambda_2}}{\varepsilon_{\lambda_1}} \right) \quad \boxed{2-23}$$

where T_{new} and T_{old} are the temperatures (Kelvin) after and before the slope adjustment, respectively. λ_1 and λ_2 are the effective wavelengths for each channel and ε_{λ_1} and ε_{λ_2} are the emissivities of the target for the corresponding channels. From this, a temperature can be derived independent of emissivity. However, for both previously mentioned pyrometers, emissivity plays a significant role in the acquisition of data. For the single-color, an emissivity must be known to calculate an accurate temperature and for the two-color, a graybody assumption is necessary to disregard the influence that direction and wavelength may have on the object. This is especially problematic for metals in which the monotonic decrease of emissivity with wavelength has been detected (Felice, 2002). Emissivity is dependent on surface characteristics as was found in Taylor et al. 2020. that explored the relationship between surface roughness and emissivity in which the surface roughness directly impacts the emissive behavior of the material (Taylor et al., 2020).

Next, a multi-wavelength pyrometer operates like a two-color pyrometer except it extends to several other wavelengths and ranges. A comparison of the types of pyrometers and the number of wavelengths they utilize is shown in Figure 2.4 below.

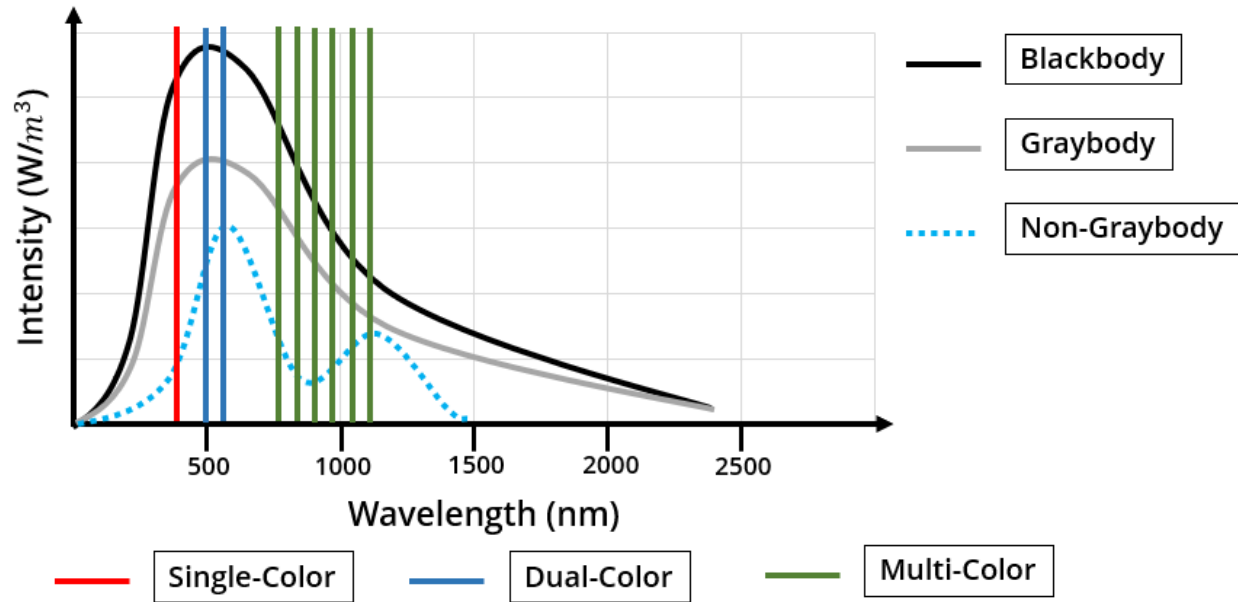


Figure 2.4 Pyrometers and the number of wavelengths they utilize

The FMPI used in this research does not rely on prior knowledge of emissivity and instead examines the data in real-time to make decisions on how it is processed based on the results of the criterion it applies (Felice, 2002). The use of the FMPI described by Fernandez et al. 2021. concluded that emissivity changes during the EB-PBF process and yet, accurate surface temperature measurements were acquired using the device. This research presents a method to capture the emissive behavior of AM metal powder to utilize in non-contact temperature measurement applications, improve upon process simulations, and assist in process parameter optimization.

2.6.1 FMPI SpectroPyrometer, A Multi-Wavelength Pyrometer

The FMPI SpectroPyrometer is capable of reading temperatures from 300°C – 2,000°C with a $\pm 0.15\%$ accuracy on gray targets (measured between 500°C and 2,000°C) and a $\pm 0.25\text{-}0.75\%$ accuracy on non-gray targets as described by the manufacturer (FAR Associates, OH, USA). Since the device is capable of measuring gray and nongray bodies, the FMPI can capture

accurate thermal signatures regardless of the surface characteristics. Using a 256-element Indium-Gallium-Arsenide (InGaAs) photodetector the device can resolve 250 wavebands of ~2nm (Felice, 2002). The device captures the target's intensity within the wavelength range of 900-1700nm simultaneously in all 250 wavebands, after which it calculates temperature using the following equation

$$T = \frac{C' \left(\frac{1}{\lambda_2} - \frac{1}{\lambda_1} \right)}{\ln R - 5 \ln \left(\frac{\lambda_2}{\lambda_1} \right)} \quad \boxed{2-24}$$

In the equation, C' represents the second radiation constant, R is the ratio of intensities I_1 and I_2 , and λ_1 and λ_2 are the wavelengths the intensities were measured at. It is with this equation that the FMPI creates a matrix of temperatures for the target temperature that is obtained by averaging and consensus. The .DAT files produced by the FMPI show the intensity (raw and corrected), noise, and signal strength (target emissivity throughout wavelength range of FMPI pyrometer) for each temperature measurement the pyrometer makes. The .log files display the average temperature, tolerance (standard deviation of temperature), and signal strength (emissivity at 1500nm). Emissivity values reported are derived from the following expression once the intensity is captured and temperature calculated (Felice, 2004)

$$\varepsilon = \frac{L \lambda^5 [e^{\frac{hc}{\lambda k_B T}} - 1]}{2hc^2} \quad \boxed{2-25}$$

Values for the speed of light in a vacuum ($2.998 \times 10^8 \text{ m} \cdot \text{s}^{-1}$) Planck's constant ($6.626 \times 10^{-34} \text{ J} \cdot \text{s}$) and the Stefan-Boltzmann constant ($1.381 \times 10^{-23} \text{ J} \cdot \text{K}^{-1}$) are denoted by c , h , k_B , respectively. The intensity values captured are taken as L and the average temperature calculated as T in the equation. Raw intensity values are corrected by employing the ratio solution of Planck's law for several intensity wavelength values (Felice, 2002). The corrected

intensity values become a matrix with temperature values and an analysis of the standard deviation of their average is done. If the analysis does not pass the criterion, the algorithm will instead check the data to see if it agrees more with a non-graybody behavior and corrects temperature values in the matrix according to this. After the temperature matrix has been recalculated, the standard deviation then becomes the tolerance for the temperature values recorded. Further detail in Chapter 3 will discuss how key variables are controlled to validate the signal strength produced so that it may be considered the emissivity of the target.

2.6.2 FMPI Design

The FMPI requires a fiber optic cable and focusing lens to be able to acquire the raw light from the target. The fiber optic cable connects the pyrometer and the optic, simply acting as a medium while the optic gathers and focuses the light. An analog-to-digital conversion system converts the information captured by the optic to display results on a computer monitor that include the temperature, signal strength, and tolerance. The .DAT file shows the raw and corrected intensities, between the wavelengths of 1080nm – 1640nm, that are used to ultimately calculate the temperature. Figure 2.5 is a schematic of the device and how it works.

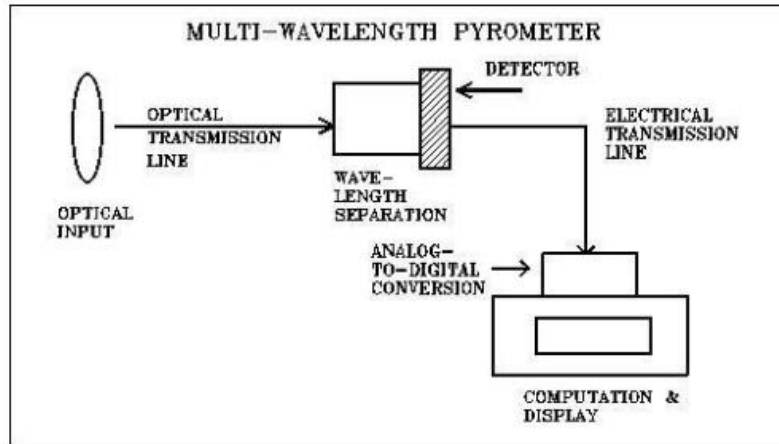


Figure 2.5 FMPI schematic; US patent 5772323 and 6379038B (Felice, 2012)

With an exposure time ranging between $4\mu\text{s}$ to 8s , the device automatically adjusts this according to the raw intensity. The more photons (above 300°C) that pass through the FMPI's detector, the faster the device will acquire data. The fastest the device can acquire data is $4\mu\text{s}$; beyond 8s , the FMPI begins a new acquisition value.

2.7 PROCESS MONITORING

Different defects can originate as the PBF process unfolds, although post-processing can be performed on the part to mitigate or remove defects from PBF-produced parts to improve the quality and meet requirements. Multiple process signatures during the processing of a part using PBF can be monitored either co-axial (Figure 2.6), placed within the optical path and specific to laser energy sources of PBF, or off-axial (Figure 2.7), outside the optical path, to obtain data as it pertains to the quality of a part.

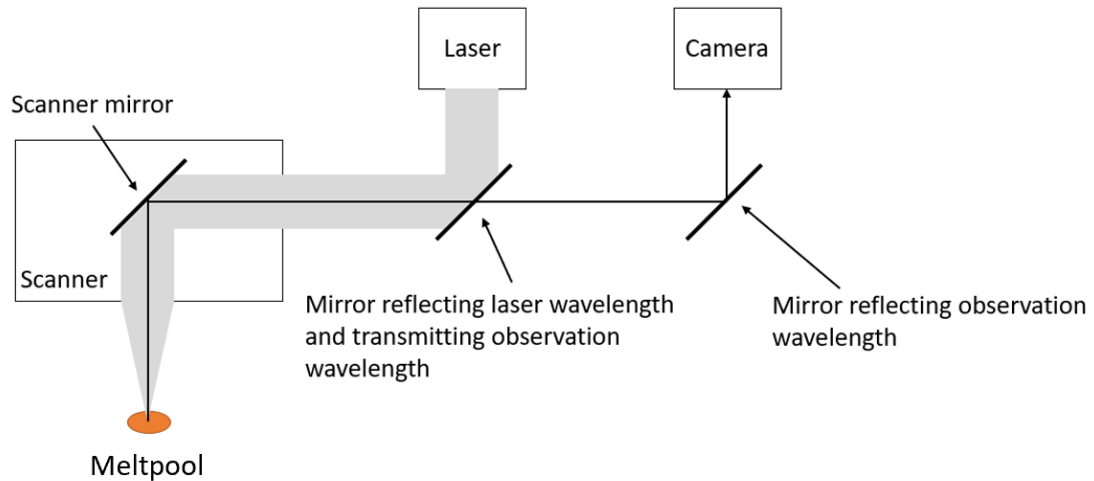


Figure 2.6 e.g., Co-axial setup for laser energy source

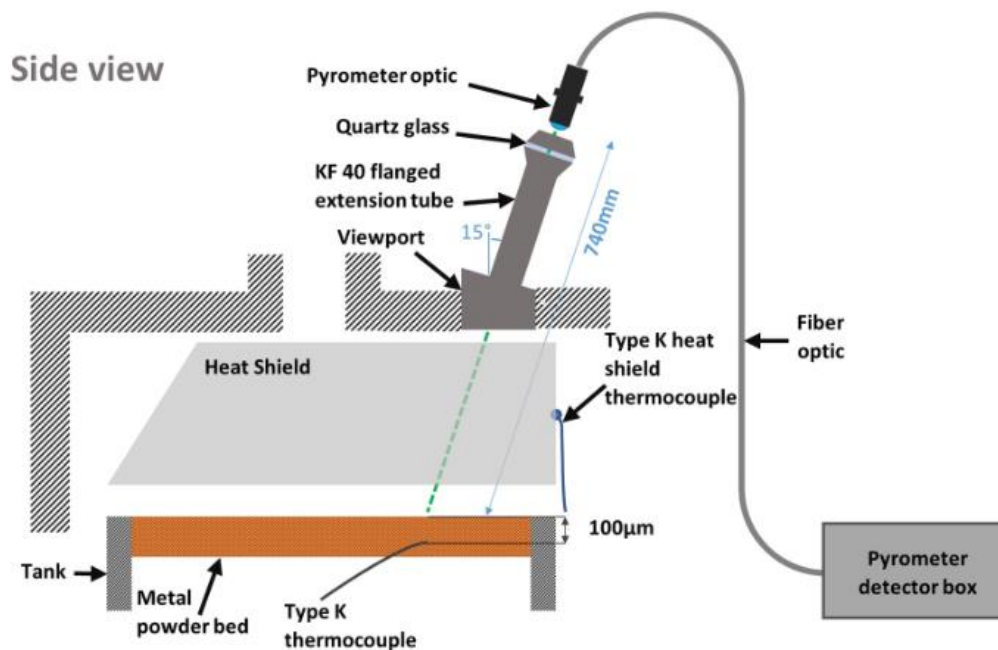


Figure 2.7 e.g., Off-axis setup for PBF process (Fernandez et al. 2021)

These process signatures are characteristics of the process that come from the powder heating, melting, and solidification as they occur during the build (Grasso & Colosimo, 2017). These signatures can further be categorized as: 1) observable signatures, and 2) derived signatures. Observable signatures are those which can be measured during the process by using sensing

devices, while derived signatures come from analytical models or simulations. There are categories of interest within observable process signatures regarding in-situ sensing which include the melt pool, the scanning track of the energy source, the slice, and the powder bed itself. The “powder bed” refers to the loose powder deposited by the recoating system, while the “slice” refers to the layer of the part scanned by the energy source. Data collection devices utilized in literature for radiative properties via non-contact can be generalized by the spectrum utilized: 1) Imaging in the infrared spectrum ($0.74\mu\text{m} - 14\mu\text{m}$) and 2) imaging in the visible spectrum ($350\text{nm} - 740\text{nm}$). These devices differ, mainly, in the spectrum monitored, ranging from the visible to long wavelength infrared (LWIR).

The importance of temperature within all metal production, and the dynamic PBF process itself, leads to various research in which temperature, or intensity of radiation at a particular wavelength, is monitored and correlated to a measurable quality parameter for the purpose of producing parameters for the process to be optimized. For Price et al. 2014, powder porosity was found to be crucial to the thermal characteristics during EBM (Price et al., 2014). Increasing the powder porosity increased the melt pool size proportionally and drastically reduced the thermal conductivity from 2.44 W/mK at 50% porosity versus 10.17 W/mK for solid Ti-6Al-4V at 750°C . Similarly, in Vallabh and Zhao a map of the melt pool on the X-Y plane developed on a commercial EOS M290 LPBF machine using an integrated high speed CMOS camera and a photodiode to detect deformation due to thermal stresses and overheating at overhang zones (Vallabh & Zhao, 2022).

Optical monitoring using pyrometers has been shown to be beneficial in its remote sensing capabilities which can be used in the PBF process to monitor areas of interest to provide further information about a part’s thermal history.

Pyrometry has been used to monitor thermal signatures as they relate to the melt pool size and temperature intensity. Similarly, the track and powder bed have been reported in literature to have been monitored as well. A co-axial monitoring setup done by Pavlov et al. 2010 used a two-color pyrometer and CCD camera integrated with the optical scanning system of a PHENIX PM-100 SLM machine to monitor the temperature within the laser impact zone (Pavlov et al., 2010). The sensible variation of the main operational parameters was captured by the pyrometer signal, and 2D temperature mapping from the heat affected zone (HAZ), while the temperature intensity of the melt pool was monitored. Here it is important to note that the accuracy of two-color pyrometry to measure temperature depends on a known emissivity at the same wavelengths as those used by the pyrometers. During the monitoring of a EB-PBF process, variations in temperature of up to 360°C were seen when comparing uncorrected to corrected emissivity values when using a FLIR SC645, an IR camera (Rodriguez et al., 2015). In Berumen et al. 2010, the same process signature is monitored and proven to be capable of successful monitoring and can assist in making up relevant parameters in a database for each building job (Berumen et al., 2010). Customized reports can be generated from these databases and be integrated in a production management system, further solidifying the fact that these process signatures are key in quality control. Defects and their causes have been correlated and the monitoring of the PBF process has brought with it the ability to further analyze defects and how to improve the processing parameters that cause them. Pertaining to common features in PBF manufacturing, Chivel and Smurov determined that the destruction of overhanging layers is associated with overheating, instabilities, and their growth (Chivel & Smurov, 2010). A two-color pyrometer was used to carry out measurements and determine the mechanisms of the melt penetration into loose powder. Melt pool monitoring has been important to the industry when determining part quality

and process stability. Clijsters et al. 2014 used a photodiode and NIR thermal CMOS camera sensitive to wavelengths in the range of 400nm – 1000nm together logged melt pool intensity, area, length and width to show quality of a part during and after manufacturing by relating signals observed in situ to actual defects revealed via X-ray CT (Clijsters et al., 2014). Gutknecht et al. 2020 employed a co-axial setup of a two-color pyrometer integrated into an SLM machine to collect emitted radiation from the melt pool and its vicinity (Gutknecht et al., 2020). Long term stability of the process was verified by examining raw data of the pyrometer, operating within 1450nm – 1800nm, alongside a secondary CMOS based high-speed camera receiving process signals at the 850nm wavelength. However, further investigation and a higher temporal resolution was needed for detecting events such as inhomogeneous powder deposition. Slices have been monitored to determine their application in determining process stability as well, adjacent scan vectors, overhang zones, and acute corners were shown to have significant influence on the processing influence and were captured via a photodiode operating within the range of 780nm and 950nm and high-speed CMOS camera (Craeghs et al., 2011). Bayle and Doubenskaia 2008 explored IR camera and pyrometry applied for SLM process visualization and control and determined IR cameras can see ejected liquid droplets and the temporal change of heat affected zones along tracks, which can be correlated to the process stability and suggests applications outside of accurate temperature measurements for IR cameras (Bayle & Doubenskaia, 2008). Temperature monitoring is useful in optimizing process performance. Average values of temperature, however, cannot be used to determine process stability which is important for repeatability of manufacturing metal components.

CHAPTER 3: METHODOLOGY AND PROCEDURES

The following chapter will include the materials used, design of components with corresponding schematics, and the instrument used for capturing thermal signatures. The experimental setup and procedures that were conducted for each of the experiments are outlined and discussions regarding calibration procedures and steps taken to isolate the radiative environment (a common source of influence for any device capturing the infrared spectrum). To be detailed in this chapter will be the requirements to procure spectral emissivity measurements and the steps taken to ensure those requirements were met through this methodology including the design of the heater used and environment conditions.

3.1 INTRODUCTION

To capture the spectral emissivity of metal AM powders, there are design requirements that need be met prior to each measurement that are described further in the following section but can be condensed into the following major points: 1) Control sources of emissivity variability of the target (i.e. morphology, chemistry, phase of material), 2) Ensure the powder is not being influenced by external sources of radiation and is the sole thermal signature being acquired, 3) Heat the powder through a range of temperatures, maintaining the target in isothermal or in a steady state temperature at the time of data acquisition 4) Ensure the target area is being measured.

3.2 MATERIAL

To control sources of emissivity variability, one being chemistry, the material that was used for these experiments was kept the same for each powder size distribution, a nickel-based superalloy (Inconel 718) from AP&C (AP&C, Quebec, Canada). The experiments used three different particle size ranges of 15 μm -53 μm (d50-40 μm), 45 μm -106 μm (d50-73 μm) and 45 μm -150 μm (d50-85 μm) as specified by the manufacturer (UNS N07718, AP&C, Quebec, Canada).

The powders had not previously been used or exposed to any PBF processing and samples of the powders were collected in separate vials. Scanning electron microscope (SEM) images taken in a JEOL IT500LV (Tokyo, Japan) of the different spheroidal particle samples at 150x were taken prior to the powders being heated and are shown in the Figures 3.1 – 3.3.

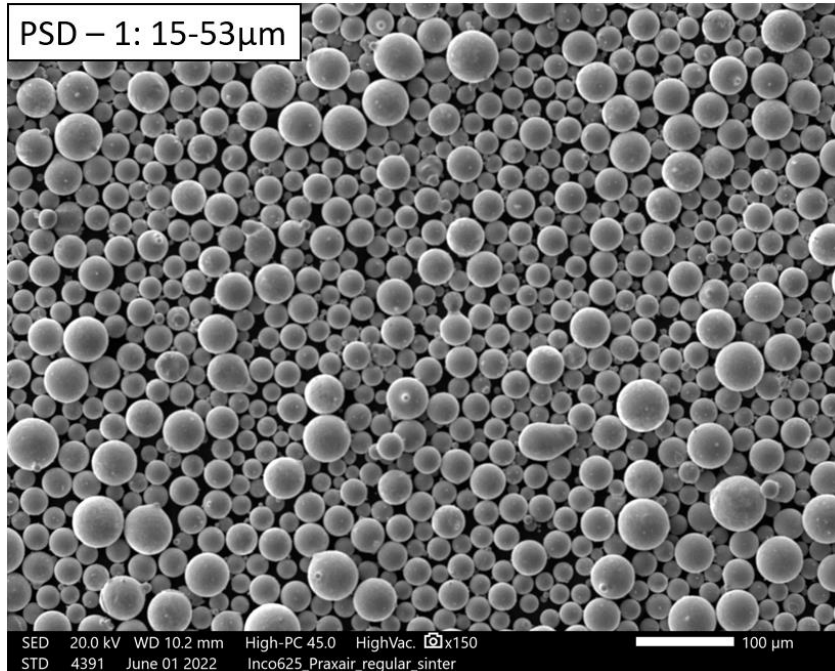


Figure 3.1 SEM image of PSD - 1 at 150x

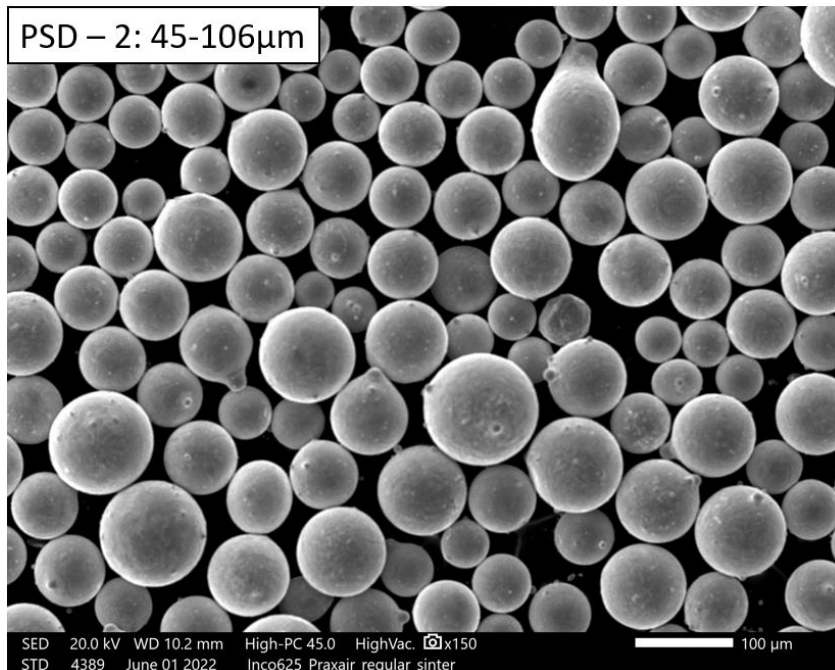


Figure 3.2 SEM image of PSD - 2 at 150x

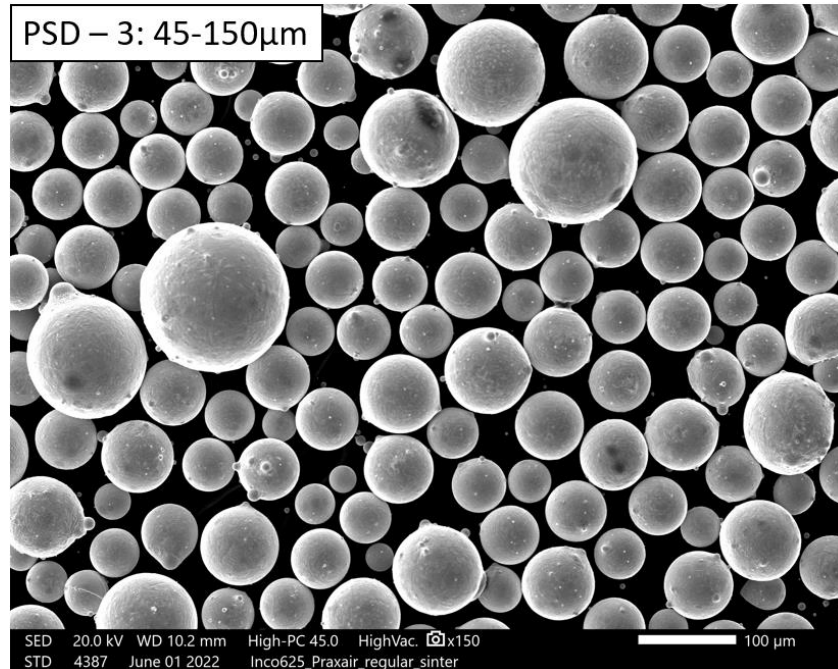


Figure 3.3 SEM image of PSD - 3 at 150x

Although this alloy was the only one employed for this method, it is expected that it can be applied to others used in metal AM processes. The chemical compositions obtained from the manufacturer for the lots containing the powders are shown below.

Table 3.1 Inconel 718 elements and their percentages for PSD - 1 and PSD - 2

Item	Unit	Measured Value
C	Wt. %	0.030
Mn	Wt. %	0.090
Si	Wt. %	0.040
P	Wt. %	0.005
Si	Wt. %	0.002
Cr	Wt. %	18.900
Co	Wt. %	< 0.1
Mo	Wt. %	2.970
Ti	Wt. %	0.920
Al	Wt. %	0.540
Fe	Wt. %	Balance
Nb + Ta	Wt. %	5.000
Cu	Wt. %	< 0.100
Ni	Wt. %	53.160
B	Wt. %	0.003
O	Wt. %	0.014
N	Wt. %	0.005

Table 3.2 Inconel 718 alloy elements and their percentages for lot containing PSD - 3

Item	Unit	Measured Value
C	Wt. %	0.050
Mn	Wt. %	0.130
Si	Wt. %	0.080
P	Wt. %	0.000
Si	Wt. %	0.003
Cr	Wt. %	18.800
Co	Wt. %	0.100
Mo	Wt. %	2.930
Ti	Wt. %	0.920
Al	Wt. %	0.490
Fe	Wt. %	Balance
Nb + Ta	Wt. %	5.050
Cu	Wt. %	< 0.100
Ni	Wt. %	52.810
B	Wt. %	0.002
O	Wt. %	0.011
N	Wt. %	0.017

The inert glovebox environment allows for metals typically prone to oxidation, like copper, to also be viable for the same method described for Inconel 718 without significant oxidation which has been shown to increase the emissivity by at least a factor of 3 (Balat-Pichelin et al., 2017). The research demonstrated that Inconel 718 powder can be heated to temperatures up to 600°C with the current heater design and it is expected that powders with the same or better thermal conductivity than Inconel 718 powder would also be able to reach such temperatures. This gives potential for the method to explore how variables such as the chemical composition can impact the emissivity/absorptivity of powders as it was shown by (King et al., 2018). To reduce the influence of oxygen and environment on the experiments they were performed within a custom design of an LC-150 Standard Glovebox (LC Technology Solutions, MA, USA) with a brushed stainless-steel enclosure, made to include two viewports at the top of the glovebox chamber. When connected to the manufacturer's RGP-050 or RGP-1 series of gas purification systems the

glovebox can maintain oxygen levels below 1ppm. The antechamber of the glovebox produces a vacuum of -30 in.Hg (~15psi) to help remove oxygen before anything enters the glovebox.

3.3 HEATER

The original design of the heater for the experiments was intended to reach temperatures of about 1,000°C. Previous iterations of the heater from its original design will be shown and described in this section. Design considerations for the development of the heater included: 1) heating the powder up to 1,000°C from room temperature while maintaining steady state temperatures at 100°C intervals, 2) capturing thermal signatures of powder alone, 3) using materials capable of withstanding the intended temperatures and able to thermally conduct heat to the powder, 4) mitigating sources of influence from the heater (e.g., the heating source of the heater).

3.3.1 Variable Power Supply

The heater had electrical leads attached to it and part of the design to connect cables from a 9115 Programmable Multi-Range DC Power Supply (B&K Precision, CA, USA) to the heater itself. This power supply was set to different current outputs depending on the steady state temperature wanting to be reached, with a maximum output of 60.5 amps. The power supply can be set to specific amperages by inputting the values and can be manually changed by increments as small as 0.001 amps. The currents were inputted to the power supply to mitigate influences from a gradual change in current output that may not be kept consistent through different experiments.

3.3.2 Heater Design and Iterations

A high-temperature, thermally shock-resistant silicon carbide ceramic block was fabricated and used for the base to house the components without cracking or warping. The insulator was made of an alumina-bisque ceramic rod that is, according to the manufacturer (McMaster-Carr,

CA, USA), easy-to-machine and has a max working temperature of 1,350°C to both machine the desired geometry and work above the temperatures expected to be reached during experimentation. Both the top hat, made of the same material as the insulator, and the top plate, made of the base's material, served similar purposes in preventing the combination of specular and diffuse reflections that make up the reflection process from influencing the pyrometer's measurements, particularly those stemming from the tungsten filament (Bass et al., 1995). Figure 3.4 shows emissions stemming from the filament during the heating of a solid sample, illustrating the need for the top plate to mitigate these sources of influence on the measurements taken by the pyrometer.

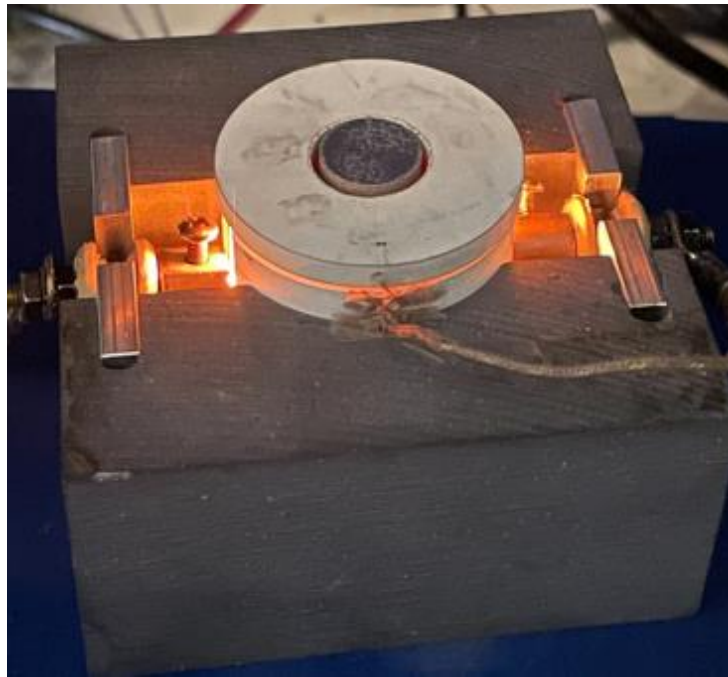


Figure 3.4 Image of tungsten filament emitting while current is passed through

The components of the final design of the heater and their descriptions are shown in Figure 3.5 so that they can accurately be referred to while a blown-up image of the CAD for the original design is shown in Figure 3.6 to illustrate the placement of previous components.

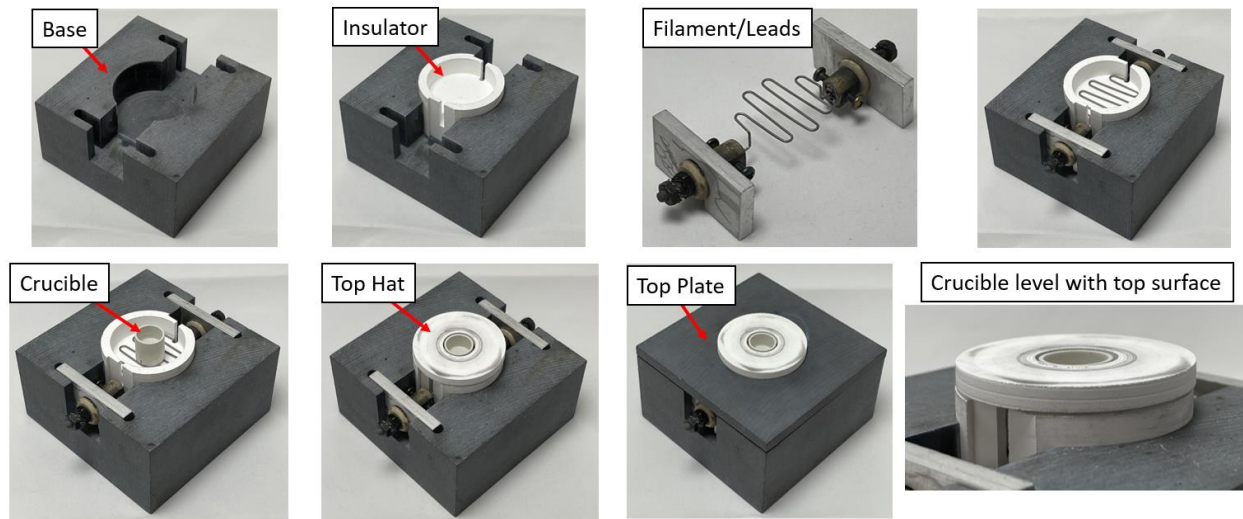


Figure 3.5 Heater components and assembly

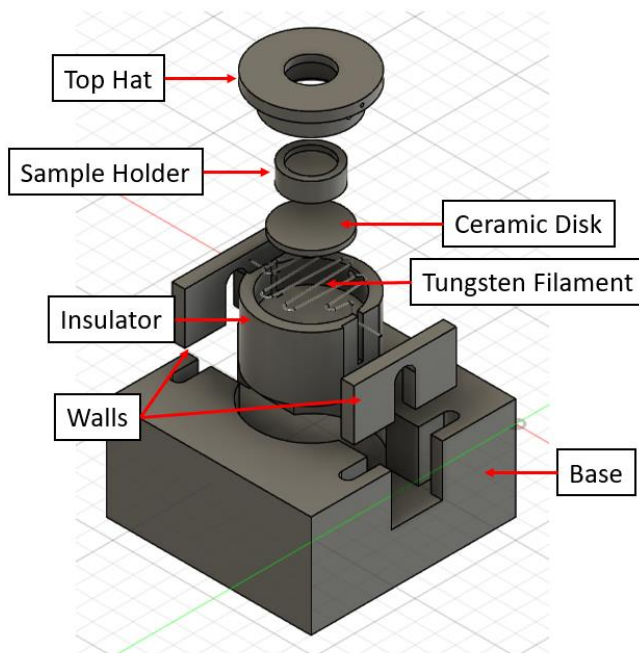


Figure 3.6 Blown-up image of CAD for original heater design

The changes to the design of the heater centered around the source of heating (filament) and design of the substrate (crucible/sample holder and ceramic disk) that held the sample. Redesign considerations for the sample holder came about when the emissivity captured by the FMPI began

to read greater than 1.0. In discussions with the manufacturer of the device (FAR Associates) it was believed that the top hat was increasing the emissivity beyond 1.0 as emissions and reflections from it being heated would reach the target area. An illustration of this influence is shown in Figure 3.7 below.

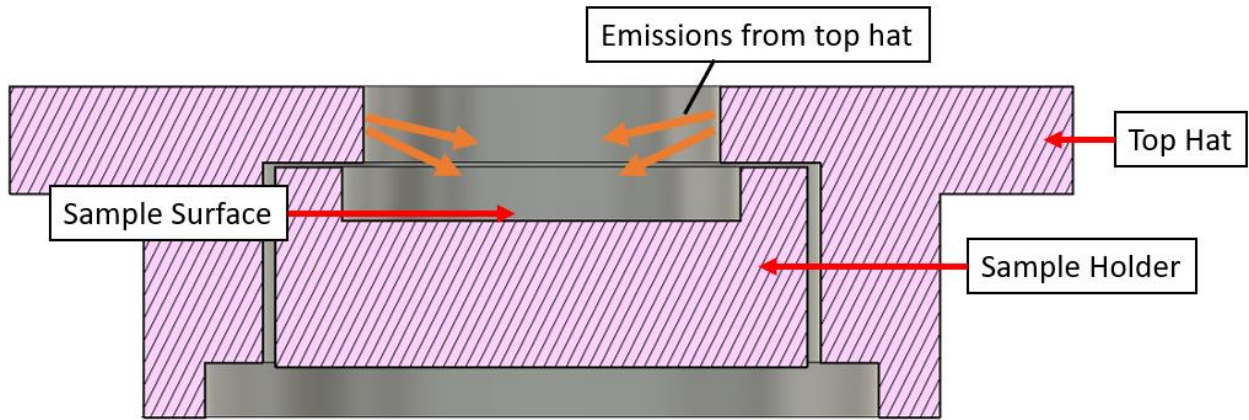


Figure 3.7 Illustration of influence from top hat

A cavity was formed with the top hat surrounding the sample surface, influencing results via internal reflections within the volume immediately surrounding the sample surface. Another issue in the sample holder was the material itself, which was machined out of copper. Although the melting point of copper is $\sim 1,085^{\circ}\text{C}$ and the thermal conductivity higher than most metals ($\sim 342\text{W/m}\cdot\text{K}$) it was melting due to the insulation of the heater and high temperature needed of the sample ($1,000^{\circ}\text{C}$). Before the samples could reach $1,000^{\circ}\text{C}$ it would begin to melt, and a new sample holder had to be machined. Aluminum nitride was eventually chosen as the new sample holder material being that it has a close thermal conductivity to copper ($\sim 321\text{W/m}\cdot\text{K}$) and can withstand temperatures up to $1,870^{\circ}\text{C}$ according to the manufacturer (McMasterr-Carr, CA, USA). Additionally, a redesign of the sample holder to remove the ceramic disk and increase the height of the sample surface was implemented which led to the current “crucible” design shown in Figure 3.8.

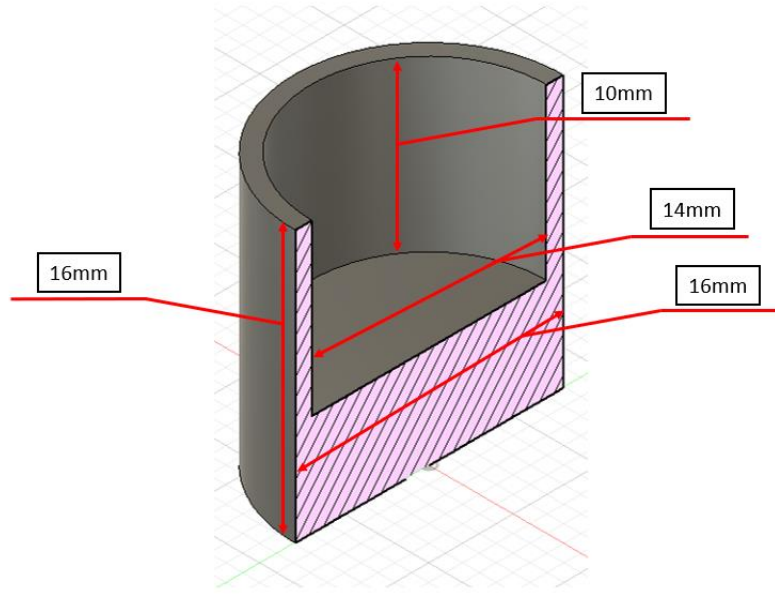


Figure 3.8 Image of crucible and CAD w/ dimensions

Originally, a tungsten filament with a 0.040-inch diameter (Kurt J. Lesker, PA, USA) was used for the experiments, as opposed to the current 0.060-inch diameter filament from the same manufacturer. The 0.040-inch diameter filament provided higher temperatures up to 1,000°C as it was rated at a maximum of 31 amps which the power supply could reach. However, the filament would break within 1 – 2 cycles of heating (~21°C - 1,000°C) when the power supply was set to 50 amps to reach 1,000°C which led to delays in experiments as the heater had to be passed in and out of the glovebox each time it needed to be replaced. There was also a risk in the experiment runs not being completed if the filament were to break before the last measurement. Lastly, a lead time of about two months for the filaments would lead to further delays in the progress of experiments. Therefore, the 0.060-inch diameter rated at a maximum of 71 amps was chosen to mitigate delays while maintaining the same mode and source of heating. Although the filament could not heat the samples to 1,000°C it was able to heat the samples to 600°C.

To check for more sources of influence from the heater, an eSWIR Acuros 1280 GigE eSWIR Camera (SWIR Vision Systems, Durham, NC, USA) was used to capture emissions that may not be easily seen in the visible spectrum, operating between 350nm and 2000nm. An image was captured while a sample of powder was being heated to 450°C. The image with labels can be seen in Figure 3.9.

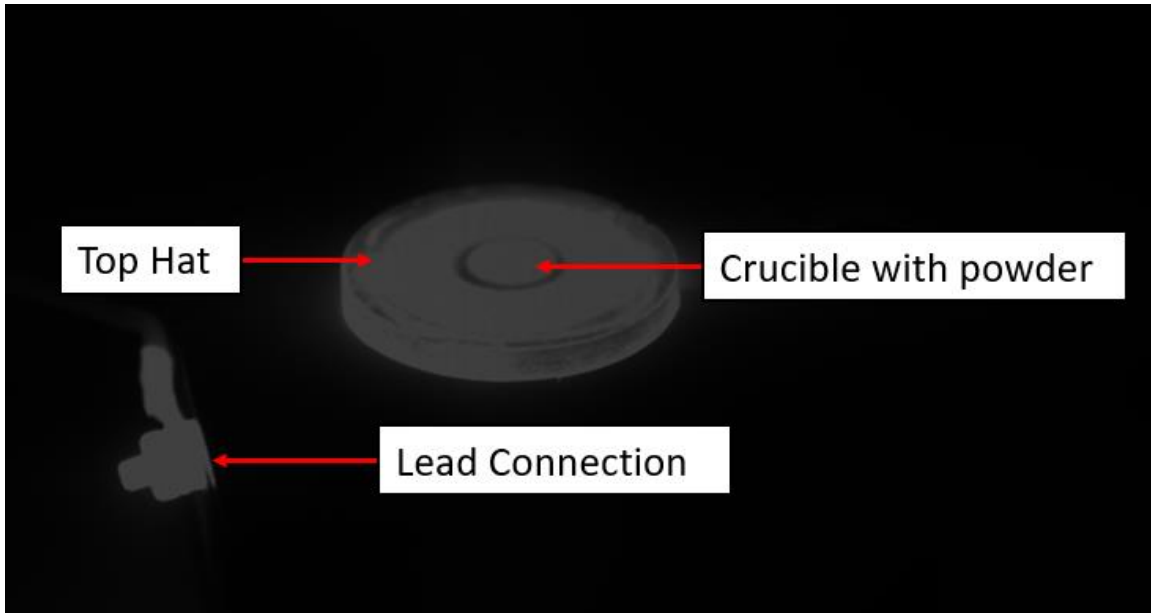


Figure 3.9 IR image of heater with heated sample

Despite the improvements made to the design of the sample holder, it is apparent in this image that sources of emission can stem from sources not clearly visible during experiments. For example, the image shows that not only the top hat and lead connection, but the wire exposed near the lead connection also emits; these sources of emissions can reflect within the environment as it is shown in the illustration in Figure 3.10.

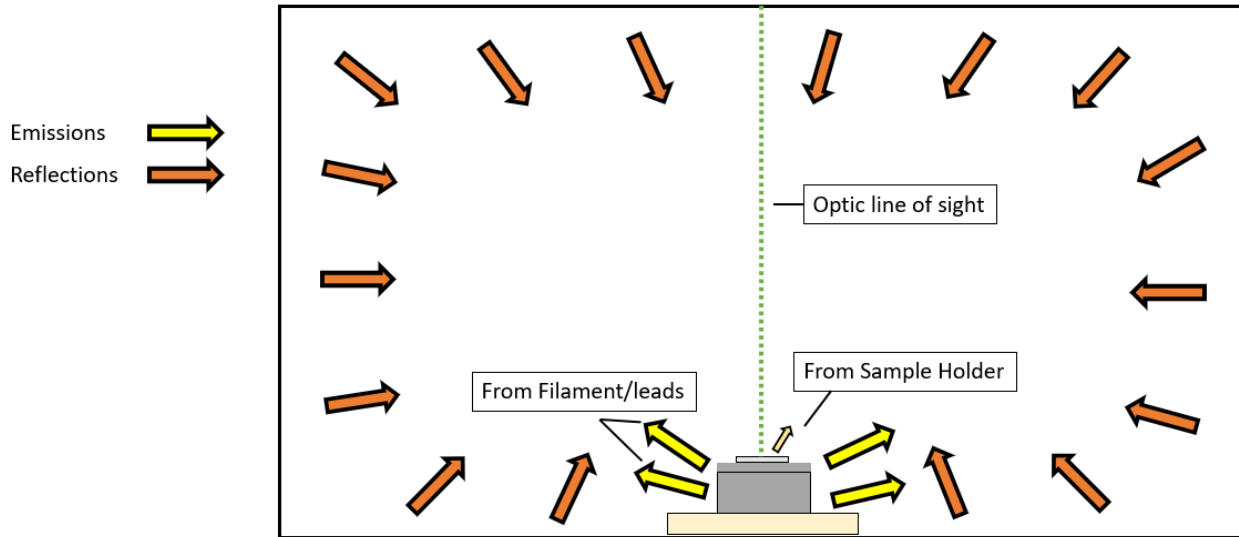


Figure 3.10 Illustration showing emission and reflection interaction within glovebox

It was expected that it would be difficult to isolate the emissions and reflection sources by making alterations to the heater as it would eventually become a source of influence as well. Although the reflections are not as influential as direct emissions, being that they are reduced to due to conservation of energy, onto the target area there is still a need to mitigate these as their influence has not been directly measured.

3.3.3 Pyrometer Optic Fixture

Eliminating sources of radiative environment influence and maintaining an inert environment that would not influence the material's surface were key objectives in the setup of the device in relation to the target. The target area needed to be isolated as much as possible to reduce or eliminate the influence from the environment. In discussions with FAR Associates it was decided a tube extending down to isolate the target area and optic would be best. To accomplish this, a silicon carbide tube was obtained from FAR Associates to be used for the experiments. A fixture that would optically align the pyrometer's optic and tube with the target area needed to be designed and fabricated.

Initially, a fixture that accommodated the optic and tube was designed and printed from a Ender 3 v2 using PLA. The AM process was chosen for rapid prototyping of the fixture before it would be machined. A CAD assembly and an image of the designed fixture are shown in Figures 3.11 and 3.12 respectively.

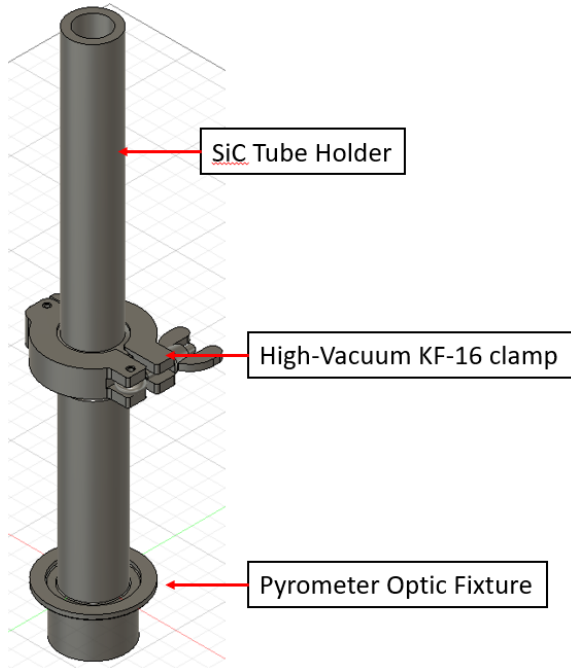


Figure 3.11 CAD image of assembled SiC Tube Holder/Optic Fixture





Figure 3.12 Assembly images of optic fixture

The fixture was designed with a press-fit for the pyrometer's optic so that prototypes could be rapidly manufactured and checked for issues such as aperture obstruction of the optic. The PLA material would flex when the SiC tube was attached to the opposite end, increasing the risk of misalignment between the optic and target area. Images showing the SiC tube with and without support to maintain the alignment with the blackbody source's aperture are shown in Figure 3.13.

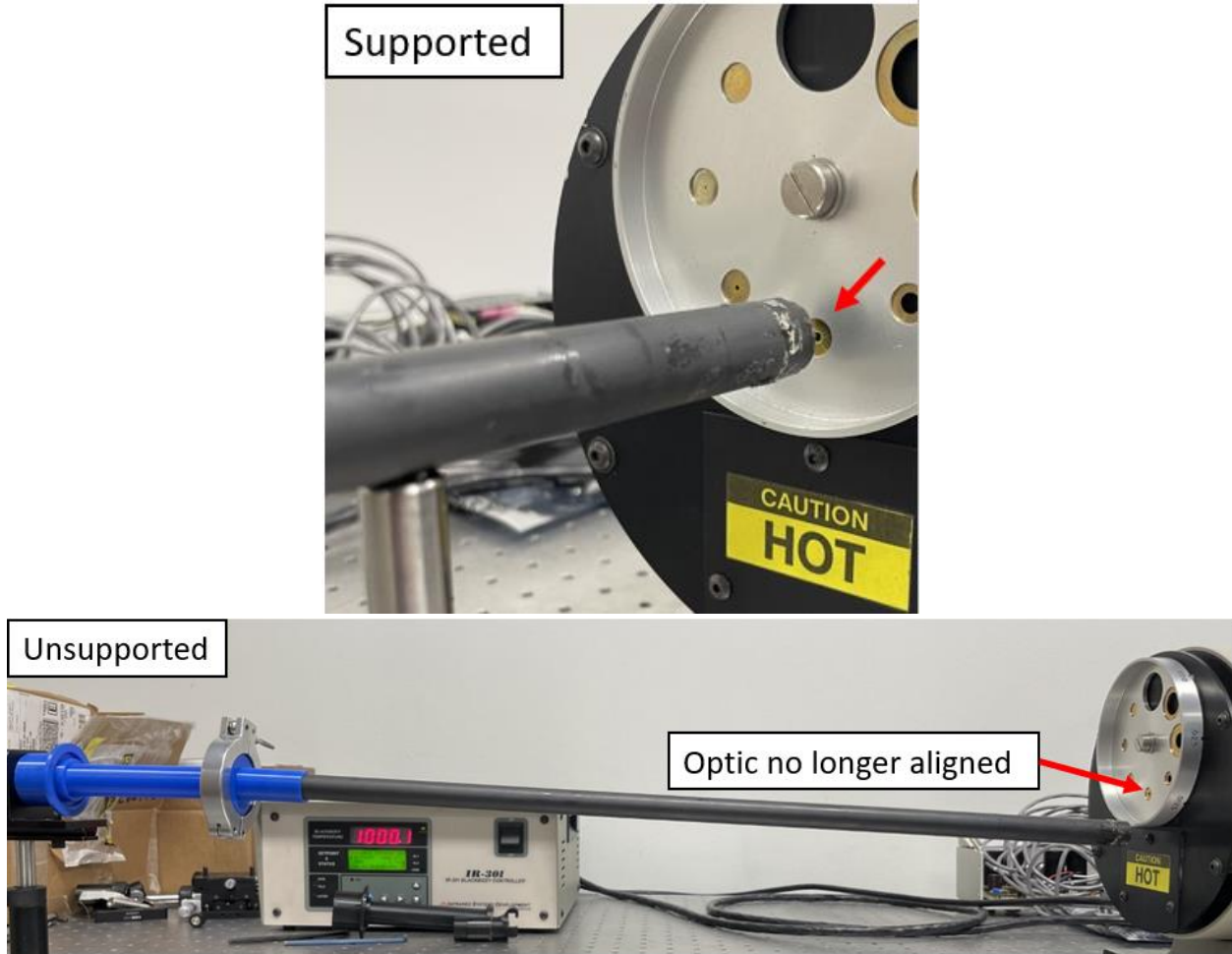


Figure 3.13 Fixture with and without supporting the SiC tube

The PLA material originally used for the design was replaced with WaterShed (Stratasys, Rehovot, Israel) and manufactured using vat photopolymerization. The material was chosen for its strength, having been advertised as being used in wind tunnels, and its pressure-rated use. Due to the material's transmission after being printed, the SiC Tube Holder was spray painted matte black using Kyrton High Heat spray paint (Sherwin-Williams, TX, USA). One benefit of manufacturing the SiC Tube Holder using AM is the ability to interchange tubes of different materials and dimensions. Being that SiC is an expensive and difficult to machine material, the material and tube dimensions can be changed so long as the aperture of the FMPI optic is not obstructed, and the material is at a lower temperature than the target so as not to produce a

greater than 1% influence on the emitted radiation of the target given by the following equation from Fernandez et al. 2021:

$$R\% = \frac{L_2}{L_1} = \frac{\frac{2hc^2}{\lambda^5} * \left(\frac{hc}{e^{\lambda k_B T_T}} - 1\right)^{-1}}{\frac{2hc^2}{\lambda^5} * \left(\frac{hc}{e^{\lambda k_B T_P}} - 1\right)^{-1}} \quad \boxed{3 - 1}$$

Where h is Planck's constant, k_B is Boltzmann's constant, c is the speed of light, λ is the wavelength (m) and the temperatures in Kelvin for the target (L_1) and the source of influence in question (L_2). Variations in measured temperature that exceeded 300°C were found when using uncorrected emissivity values (Rodriguez et al., 2015). Therefore, 1% was chosen as the extent to mitigate these influences as much as possible. The fixture housing the optic was eventually machined out of aluminum and threads added so the optic could be screwed into place and optically aligned better than with the original press-fit design. The fixture housing the SiC tube was extended and kept as a press-fit design with the tube so that it could be replaced if either were to break or need design changes. A CAD and dimensions of the pyrometer final design of the optic assembly and its orientation within the glovebox during experiments is shown in Figures 3.14 and 3.15 respectively.

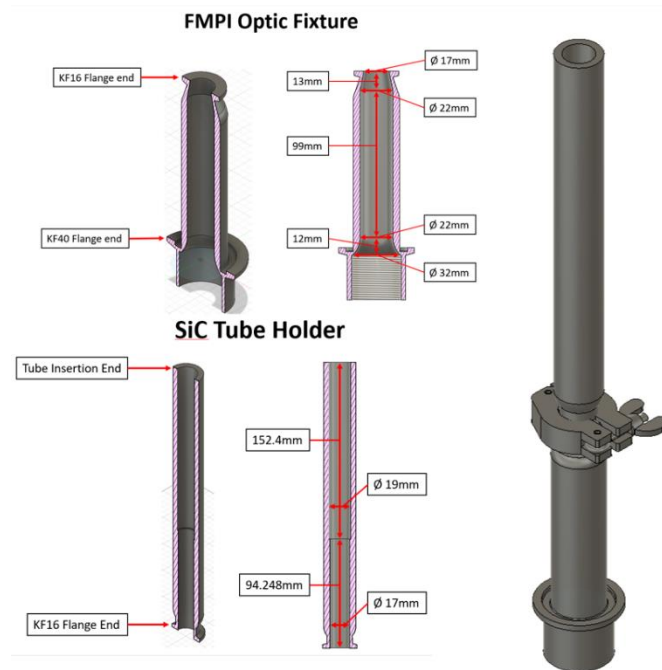


Figure 3.14 CAD and dimensions of pyrometer optic assembly

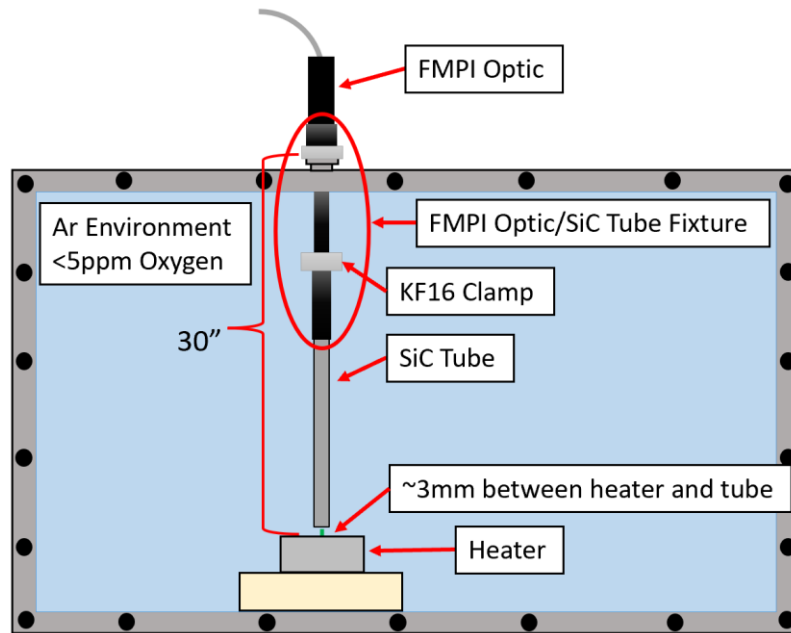


Figure 3.15 Orientation and placement of pyrometer optic, fixture, and SiC tube in glovebox

3.4 FMPI MEASUREMENT METHODOLOGY

The FMPI device captures and stores the spectral emissivity in the .DAT files that have been gathered within the working wavelength range of the device for each temperature measurement. The temperature, tolerance, and signal strength can all be used in the analysis of the target that is being monitored to ensure accuracy in the results obtained. With an exposure time ranging between 4 μ s and 8s, the FMPI automatically adjusts this according to the raw intensity signals it receives. The more photons (above 300°C) pass through the detector, the faster the device will acquire data. For this method the exposure times were set to the minimum and maximum (4 μ s and 8s respectively), meaning the fastest the device can acquire data is 4 μ s; beyond 8s, the FMPI stops the acquisition for that temperature value and begins a new acquisition value until the detector is saturated.

3.5 FMPI CALIBRATION

3.5.1 FMPI Calibration Setup

Calibration for the FMPI is necessary to account for discrepancies between measurements and experiments. To maintain the accuracy of the device, a NIST traceable blackbody (IR-563, Infrared Systems Development Corporation, FL, USA) was used at a steady state temperature of 1,000°C. Through this calibration, the spectral emissivity results are ensured to be accurate between the wavelengths of 1080nm and 1640nm. To account for changes in the optical path, a calibration setup similar to one performed by Fernandez et al. 2021 in an open environment was done within the inert glovebox environment. While placed within the optic fixture, the pyrometer's optic was affixed to the viewport at the top of the glovebox and aimed down into the glovebox while the blackbody was positioned such that it could be aligned with the optic, utilizing the FMPI's alignment laser. Aluminum blocks of equal heights were placed underneath the blackbody to prevent its fan from being blocked by the bottom of the glovebox and potentially causing it to

overheat while also maintaining a level surface. Once the blackbody source was in position and the alignment laser turned on from the FMPI, the apertures on the blackbody were used to align the laser such that they were concentric as it is shown in Figure 3.16.

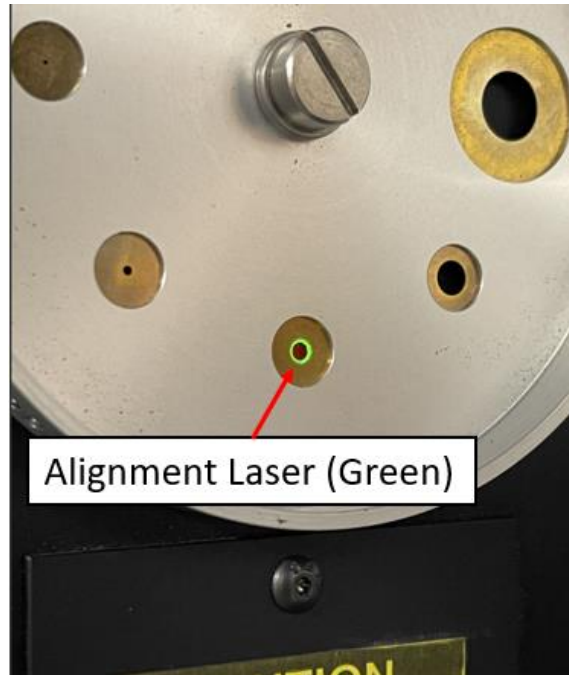


Figure 3.16 Optical alignment of pyrometer alignment laser and blackbody aperture

After alignment, the aperture was opened to the largest diameter and the calibration process continued on the FMPI software once the blackbody reached a temperature of $1,000^{\circ}\text{C}$. Once the blackbody source reached the steady state temperature, the calibration on the software could be performed in which the temperature ($1,000^{\circ}\text{C}$) could be inputted and the FMPI calibrated while looking into the cavity and a steady state temperature. The calibration process described was performed prior to each experiment with a minimum chamber pressure set to 0.5mBar and $<10\text{ppm}$ oxygen levels. An illustration of the calibration setup is shown in Figure 3.17.

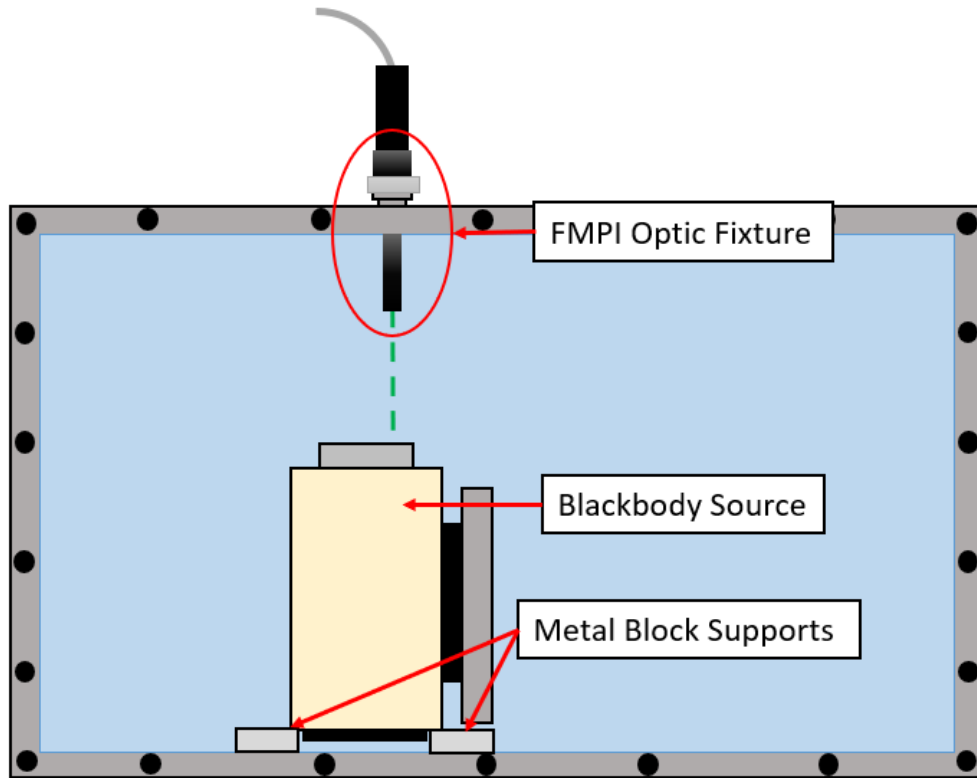


Figure 3.17 Illustration of FMPI calibration setup

3.5.2 Silicon Carbide Tube Aperture Influence

A similar calibration setup in ambient atmosphere was used to check for influence from the tube on the measurements in the event it restricts the optic's aperture. An image of the setup is shown in Figure 3.18.

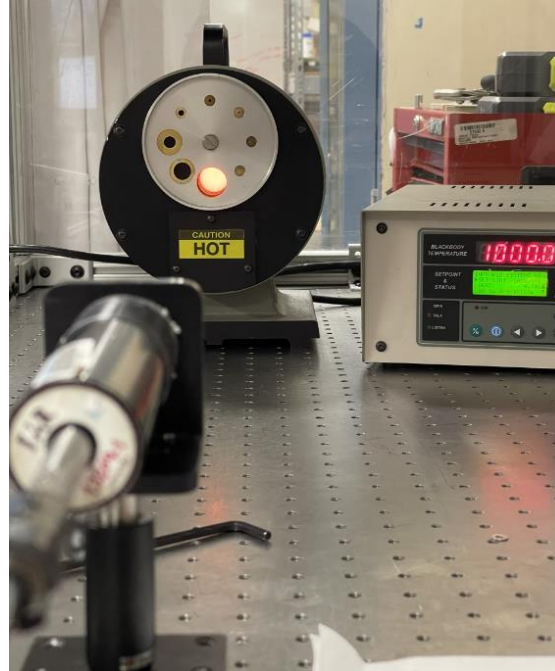


Figure 3.18 Image of aperture influence experiment

The pyrometer was calibrated after being optically aligned to the aperture of the blackbody source once it reached 1,000°C. Once calibrated, the entire assembly was placed over the optic as it is shown in Figure 3.19.



Figure 3.19 Pyrometer optic/SiC tube fixture affixed to optic

Then, after having been calibrated without the fixture and maintaining the alignment of the optic with the blackbody source, the software was started to check for influences from the fixture. Results showed that there was no impact to the emissivity recorded before or after the placement of the fixture, indicating there would be no impact while the device captures measurements.

3.6 EXPERIMENTAL SETUP

3.6.1 Powder Sample Preparation

Comparing emissivity results of the experiments requires a repeatable sample preparation method since emissivity values can differ depending on the sample's surface (Wu et al., 2021). Therefore, a sample preparation method is derived from the ASTM B213-20 and ASTM-B527 test method for flow rate of metal powders using the Hall Flowmeter and apparent and tap density respectively. The crucible is placed below the funnel to catch the powder as it flows out. The method describes using the Hall Flowmeter, shown in Figure 3.20, and pouring powder into the funnel, using a straight edge to cover the opening at the bottom.

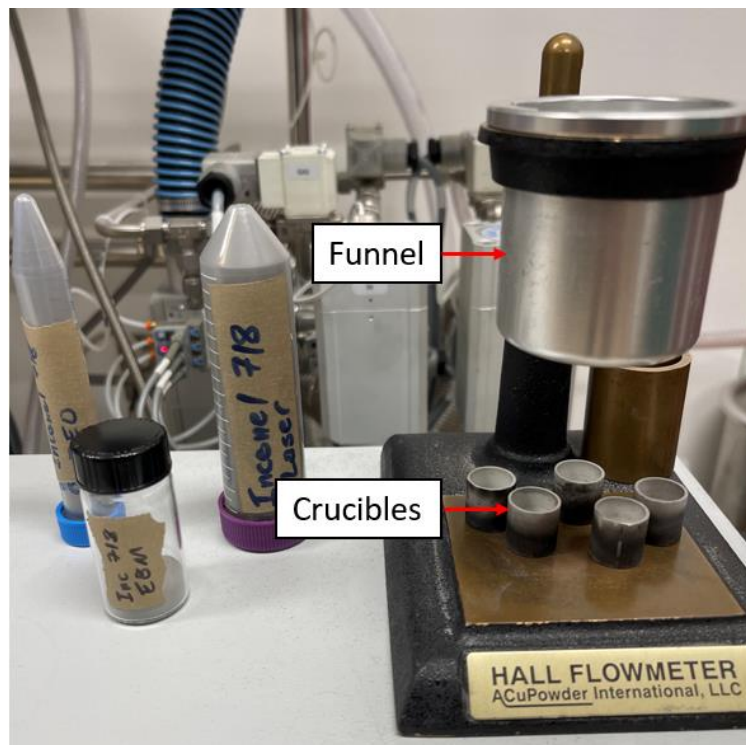


Figure 3.20 Hall Flowmeter with funnel and crucibles

Once the powder is poured into the funnel, the straight edge is removed and the powder flows into the crucible below it. For the apparent density, the straight edge is then dragged across the top of the crucible. For the tap density, the crucible is tapped 40 times on its side using the same

straight edge and afterwards the straight edge is dragged across the top. The sample preparation is performed within the glovebox to reduce shaking or tapping the crucible so as not to further compact it, and in the same respect being careful to only drag the straight edge across the crucible without pressing down on the powder.

3.6.2 Capturing Measurements and Emissivity

The FMPI optic and its fixture is placed at the top of the glovebox, normal to the viewport's opening. Images of the setup with the FMPI Optic Fixture and SiC Tube Holder both in place are shown in Figure 3.21.

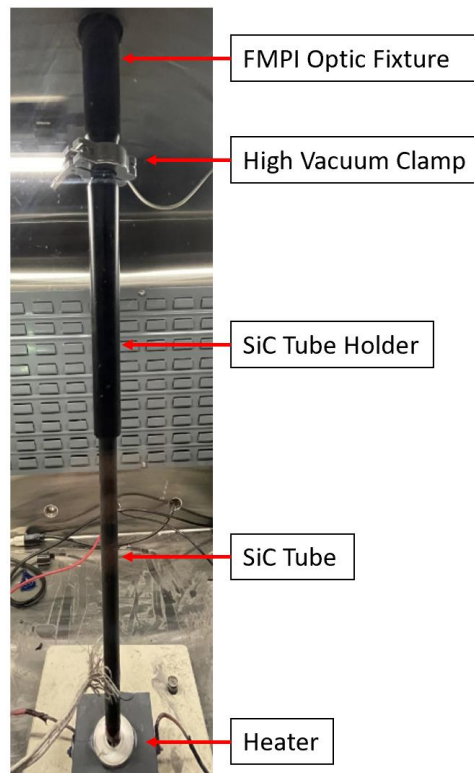


Figure 3.21 Fully assembled FMPI optic fixture and SiC tube holder

A ceramic plate was placed below the heater to maintain the optic's 30" (762mm) focal length. The SiC tube is attached to the opposite end of the optic's fixture and the alignment laser is used to make the line of sight of the optic concentric with the powder's surface as shown in Figure 3.22.

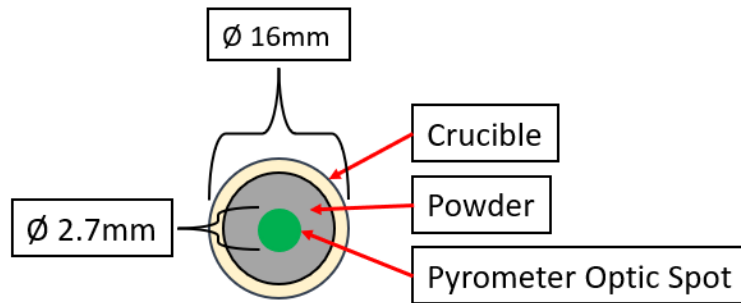


Figure 3.22 Aligning of pyrometer optic and powder surface

The FMPI optic is aligned using its alignment laser such that the optic, tube, and crucible are concentric as shown in Figure 3.23.

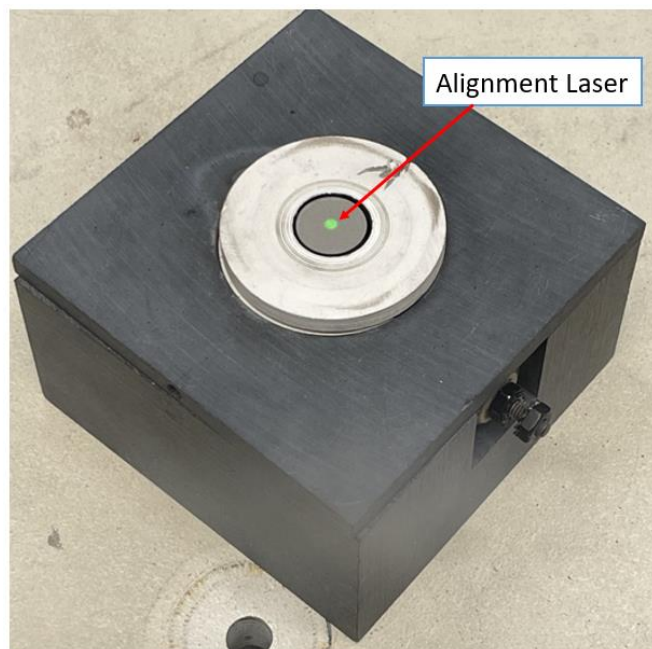


Figure 3.23 Alignment of laser with target

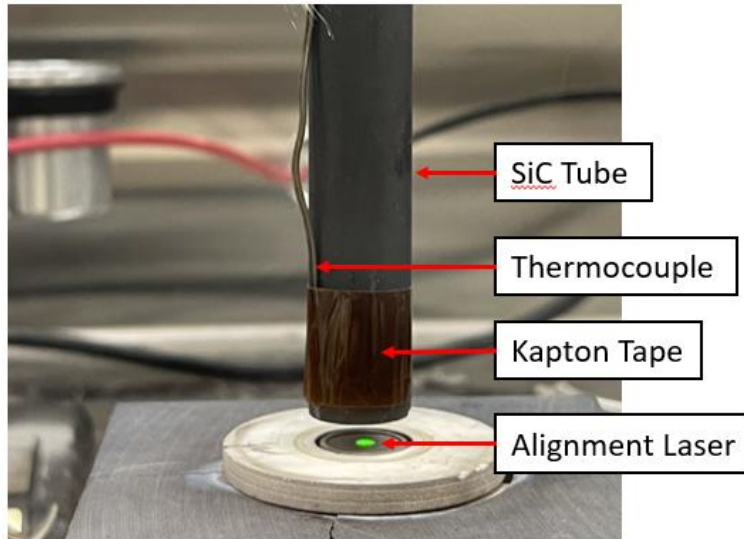


Figure 3.24 Fully assembled fixture and tube with alignment laser visibly unobstructed

Ensuring that the alignment laser is not visibly obstructed, as it is shown in Figure 3.24, the FMPI software is started before the power supply so that the data can be captured as soon as the target begins to emit, at which point the pyrometer can begin gathering the raw intensity. Once the pyrometer optic is aligned, the tube is set in place and the software log rate is set to “All” to gather as many temperature values as possible, only being restricted by the raw intensity the pyrometer can gather. It is important for the target to maintain a steady state temperature prior to taking measurements to isolate variables that may come from heating or cooling. The powder needs to be heated slowly to prevent an “overshooting” of the temperature. To achieve this, the power supply is turned on and set to 45 amps to begin heating the powder. Initially, waiting about 60 minutes for the powder to heat up before increasing the amps by 1 amp each 15 minutes. Once the pyrometer reads that the target is at $400^{\circ}\text{C} \pm 1^{\circ}\text{C}$ for a continuous time of 5 minutes, the current is maintained at that level as data is recorded for 2 minutes. For each two-minute measurement, the FMPI’s software is closed and restarted so that the data acquisition is of the intended temperature alone. After those two minutes, the power supply is set to 54 amps to

continue heating while the temperature can be monitored by the FMPI software in real-time. If after another 60 minutes, the powder is not yet at 500°C, the amps are again increased by small increments of about 0.05 amps each 15 minutes. Once the pyrometer reads the target is at 500 ±1°C for a continuous 5 minutes, the current is once again maintained at that level. Once the two minutes of data are gathered, the power supply is again set to 58amps and a similar procedure when heating to 500°C is followed to reach 600°C. For the procedure, the amperage is increased by 0.02amps instead of 0.05amps if 600°C is not reached within 60 minutes. After the final gathering of data at 600°C, the power supply is turned off. The maximum temperature the tube can reach before >1% influence is seen was calculated to be 180°C while the powder is at 400°C (the first temperature for data acquisition) and 280°C when the powder reaches 600°C. Experiments were performed to measure the temperature of the tube throughout the experiment and results are presented in Chapter 4.

CHAPTER 4: RESULTS AND DISCUSSIONS

4.1 INTRODUCTION

The results in this chapter include the emissivity values extracted from the three different Inconel 718 powder size distributions that were tested at three different temperatures. Within literature there are emissivity values that depend on temperature, the wavelength the measurement was taken at, chemistry, and characteristics of the surface (smooth, rough, etc.) (Barreira et al., 2021). A direct comparison between emissivity values cannot be made unless the same conditions previously mentioned are met for each measurement; however, general trends in the emissivity's behavior with variables like temperature and morphology can be made between different setups and examples of these trends will be mentioned throughout this chapter. Measurements were taken for each of the particle size ranges from $\sim 400^{\circ}\text{C}$ to $\sim 600^{\circ}\text{C}$ and a steady state temperature ($\pm 2.7^{\circ}\text{C}$ per 2-minute data acquisition) reached before each of the measurements at the three different temperatures. Analysis of the particle size distribution and surface images taken in a microscope follow the emissivity values gathered.

Data for the 2-minute acquisition was gathered at each steady state temperature of 400°C , 500°C , and 600°C . The .log files were used to show the emissivity at a single wavelength (1500nm) at a given temperature across the entire 2 minutes. The "sequence" to be plotted on some graphs is the number given to the .DAT file that was captured as measurements were taken. Figure 4.1 shows representative examples of the .log and .DAT files with names for the columns produced. The amount of .log files is directly related to the exposure time, meaning that there are more .log files for the lower exposure times (i.e. data taken at 400°C).

.log file for PSD – 1 Powder at 600°C

Sequence	Date	Time	Temp	Tol	Signal Strength	Exposure Time
1	10/27/2022	50:34.1	602.2	3.11	0.456	0.729856
2	10/27/2022	50:34.9	601.4	3.13	0.455	0.729856
3	10/27/2022	50:35.6	601.2	3.18	0.454	0.729856
4	10/27/2022	50:36.3	601.2	3.19	0.454	0.729856

.DAT file for Sequence 1 of PSD – 1 Powder at 600°C

Wavelength (nm)	Raw Intensity	Noise	Corrected Intensity	Emissivity
1080	3457.28	2404.93	435.931	0.494725
1081.56	3293.54	2133.02	466.953	0.522173
1083.13	3167.34	1912.12	492.311	0.542497
1084.69	3168.84	1865.14	502.224	0.545375

Figure 4.1 Example of .log and .DAT files extracted from FMPI and put into Excel

Along with some time stamps of the data collection, the temperature, tolerance, exposure time, and signal strength (the emissivity at 1500nm) are all displayed in the .log files. Within the .DAT files the spectral emissivity can be found with the intensities calculated at each wavelength. The raw intensity is the raw signal captured by the pyrometer prior to any calculations accounting for noise. The calculated noise is then displayed which gives a metric to light intensities not considered by the pyrometer in its emissivity or temperature calculation. Finally, the corrected intensity is calculated by the pyrometer after considering the raw intensity and background noise. An important distinction to note between raw and corrected intensity is that the pyrometer utilizes the raw intensity to signal the acquisition of data. This means that raw intensities above 20000 counts will trigger the acquisition of a .DAT file.

4.2 DATA ANALYSIS METHODS

The wavelengths to be included in the analysis were between 1080nm and 1640nm since the FMPI was calibrated between these wavelengths; therefore, those below and above were excluded from any analysis. For a blackbody, the intensity peak of the emitted spectrum shifts to

shorter wavelengths as temperature increases (Britannica, 2020). An illustration of this relationship is shown in section 2.4. This shift in intensity peaks means that noise gathered by the pyrometer would more heavily influence the results at lower temperatures and shorter wavelengths. To account for this, the “signal strength” is used in the analysis of the results to maintain a constant wavelength to compare individual results. The signal strength shown by the FMPI can be defined as the emissivity at 1500nm with no environmental influence, calibrated optical path and a known target. The caveats mentioned are all accounted for in the calibration technique described in section 3.6.

4.3 ORDER OF EXPERIMENTS

Table 4.1 shows the numbers assigned to each experiment with the particle size distribution and sample preparation method.

Table 4.1 Numbers assigned to each experiment run

Particle Size Distribution	Apparent Density	Tap Density
PSD – 1	1	2
	3	4
	5	6
PSD – 2	7	8
	9	10
	11	12
PSD – 3	13	14
	15	16
	17	18

Once a number was assigned to each experiment, random.org was used to generate a random sequence of numbers. Random.org uses randomness derived from atmospheric noise, as opposed to a pseudo-random number algorithm typically used in computer programs. Using its “sequence generator” the following sequence of numbers in Table 4.2 was outputted and carried out in order from top-to-bottom.

Table 4.2 Output of random sequence generator

13	PSD – 3 (Apparent Density)
17	PSD – 3 (Apparent Density)
15	PSD – 3 (Apparent Density)
12	PSD – 2 (Tap Density)
10	PSD – 2 (Tap Density)
16	PSD – 3 (Tap Density)
4	PSD – 1 (Tap Density)
14	PSD – 3 (Tap Density)
11	PSD – 2 (Apparent Density)
9	PSD – 2 (Apparent Density)
7	PSD – 2 (Apparent Density)
2	PSD – 1 (Tap Density)
1	PSD – 1 (Apparent Density)
3	PSD – 1 (Apparent Density)
6	PSD – 1 (Tap Density)
5	PSD – 1 (Apparent Density)
18	PSD – 3 (Tap Density)
8	PSD – 2 (Tap Density)

The “Separate Operator Run” column labeled in the data to be shown were experiments carried out by another operator. Like the experimental order design just described, Table 4.3 shows the

sequence output by random.org for a single run of each particle size distribution and their sample preparation method to be carried out by the separate operator.

Table 4.3 Output sequence of experiments for other operators

PSD – 2 (Tap Density)
PSD – 1 (Apparent Density)
PSD – 2 (Apparent Density)
PSD – 3 (Tap Density)
PSD – 1 (Tap Density)
PSD – 3 (Apparent Density)

The intent of this run of experiments from another trained operator was to receive feedback for moments in the sample preparation, calibration, or SiC tube placement that could yield human error and be corrected or mitigated. Another goal of these runs was to check for biases in the results originally obtained. The sample preparation method, temperatures, and particle size distributions were eventually selected for a total of 3 operators, 2 particle size distributions, 2 temperatures and 1 sample preparation method to account for variability between operators. Table 4.4 shows the numbers assigned to each operator, particle size distribution and experiment run number while Table 4.5 shows the sequence outputted by random.org. Justifications for the experimental design are discussed in the following sections.

Table 4.4 Numbers assigned to each operator/PSD/Run combination

Operator	Particle Size Distribution	Assigned Number
Operator 1	PSD – 1	1
	PSD – 3	2
Operator 2	PSD – 1	3
	PSD – 3	4
Operator 3	PSD – 1	5
	PSD – 3	6
Operator 1	PSD – 1	7
	PSD – 3	8
Operator 2	PSD – 1	9
	PSD – 3	10
Operator 3	PSD – 1	11
	PSD – 3	12
Operator 1	PSD – 1	13
	PSD – 3	14
Operator 2	PSD – 1	15
	PSD – 3	16
Operator 3	PSD – 1	17
	PSD – 3	18

Table 4.5 Order of experiments for each operator/PSD combination

Operator	Particle Size Distribution
Operator 1	PSD – 3
Operator 1	PSD – 1
Operator 2	PSD – 3
Operator 1	PSD – 1
Operator 1	PSD – 3
Operator 3	PSD – 3
Operator 3	PSD – 1
Operator 1	PSD – 1
Operator 2	PSD – 1
Operator 3	PSD – 3
Operator 2	PSD – 3
Operator 2	PSD – 1
Operator 3	PSD – 1
Operator 1	PSD – 3
Operator 2	PSD – 1
Operator 3	PSD – 1
Operator 3	PSD – 3
Operator 2	PSD – 3

4.4 PARTICLE SIZE DISTRIBUTION

A particle size distribution analysis was performed on the three different powders using a CAMSIZER X2 (Microtrac MRB, PA, USA). The CAMSIZER X2 provides particle size analysis from 0.8 to 8mm with Dynamic Image Analysis (ISO 13322-2). Using both a zoom and basic camera, fine and larger particles can be analyzed with an algorithm that combines the information provided by both cameras. The results of the analysis are shown in Figure 4.2.

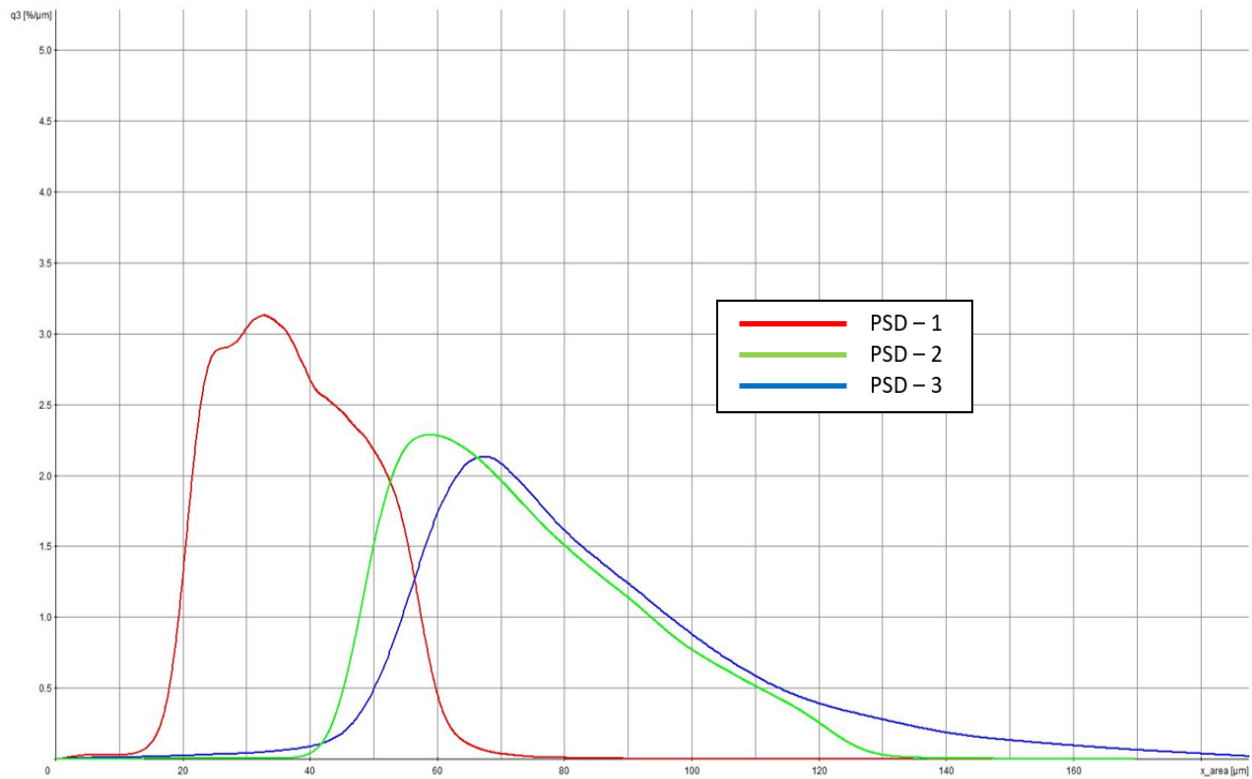


Figure 4.2 Particle size distribution results for each powder

The results correspond to what was expected from the manufacturer's specifications of the particle size distributions for the different particle size diameters previously given in Table 1.1. According to the plot, a qualitative conclusion can be made that the particle size distribution for PSD – 1 is less than that of PSD – 2 and PSD – 3. This is important to note being that Zhang et al. 2018 showed that the thermal conductivity of the powder counterparts of solid Inconel 625 and Ti64

were much lower within the 100°C and 500°C ranges that were researched (Zhang et al., 2018). Furthermore, heat transfer between contacting solid particles in gas are limited by the points of contact which likely contributed to the lack of heating from PSD – 1 (Gusarov & Kovalev, 2009).

4.5 SILICON CARBIDE TUBE INFLUENCE

To account for radiative environment influence stemming from the silicon carbide tube used in the experiments, a thermocouple was placed at the tip of the tube as it is shown in Figure 3.10 and set to acquire the temperature each second. The results for 4 different experiment runs where the powder was heated are plotted in a scatter plot in Excel alongside the maximum allotted temperature before >1% influence is reached and shown in Figures 4.3 – 4.6.

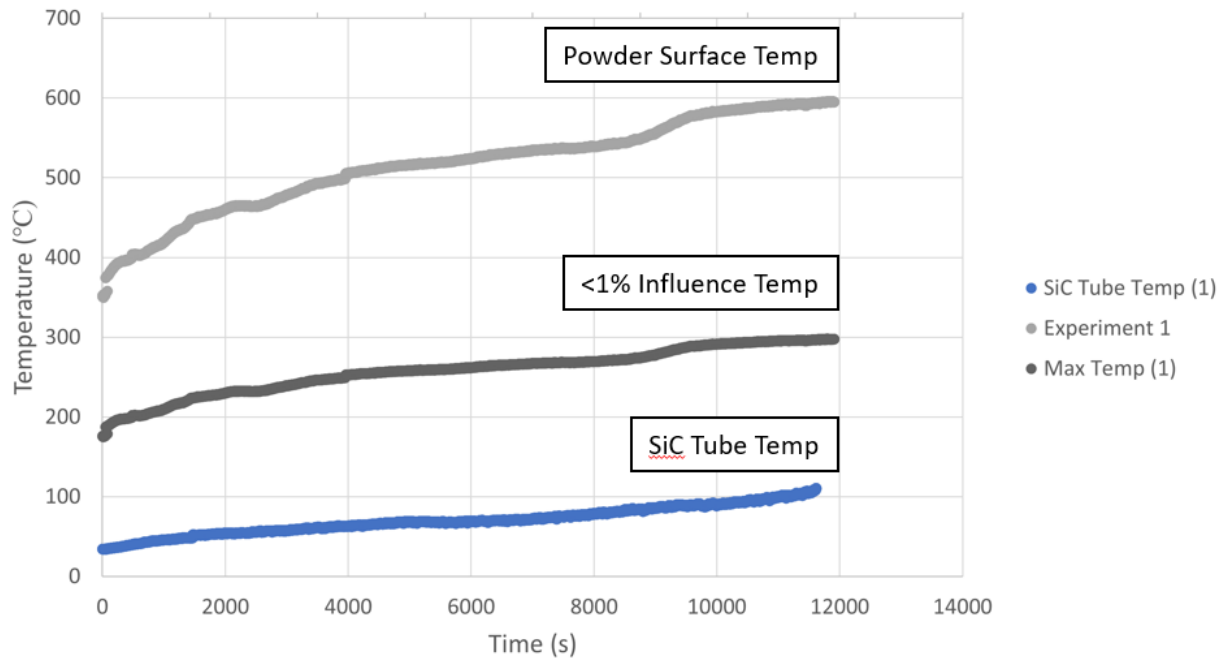


Figure 4.3 Powder surface temp. v SiC tube temp. for PSD – 2 (Apparent)

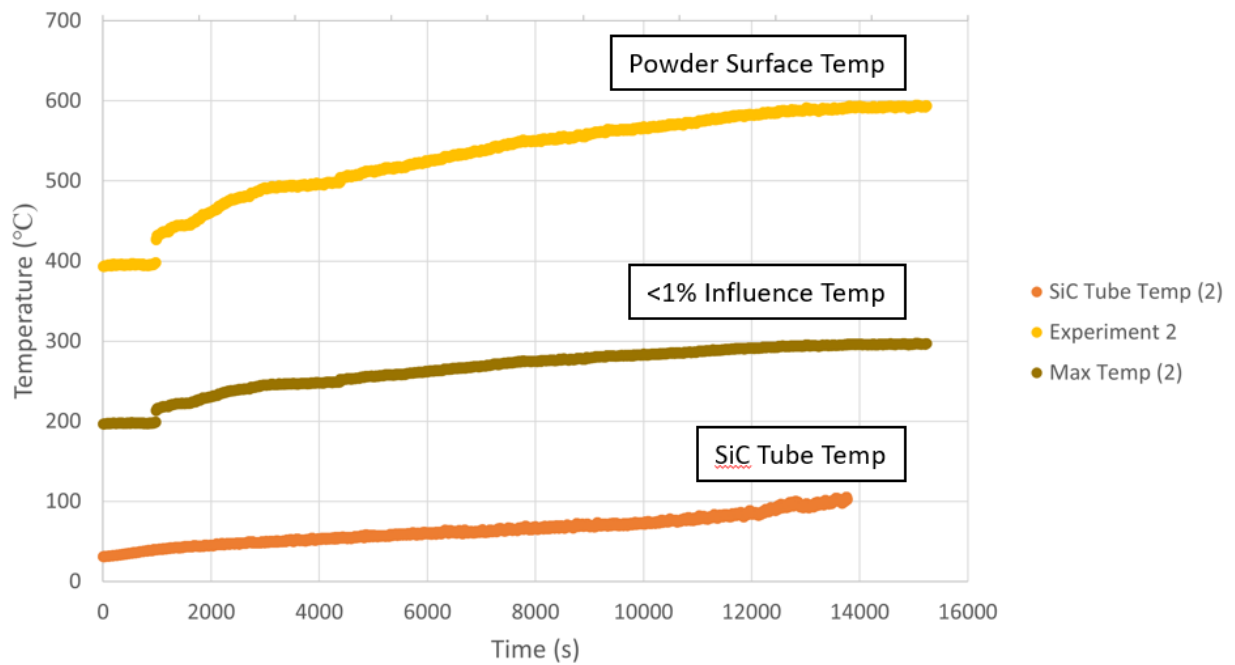


Figure 4.4 Powder surface temp. v SiC tube temp. for PSD – 3 (Apparent)

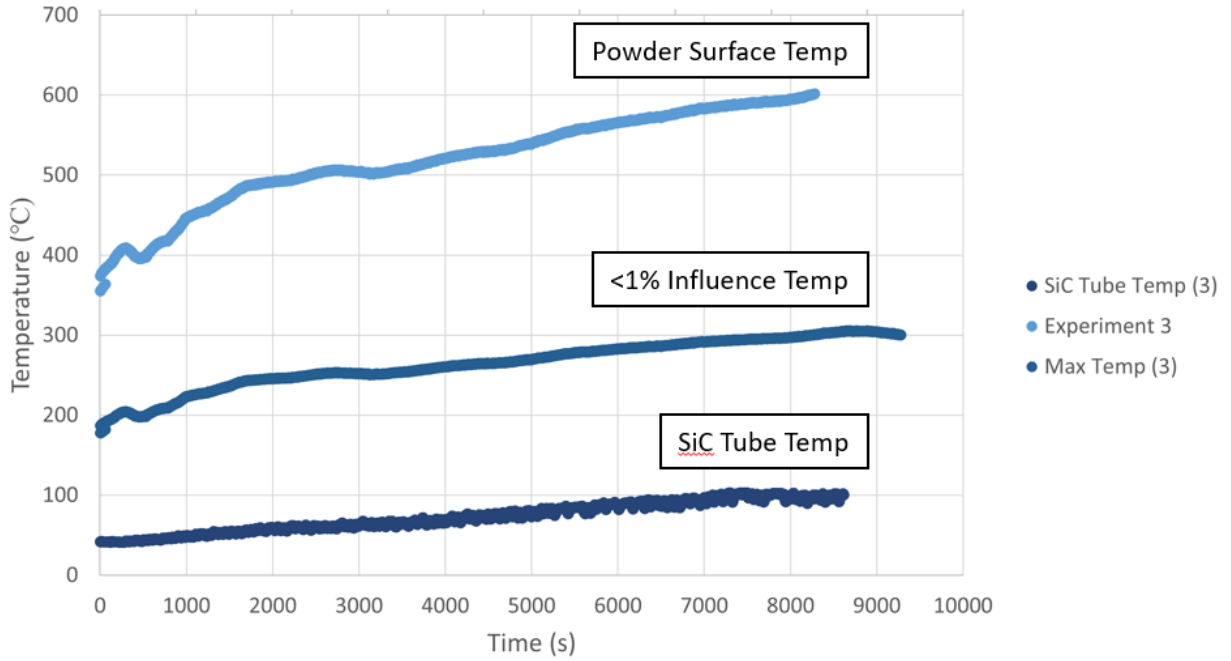


Figure 4.5 Powder surface temp. v SiC tube temp. for PSD – 3 (Tap)

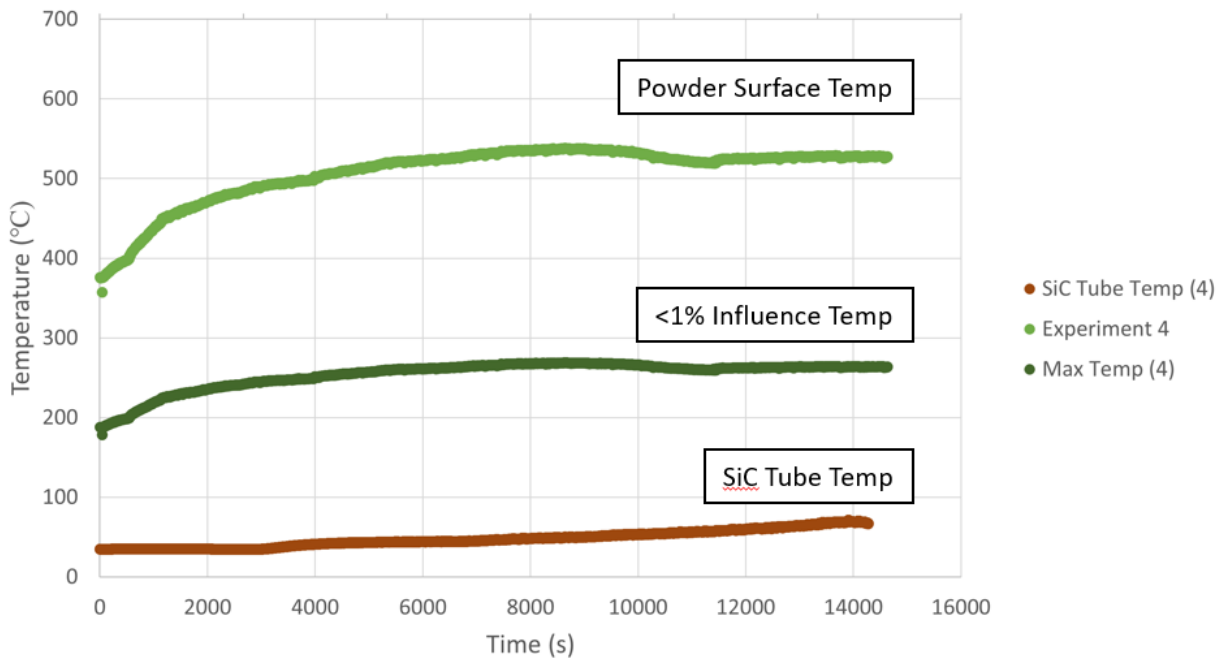


Figure 4.6 Powder surface temp. v SiC tube temp. for PSD - 1 (Tap)

The results show that the tube does not get hot enough to influence the results >1% using the equation and temperatures calculated in section 3.4. Considering a theoretical contribution of 1% equates to $\sim 5^{\circ}\text{C}$ on the measurement, the SiC tube temperature throughout experimentation is considered negligible on the measurements captured. The Kapton tape used was also rated up to 250°C and did not degrade while it was placed on the tube as further, non-quantitative, evidence. The results for experiment 4 show a lower maximum temperature reached than the rest because the experiment corresponds with the instance in which the maximum temperature reached by the powder was only 530°C . Therefore, not reaching the same maximum temperature as the other experiments plotted.

4.6 EMISSIVITY RESULTS

The average signal strength at $\sim 1500\text{nm}$ for each 2-minute acquisition of data during experiments carried out by a single operator (Run 1 – 3) were calculated to the second decimal point and are shown in Table 4.6, along with its deviation within that time.

Table 4.6 Average signal strength for each acquisition of data

Sample Preparation	Temperature	Run 1	Run 2	Run 3
PSD - 1 Tap Density	400°C	0.49 ± 0.00	0.53 ± 0.00	0.54 ± 0.00
	500°C	0.49 ± 0.00	0.50 ± 0.00	0.54 ± 0.00
	600°C	0.49 ± 0.00	0.50 ± 0.01	0.51 ± 0.01
PSD - 1 Apparent Density	400°C	0.51 ± 0.01	0.52 ± 0.00	0.58 ± 0.00
	500°C	0.47 ± 0.00	0.48 ± 0.00	0.53 ± 0.00
	600°C	0.48 ± 0.00	0.50 ± 0.00	0.53 ± 0.00
PSD - 2 Tap Density	400°C	0.59 ± 0.00	0.58 ± 0.01	0.57 ± 0.00
	500°C	0.55 ± 0.00	0.56 ± 0.00	0.53 ± 0.00
	600°C	0.54 ± 0.00	0.56 ± 0.01	0.54 ± 0.01
PSD - 2 Apparent Density	400°C	0.57 ± 0.01	0.56 ± 0.00	0.58 ± 0.00
	500°C	0.53 ± 0.00	0.52 ± 0.00	0.54 ± 0.00
	600°C	0.51 ± 0.00	0.52 ± 0.00	0.53 ± 0.00
PSD - 3 Tap Density	400°C	0.57 ± 0.00	0.54 ± 0.00	0.60 ± 0.00
	500°C	0.54 ± 0.00	0.50 ± 0.00	0.56 ± 0.00
	600°C	0.54 ± 0.00	0.50 ± 0.01	0.55 ± 0.01
PSD - 3 Apparent Density	400°C	0.54 ± 0.01	0.42 ± 0.00	0.52 ± 0.00
	500°C	0.53 ± 0.00	0.47 ± 0.00	0.52 ± 0.00
	600°C	0.54 ± 0.00	0.48 ± 0.00	0.52 ± 0.00

Table 4.7 shows a single run done by a separate operator performing the experiments once for the first time for each sample preparation method.

Table 4.7 Results for separate operator run for each sample preparation method

Sample Preparation	Temperature	Separate Operator Run
PSD - 1 Tap Density	400°C	0.50 ± 0.00
	500°C	0.47 ± 0.00
	600°C	0.43 ± 0.01
PSD - 1 Apparent Density	400°C	0.83 ± 0.01
	500°C	0.72 ± 0.01
	600°C	0.72 ± 0.00
PSD - 2 Tap Density	400°C	0.54 ± 0.01
	500°C	0.50 ± 0.01
	600°C	0.52 ± 0.01
PSD - 2 Apparent Density	400°C	0.56 ± 0.01
	500°C	0.53 ± 0.01
	600°C	0.53 ± 0.00
PSD - 3 Tap Density	400°C	0.56 ± 0.00
	500°C	0.53 ± 0.00
	600°C	0.54 ± 0.01
PSD - 3 Apparent Density	400°C	0.40 ± 0.01
	500°C	0.47 ± 0.01
	600°C	0.49 ± 0.00

The PSD – 1 results highlighted in yellow and red are instances in which the temperatures reached were $\leq 20^{\circ}\text{C}$ and $\leq 50^{\circ}\text{C}$, respectively, than the intended 600°C and the actual temperatures reached are shown in Table 4.8. It is expected that the temperature was not reached due to a reduced thermal conductivity compared to the other particle size distributions that is discussed later in the section.

Table 4.8 Temperatures reached for PSD – 1

Sample Preparation	Temperature	Run 1	Run 2	Run 3	Separate Operator Run
PSD - 1 Tap Density	600°C	580°C	581°C	574°C	530°C
PSD - 1 Apparent Density	600°C		576°C	565°C	580°C

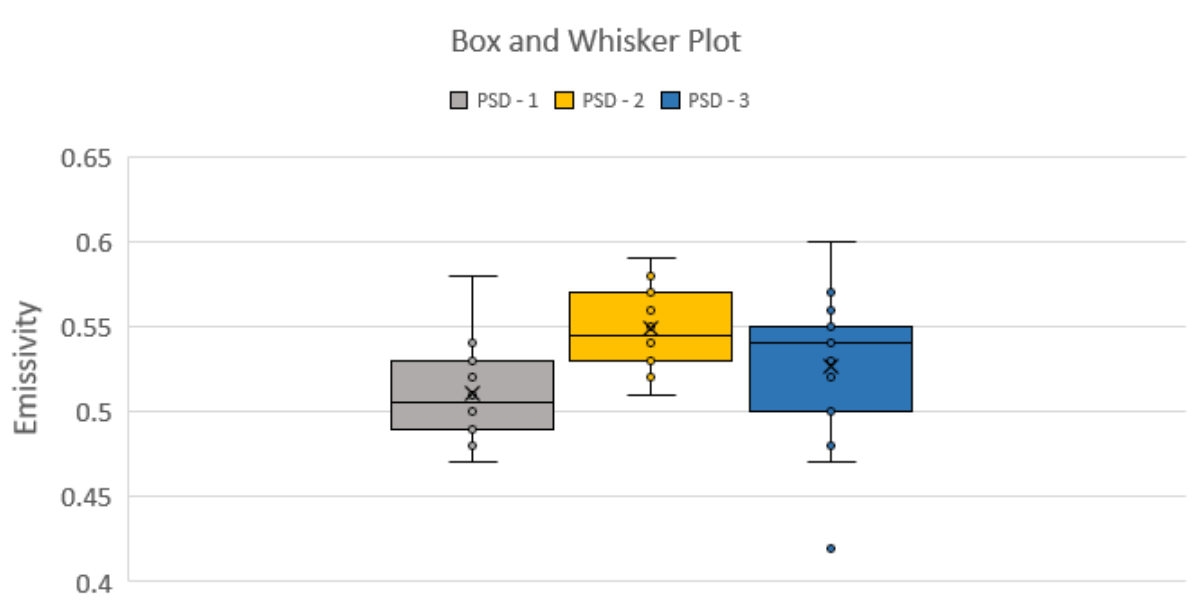


Figure 4.7 Box and whisker plots of all values for each particle size distribution

Given that there is no previous data to refer to regarding the emissivity of powder, statistical significance of the measured emissivity values was determined via hypothesis testing. A box and whisker plot was produced in Excel with the values from runs 1 - 3 for each of the particle size distributions and is shown in Figure 4.7. The plot point at ~ 0.42 for PSD – 3 extends outside the range of the plot for the particle size distribution and is considered an outlier. To confirm a Chi-squared test for outliers was performed using R studio with emissivity values grouped by particle

size distributions as the test offers overall assessments of the presence of outliers that impact latent and manifest variables (You et al., 2020). The results are shown in Table 4.9.

Table 4.9 Hypothesis testing results for chi-squared test

<div style="border: 1px solid black; display: inline-block; padding: 2px;">PSD – 1</div>
P – value: 0.011 Alternative hypothesis: highest value 0.58 is an outlier
P – value: 0.141 Alternative hypothesis: lowest value 0.47 is an outlier
<div style="border: 1px solid black; display: inline-block; padding: 2px;">PSD – 2</div>
P – value: 0.080 Alternative hypothesis: highest value 0.59 is an outlier
P – value: 0.098 Alternative hypothesis: lowest value 0.51 is an outlier
<div style="border: 1px solid black; display: inline-block; padding: 2px;">PSD – 3</div>
P – value: 0.068 Alternative hypothesis: highest value 0.60 is an outlier
P – value: 0.011 Alternative hypothesis: lowest value 0.42 is an outlier

A significance value of 0.05 was used to accept or reject the hypothesis that there are no outliers (H_0). There was a significant amount of evidence that the highest value of PSD – 1 and lowest value of PSD – 3 were outliers. Therefore, they are excluded from the analyses that follow. Box and whisker plots using the new set of data are shown in Figure 4.8.

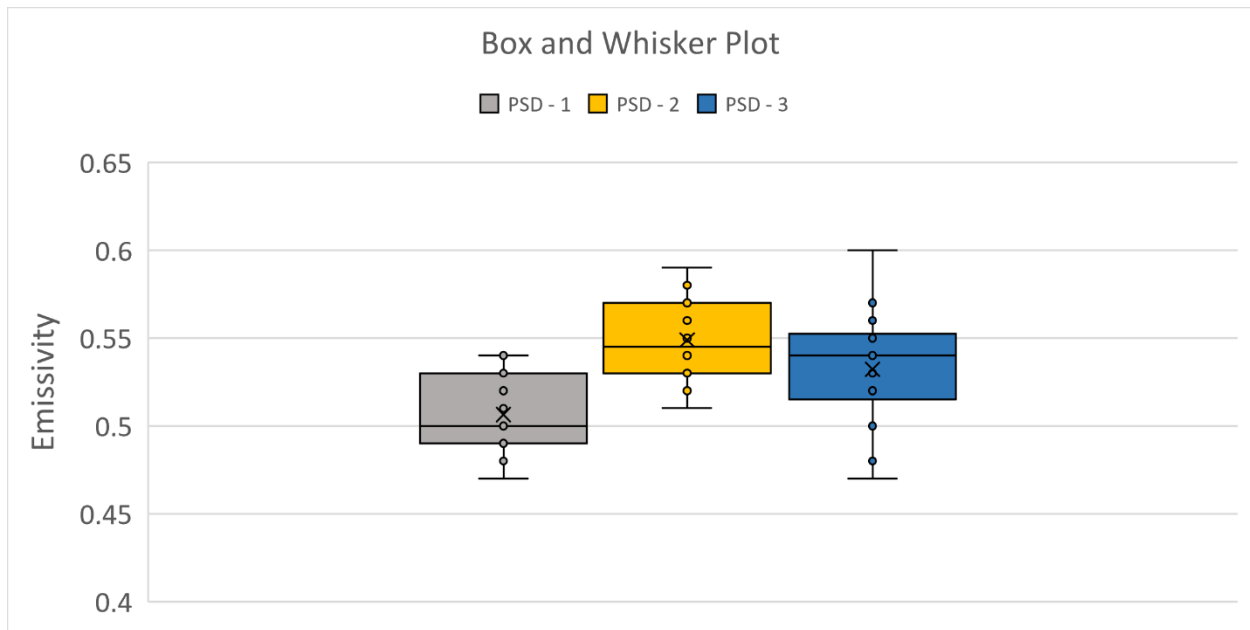


Figure 4.8 Box and whisker plots excluding outliers

Furthermore, given that there is no previous data to refer to regarding the emissivity of powder, statistical significance of the measured emissivity values was determined via hypothesis testing. Specifically, a linear regression test between particle size and emissivity was performed as the relationship between emissivity and surface roughness is understood. PSD – 1 could be thought of as a less rough surface compared to PSD – 2 and PSD – 3 as it has particle sizes between 15 μm and 53 μm while PSD – 2 and PSD – 3 powders have particle size ranges from 45 μm to 106 μm and 45 μm to 150 μm respectively. The size of particles from PSD – 2 and PSD – 3 would create deeper cavities than those of PSD – 1. The greater range of sizes leads to increased packing of the PSD – 2 and PSD – 3 powders since there are relatively smaller particles to fill in the gaps between the >100 μm particles unlike the PSD – 1 powder that only ranges between 15 μm and 53 μm . Microscope images of the surface of the powder samples were taken using a Keyence VHX 7000 (Keyence, IL, USA) while following the tap density sample preparation method described in section 3.6.1. The Keyence VHX 7000 provides an option for a depth

analysis, a qualitative image taken to highlight changes in surface height by first focusing on a lower limit and imaging the surface to the upper focused limit. These images are shown in Figures 4.9 – 4.14.

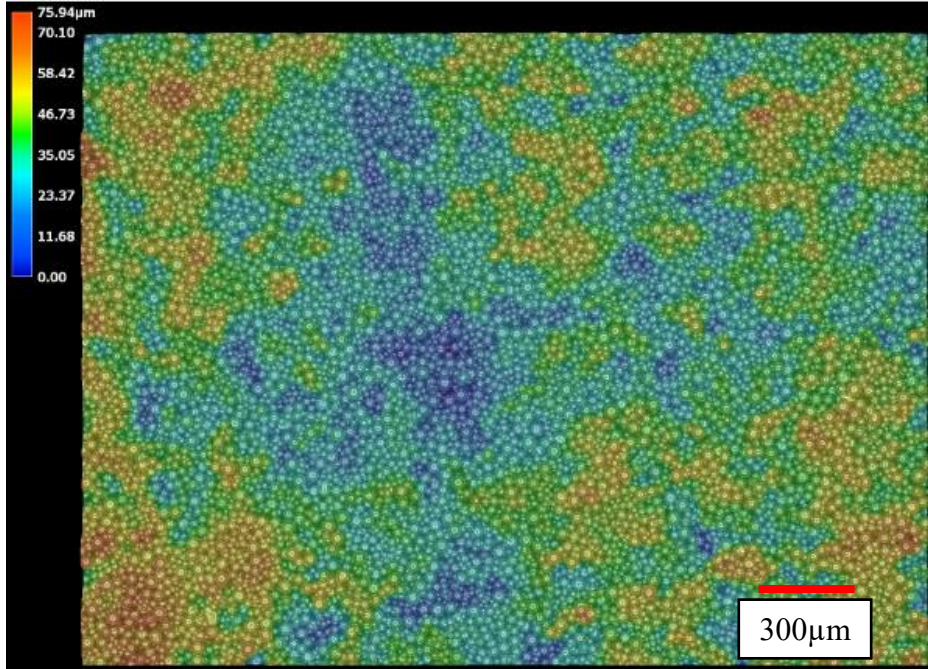


Figure 4.9 Depth analysis image of PSD - 1 tap density surface at 150x

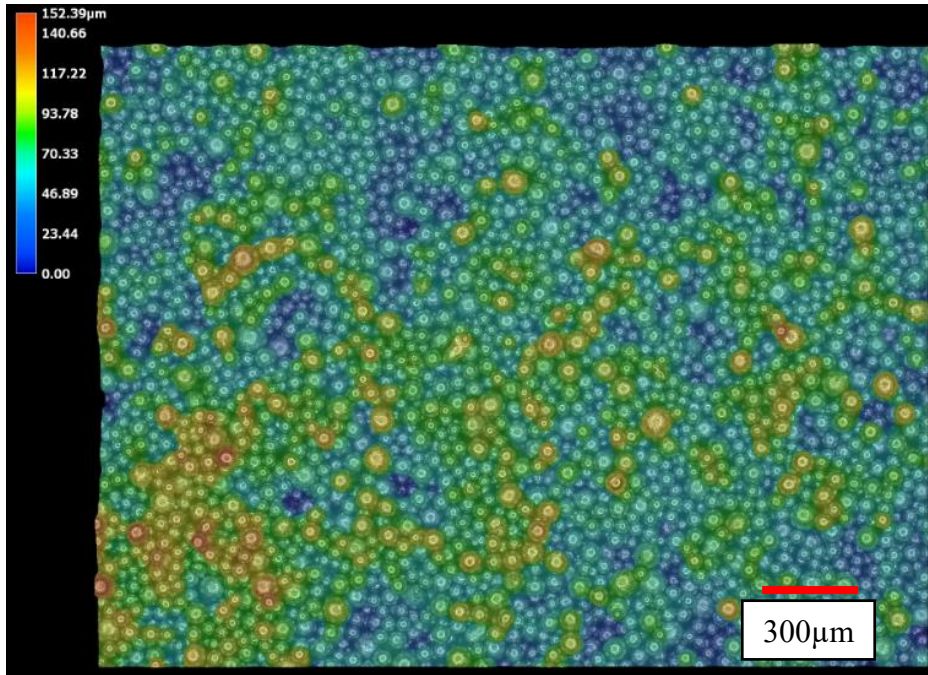


Figure 4.10 Depth analysis image of PSD - 2 tap density surface at 150x

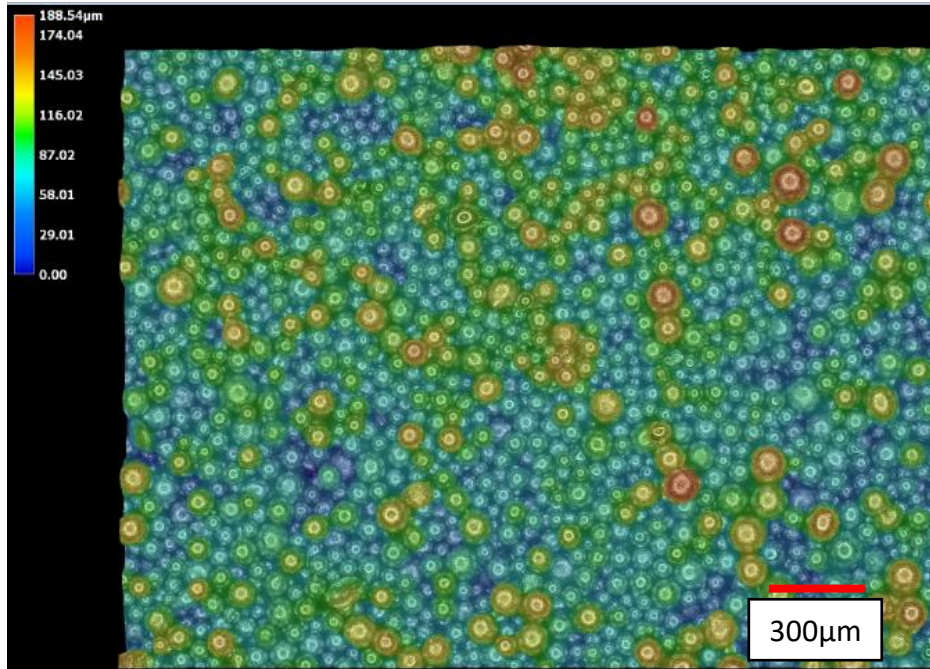


Figure 4.11 Depth analysis image of PSD - 3 tap density surface at 150x

The scale bar included with the image shows both the range and max height reached for the upper focusing limit. The images show that the maximum height for PSD – 1 was about 80 μm shorter than PSD – 2. Similarly, the color gradient in the PSD – 1 image (Figure 4.6) indicates an even surface as opposed to PSD – 2 or PSD – 3, where the same gradient is not visible. Next, the same images were taken of the apparent density sample preparation surface to acknowledge any differences that may be correlated in the results.

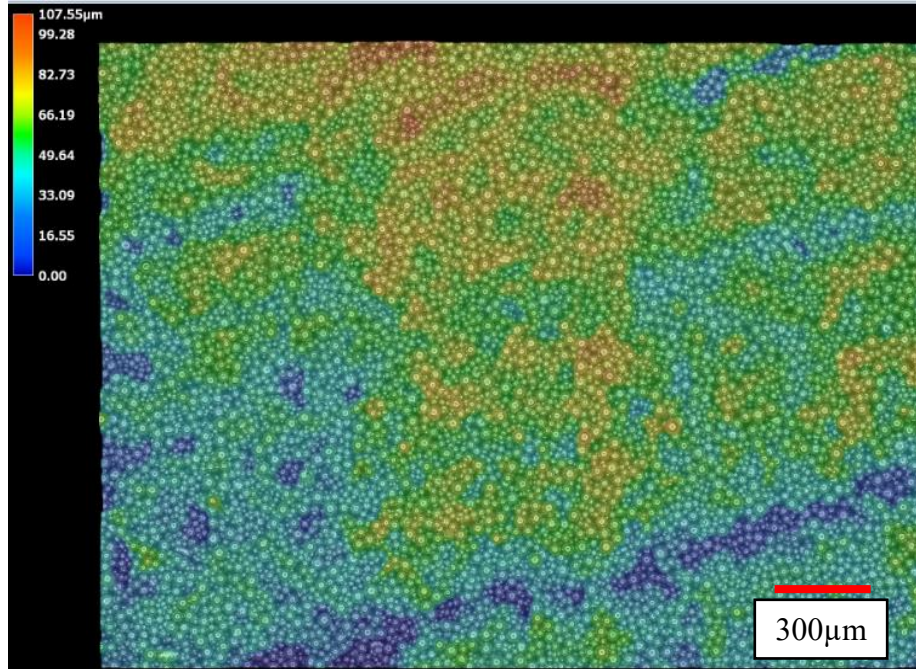


Figure 4.12 Depth analysis image of PSD - 1 apparent density surface at 150x

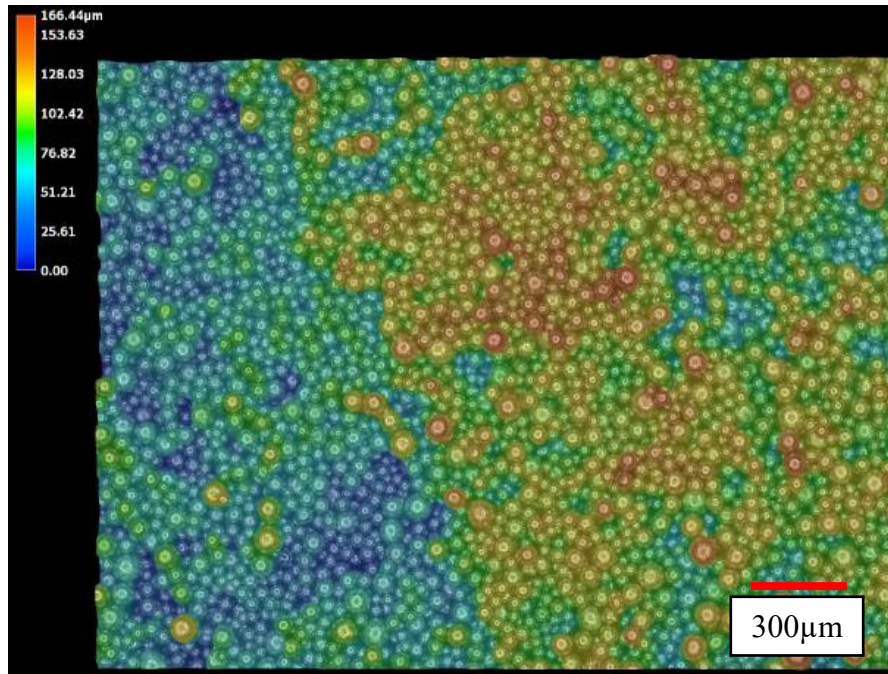


Figure 4.13 Depth analysis image of PSD - 2 apparent density surface at 150x

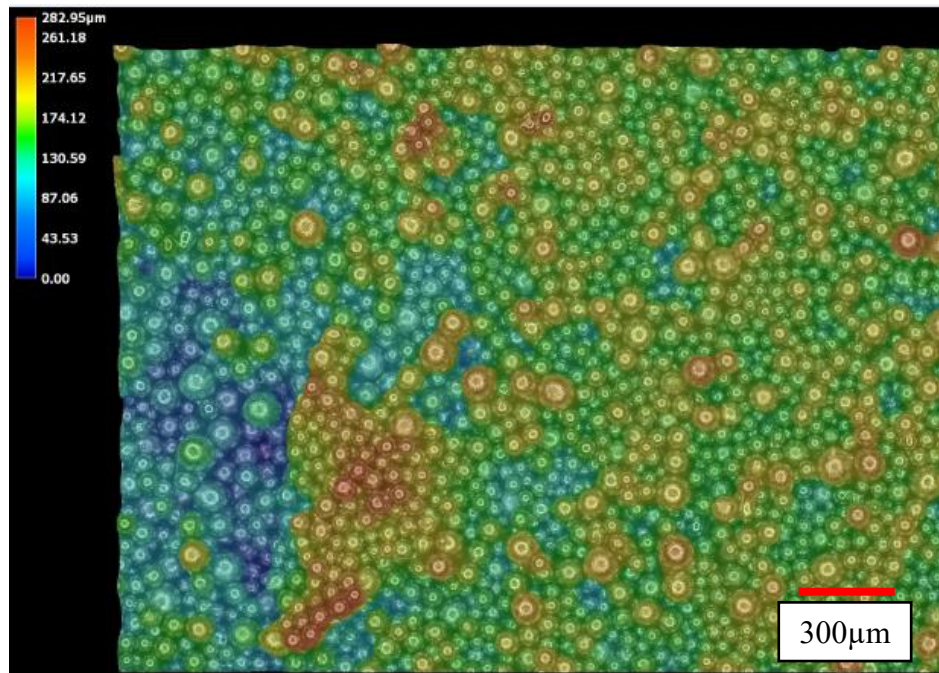


Figure 4.14 Depth analysis image of PSD - 3 apparent density surface at 150x

TPRC data for Inconel's spectral emittance is available for various surface finishes (sandblasted, electropolished, etc.) and contains the wavelengths at which they were measured. The

“electropolished” surface finish has a reported emissivity of about 0.2 – 0.3 between 755K and 922K at about 2000nm, while the “sandblasted” surface has a reported emissivity of 0.35 – 0.4 under the same conditions. A similar correlation between surface roughness and emissivity can be made for the values captured in the experiments, utilizing a linear regression test to confirm whether the values obtained correlate with the understood relationship between surface roughness and emissivity.

For the linear regression test, the hypotheses can be summarized as follows: The null hypothesis states that there is no significant relationship between the independent variable (powder size) and the dependent variable (emissivity). The alternative hypothesis states that there is a significant relationship between the independent variables and the dependent variable. D50 values of 40 μm , 73 μm , and 85 μm were used to designate the values for the independent variables to create a more representative scale in relation to the emissivity values since PSD – 2 and PSD – 3 d50 values are only 12 μm apart while PSD – 1 and PSD – 2 d50 values differ by 33 μm . A plot of the emissivity values with increasing particle size is shown in Figure 4.15 with a trendline to illustrate the relationship.

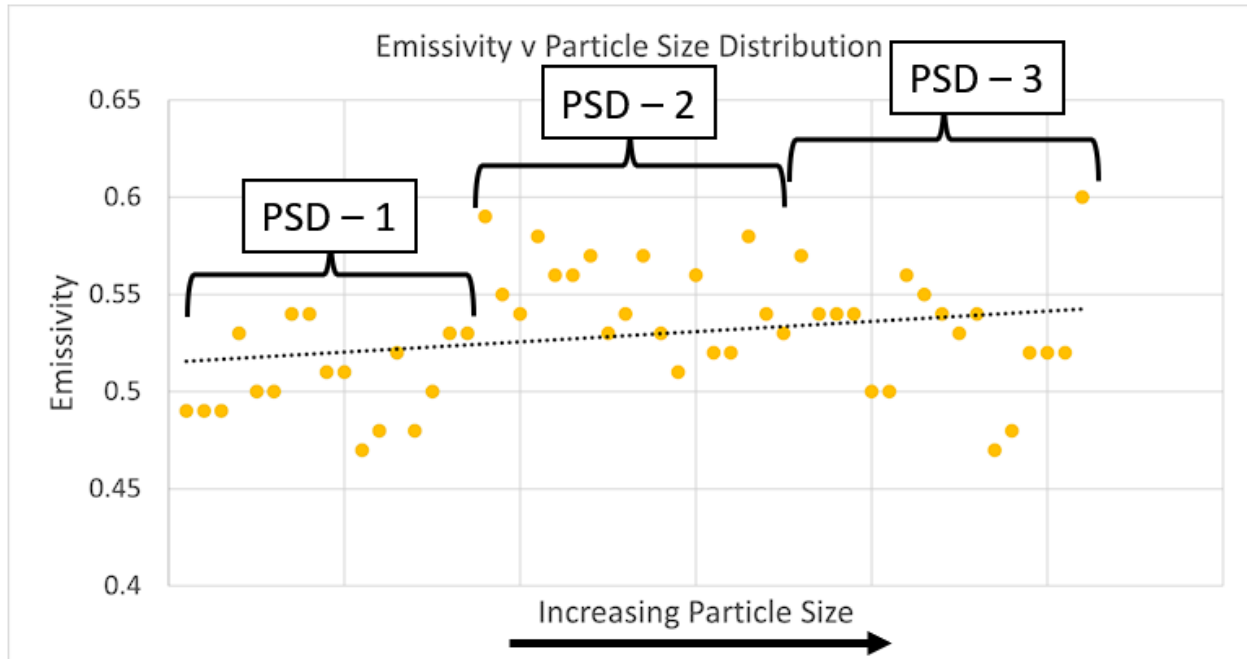


Figure 4.15 Plot of emissivity vs PSD

Although an adjusted r-squared value of 0.17 was calculated using R-Studio, the r-squared value increases with more predicting factors being added to the test. Despite this, a p-value of 0.0015 was calculated from the same linear regression test indicating there is significant evidence to suggest there is a relationship between particle size and emissivity.

4.6.1 Analysis of Means and Variance Between Experiment Runs

Before performing an analysis of variance, a test for equal variance must be conducted to choose the appropriate test. Using Bartlett's test for equal variances, the null hypothesis states that the variances are equal while the alternative hypothesis states at least one of the variances is not equal. A p-value of 0.356 was calculated using R-studio, meaning that with ~36% confidence the null hypothesis cannot be rejected. In keeping with this, both a one-way ANOVA and Welch's ANOVA were performed, assuming equal and non-equal variances respectively, to test the hypothesis regarding whether the runs (treatments) had an impact on the emissivity values (means of runs). Using R-studio, a p-value of 0.09 was calculated for the one-way ANOVA and

0.06 for Welch's ANOVA and thus not enough evidence exists to suggest the treatments had a significant impact on the means regardless of equal or non-equal variances. Furthermore, Tukey's honestly significant difference (HSD) test was conducted to identify what means, if any, were significantly different. In this analysis, the null hypothesis is that there is no significant difference between the specified populations. The alternative hypothesis states at least one population is significantly different. The results of Tukey's HSD test were calculated and plotted in R-studio and the results are presented in Table 4.10.

Table 4.10 Results of Tukey's HSD test calculated in R-studio

	P - adj
2 - 1	0.273
3 - 1	0.717
3 - 2	0.717

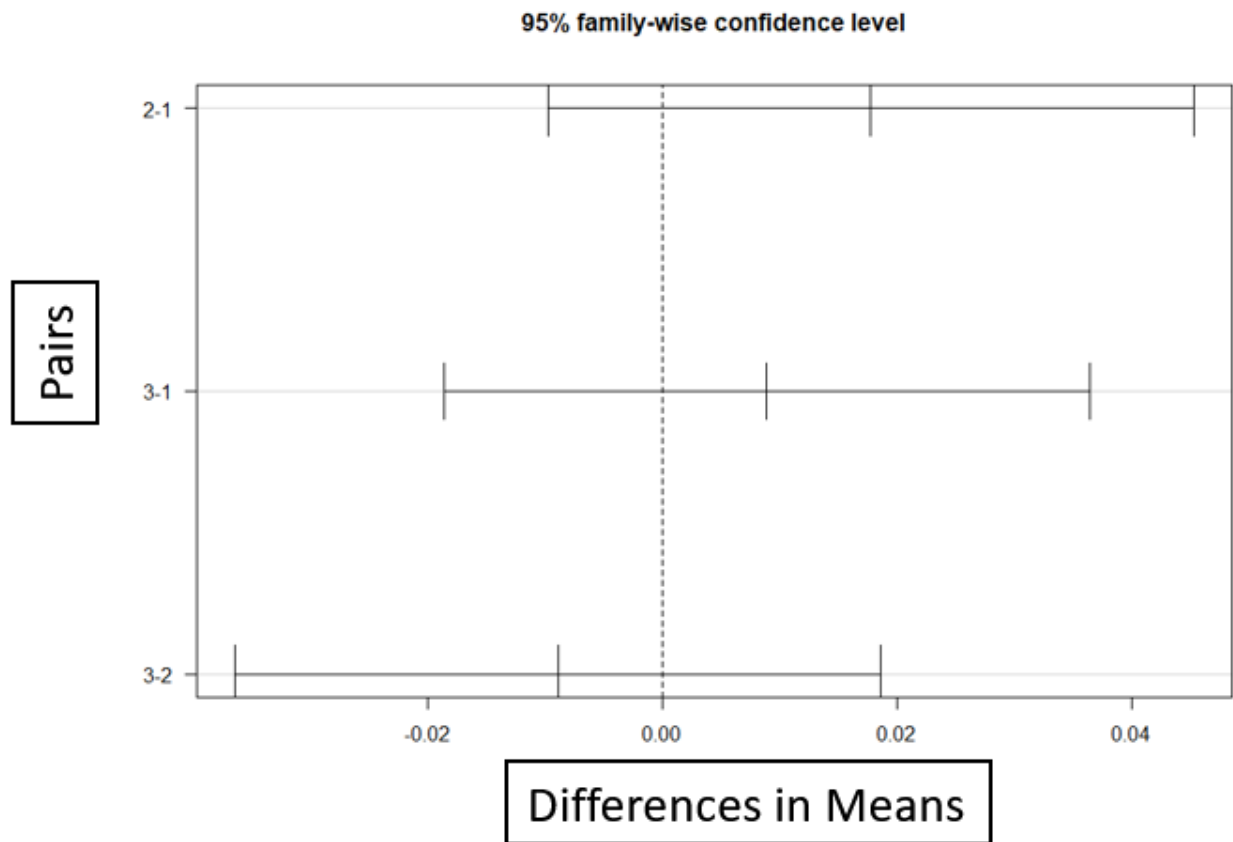


Figure 4.16 Plot of Tukey's HSD test results for run comparison

The test results show that the null hypothesis cannot be rejected with a 27%, 72%, and 72% level of significance for runs 2-1, 3-1, and 3-2, respectively. The results indicate the means are not

significantly different, meaning it is likely the means of the runs are not a product of chance and more measurements would likely be similar to those already captured.

4.6.2 Analysis of Means and Variance with Temperature

Emissivity's variance with temperature has been shown in the TPRC for solid metals. Like the pairwise comparison calculated in the previous section, another comparison to see if there is a statistically significant effect from temperature on the emissivity values captured from the experiments. The null hypothesis remains that the temperature does not have a significant effect on the emissivity values captured. The alternative hypothesis states that temperature does have a significant impact on the emissivity values captured. The results of Tukey's HSD test calculated and plotted in R-studio are shown in Table 4.11 and Figure 4.17.

Table 4.11 Results of Tukey HSD test calculated in R-studio

	P - adj
500°C – 400°C	0.070
600°C – 400°C	0.056
600°C – 500°C	0.994

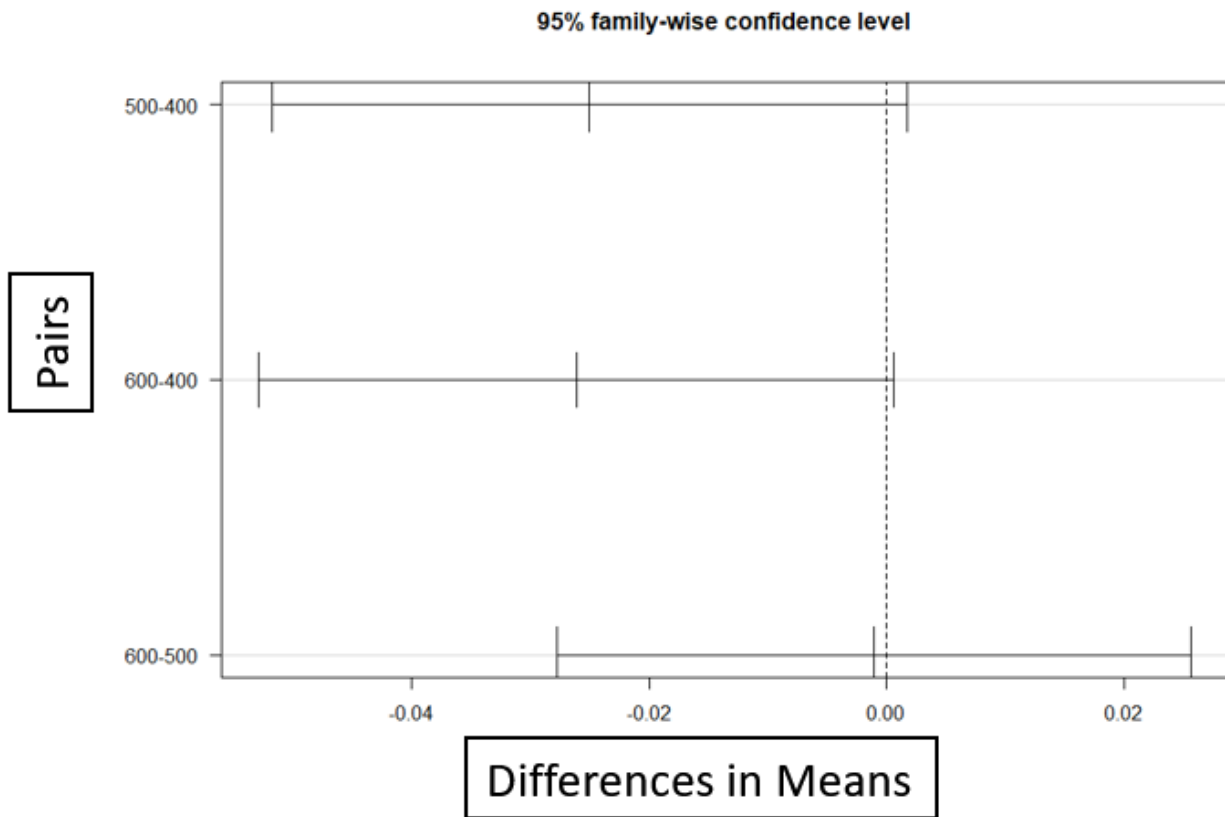


Figure 4.17 Plot of Tukey's HSD test results for temperature comparison

The results indicate that the null hypothesis for any of the pairs cannot be rejected and the 500-600 pair is even nearly identical (~99% the same) and so the null hypothesis that there is no

statistically significant difference cannot be rejected. To illustrate the means and standard deviations, a confidence interval plot is shown in Figure 4.18.

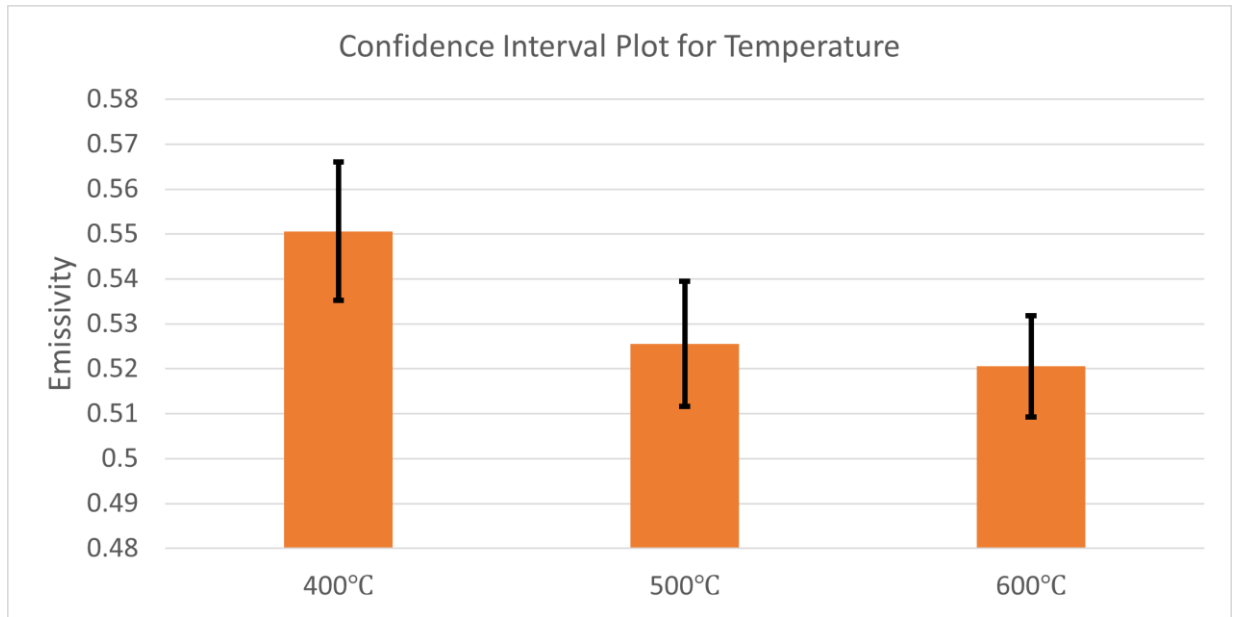


Figure 4.18 Confidence interval plot for emissivity at each temperature

The plot illustrates the difference in means detected by Tukey's HSD test, where a difference of ~ 0.03 can be seen in the means of 400°C and 500°C. A thermal analysis of the crucible and powder with an applied heat of 500°C placed on the bottom surface of the crucible to simulate heat from the filament was performed in Fusion 360 to illustrate thermal gradients within the crucible using the thermal conductivity of Inconel 718 powder ($\sim 11 W/m \cdot K$) as the material within the crucible and $\sim 300 W/m \cdot K$ for the thermal conductivity of the crucible.

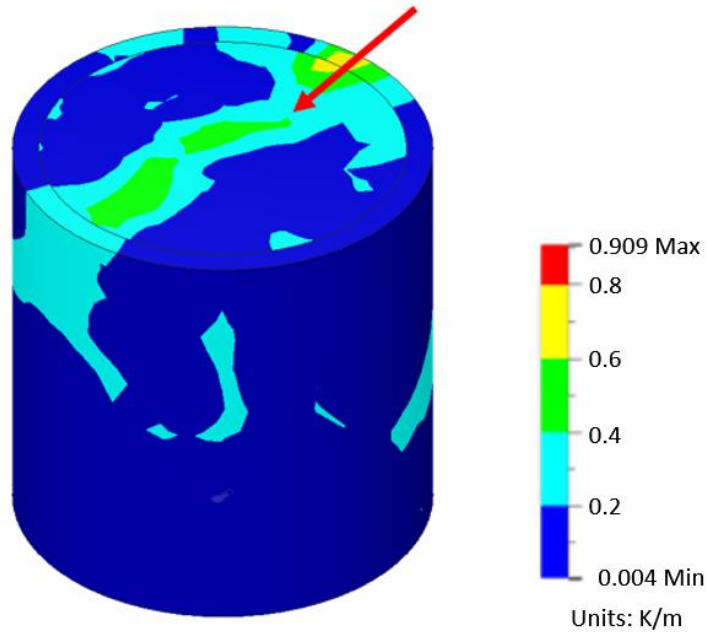


Figure 4.19 Thermal analysis w/ thermal gradient legend

It is expected that the decrease in emissivity from 400 to 500 is due to the thermal gradients produced from the thermal conductivity of the AlN crucible. The relationship between the decrease in thermal conductivity and temperature can be expressed as $T^{-1.25}$ indicating that most of the decrease in thermal conductivity occurs at temperatures between 27°C and 180°C where a more than 50% reduction in thermal conductivity from $\sim 300 \text{ W/m} \cdot \text{K}$ at 27°C to $\sim 130 \text{ W/m} \cdot \text{K}$ at 180°C (Slack et al., 1987). To confirm the existence of a thermal gradient within the crucible, temperature measurements with the FMPI were taken at locations deemed the “upper/lower” and “sides,” where the sides are closest to the filament/lead connections, when the center temperature was measured at $\sim 600^\circ\text{C}$. The “sides” are areas on the powder surface closer to the lead connections for reference. An illustration of the measurement locations is shown in Figure 4.20 and the average temperature recorded is shown in Table 4.12.

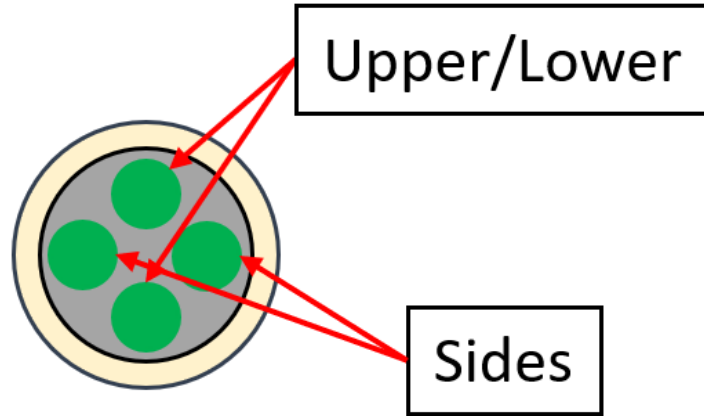


Figure 4.20 Measurement locations on sample surface

Table 4.12 Average temperatures of locations

Center	Upper	Lower	Side	Side
598°C	584°C	564°C	618°C	614°C

The temperature measurements indicate there is a thermal gradient present within the surface of the powder. However, the pyrometer gives a tolerance that represents the gradient within the measurement area ($\text{Ø}2.7\text{mm}$) and for all measurements taken the tolerance was $<3^\circ\text{C}$ meaning that although there is a gradient present on the entire surface of the powder, the measurement area does not reflect the same gradient. Rather, the existence of the thermal gradient on the surface suggests that emissivity measurements at 500°C and 600°C are 0.03 lower than 400°C due to the powder being compacted at the center from the thermal expansion of powder at the outer regions of the crucible. To confirm/deny a linear correlation between 400°C and $500^\circ\text{C}/600^\circ\text{C}$ so that the values at higher temperatures are still capable of producing accurate emissivity values with this understanding a linear regression test was performed using R-studio.

A p-value of 0.033 was calculated, leading to rejecting the null hypothesis that there is no linear relation between 400°C and 500°C measurements and accepting the alternative hypothesis with a significant amount of evidence suggesting there is likely a relationship between the two.

Furthermore, the means of the 600°C measurements are 0.005 less than those of the 500°C measurements and it is expected this decrease in emissivity, like the relationship between temperature and thermal conductivity, will be <0.005 at higher temperatures. This coupled with the statistical analysis of the 500°C and 600°C measurements suggests that higher temperatures measurements are still viable and will produce similar emissivity values that can be correlated to 400°C values while accounting for a 0.03 difference in emissivity.

4.6.3 Analysis of Means and Variance with Powder Size Distribution

An analysis of the means and variance between powder size distributions was conducted to reduce the expense and time of experiments via a pairwise comparison to check for particle size distributions that could be excluded in future experiments. Initially, PSD – 2 and PSD – 3 appeared to be similar considering their particle size distributions both start at 45 μm and d50 values are within 12 μm of each other which may not be an accurate separate metric for operators to compare to. A hypothesis test for the null and alternative was conducted for the particle size distributions and the results of Tukey’s HSD test are shown in Table 4.13 and Figure 4.21.

Table 4.13 Tukey's HSD test results using R-studio

	P - adj
2 – 1	0.000
3 – 1	0.026
3 – 2	0.108

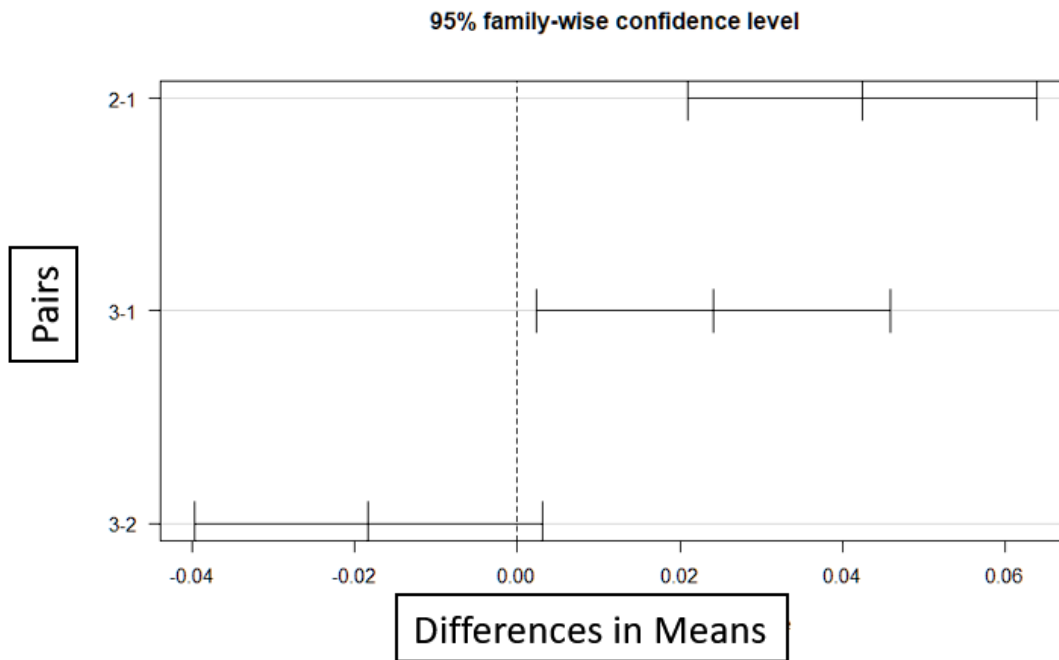


Figure 4.21 Plot of Tukey's HSD test for particle size distribution

The results indicate that there is not enough evidence to reject the null hypothesis for PSD – 2 and PSD – 3 with a p-value of 0.108, implying they are not statistically different. For the PSD – 1 and PSD – 2/PSD – 3 pairs, however, the null hypothesis was rejected in favor of the alternative which states there is a statistical difference between the measurements of these pairs.

4.6.4 Analysis of Means and Variance with Sample Preparation Methods

To account for potential errors within sample preparation methods, a Bartlett test of homogeneity of variances to test whether the variances between sample preparation methods are different was done. The results of the Bartlett test conducted in R-studio are shown in Table 4.14.

Table 4.14 Results of Bartlett test

```
bartlett test of homogeneity of variances
data: Emissivity by Prep
Bartlett's K-squared = 0.88047, df = 2, p-value = 0.6439
```

The p-value of 0.644 suggests the null hypothesis that the variances are statistically the same cannot be rejected, meaning there is no statistically significant difference between the variances of the tap density sample preparation method and that of the apparent density sample preparation method. Although no significant difference in the variances was found for a single operator, it is important to note that for the “Separate Operator Run” the standard deviations between tap and apparent density were different by 0.1, with the apparent density having a standard deviation of 0.14 and tap density of 0.04. The intent of this specific run was to check for potential human error from the operator and it is likely that the apparent density sample preparation method lends itself to greater variation due to the lack of compaction prior to scraping across the surface and experience with the sample preparation method. Furthermore, a t.test was performed to compare the means of the tap and apparent density sample preparation results to confirm if they are the same. The p-value and calculated means are shown in Table 4.15.

Table 4.15 T.test results comparing sample preparation methods

Means	
Tap Density	Apparent Density
0.54	0.52
t.test P-value: 0.043	

The results indicate there is enough evidence to reject the null hypothesis in favor of the alternative which states that there is a statistically significant difference between the two means. It was expected that the apparent density sample preparation method would result in a higher emissivity in that the channels that may be produced within the surface would create a sort of cavity on the surface, like a blackbody cavity and to a lesser extent. Although the means differ by 0.02 the t.test results indicate they are different, and the tap density is the greater of the two.

Surface roughness can be defined as a complicated shape with continuous peaks and valleys whose height, depth, and intervals differ while waviness refers to uneven surface features appearing at longer intervals than the roughness (*VHX-7000 User's Manual 1 Before Using the VHX-7000*, n.d.). An illustration of these differences is shown in Figure 4.22.

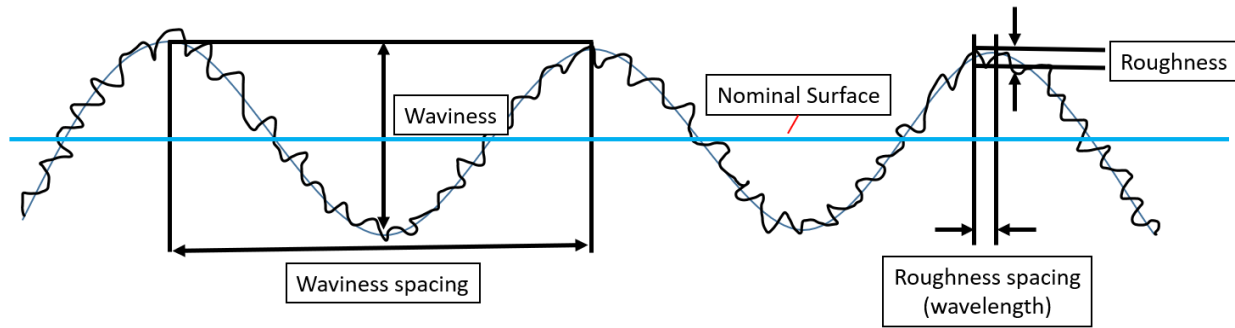


Figure 4.22 Illustration of waviness and surface roughness

It is expected that the channels within the apparent density sample surface are akin to a waviness and do not directly impact the surface roughness, whose relationship with emissivity is known to increase with an increase in surface roughness. Similarly, the ten point average surface roughness, R_z , is calculated using the sum of the peak and valley heights divided by the sample length (*Technical Reference - Surface Roughness - IAI America, n.d.*). It is from this relationship between the abundance of peaks and valleys and the calculated average surface roughness that the compaction of the powder (i.e., tap density preparation) is expected to lead to a greater amount of both peaks and valleys as opposed to the apparent density preparation method in which the powder is loosely spread.

Although other alloys are not explored in this research, the intent was to reduce sources of variation to translate the method to other metal powders. It was noticed at times during the sample preparation procedure that if the straight edge was not one continuous motion, noticeable depressions in the powder were sometimes created and so the preparation had to be performed again. An example of these depressions can be seen in the depth analysis image of PSD – 1’s apparent density sample preparation surface (Figure 4.23).

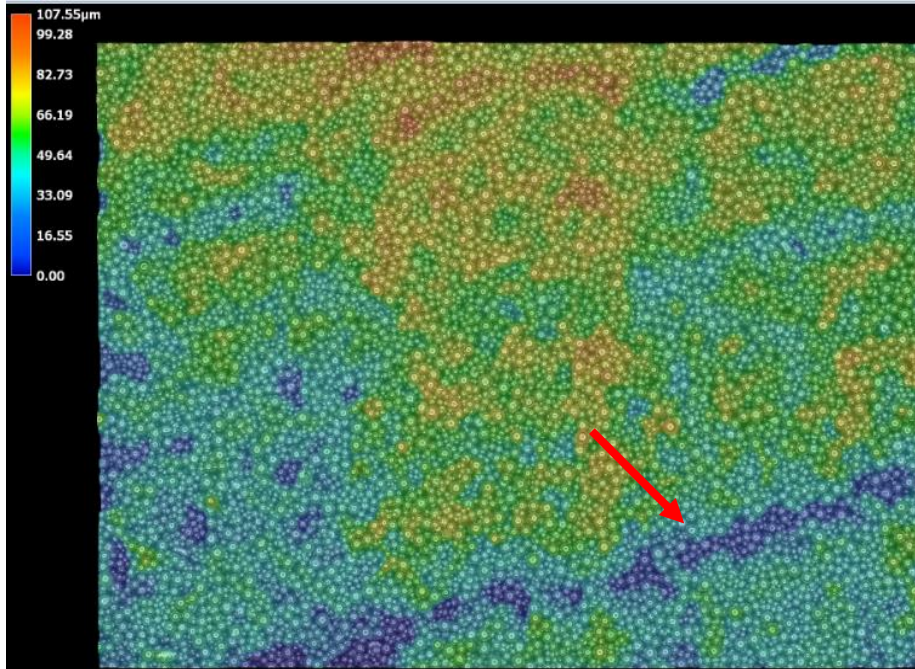


Figure 4.23 PSD - 1 apparent density depth analysis image highlighting artificial cavity

While it is unlikely that the sample preparation method would result in a difference in the variability for a trained operator, a consideration was made to solely utilize tap density for future operators as there was no variation like that of the apparent density from the “Separate Operator Run” of experiments. Additionally, the original operator carried out the apparent density sample preparation method a total of 18 times compared to the other operator that performed it only 3.

4.6.5 Emissivity Dependence with Wavelength

Emissivity is known to vary with wavelength, plots of the .DAT files containing the spectral emissivity of PSD – 1 at each temperature, sample preparation method, and 1-minute into the data acquisition for each temperature between the wavelengths of 1080nm and 1640nm are plotted in Excel and shown in Figure 4.24 – 4.26.

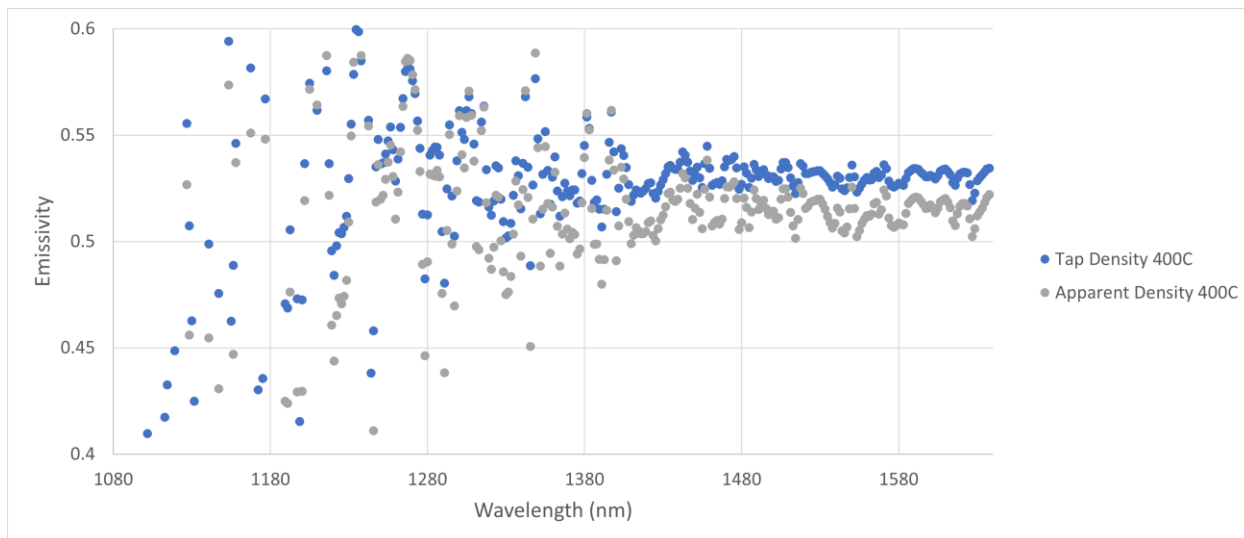


Figure 4.24 .DAT file plotted for PSD - 1 at 400°C, for each sample preparation and 1 minute into data acquisition

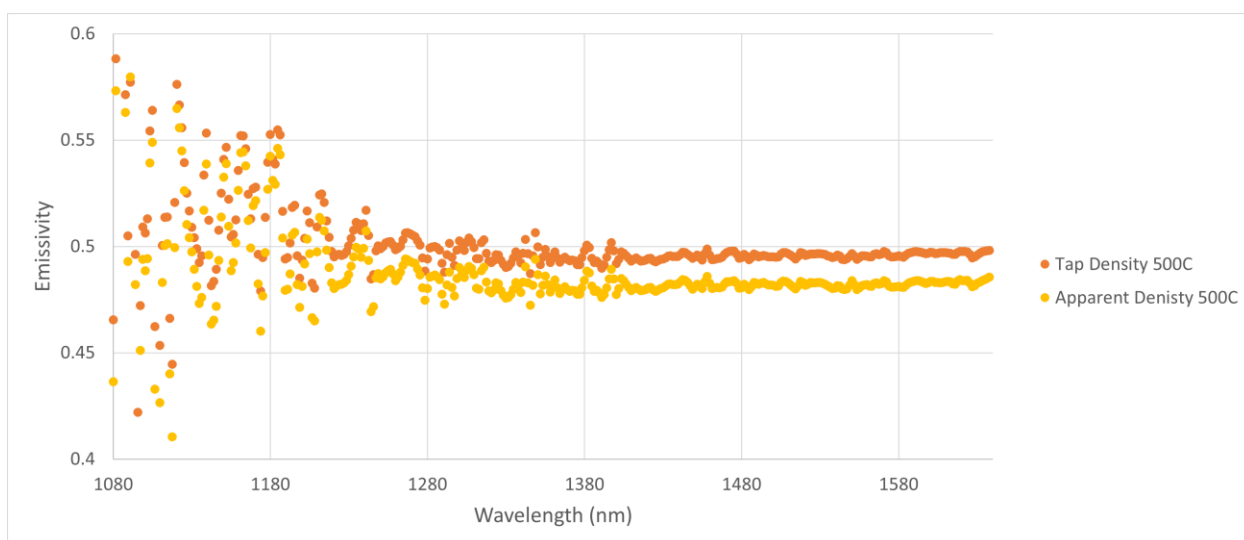


Figure 4.25 .DAT file plotted for PSD - 1 at 500°C, for each sample preparation and 1 minute into data acquisition

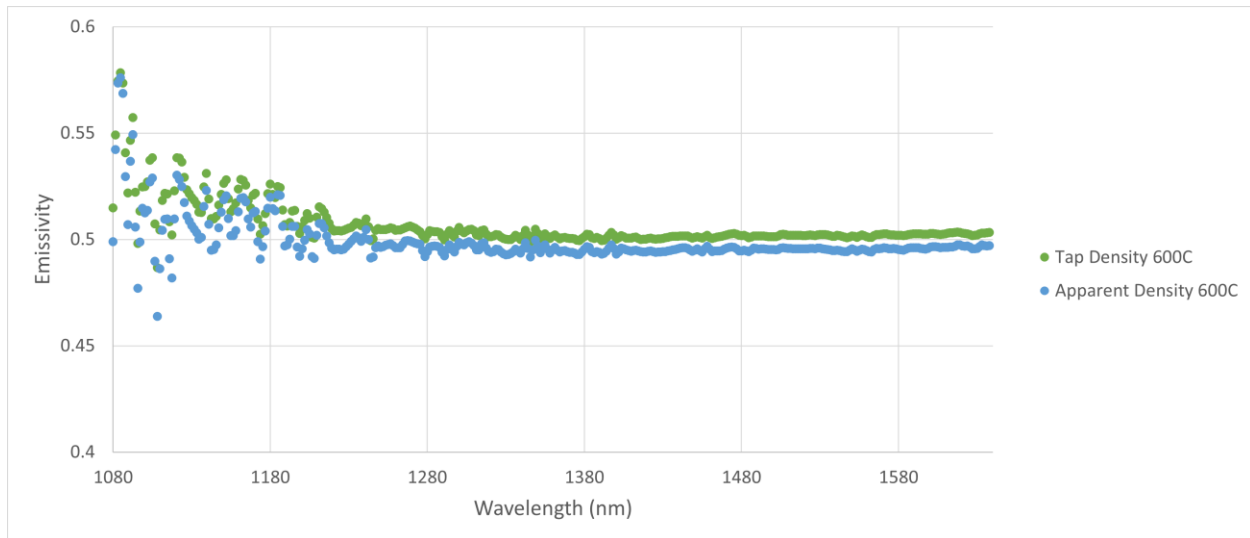


Figure 4.26 .DAT file plotted for PSD - 1 at 600°C, for each sample preparation and 1 minute into data acquisition

At higher temperatures, the deviation of emissivity across the calibrated spectrum (1080nm – 1640nm) gets reduced from 0.173 at 400°C to 0.011 at 600°C. It is important to note that the intensity peak, for a blackbody, of the emitted spectrum shifts to shorter wavelengths as temperature increases (Britannica, 2020). This shift in intensity peak implies that noise captured by the pyrometer would be influential to the measurements at lower temperatures and shorter wavelengths. This is why a trend is seen as the temperature increases that the standard deviation of the spectral emissivity decreases. This does not invalidate the values captured that are used for the statistical analysis at 400°C since the pyrometer can exclude noise from its emissivity calculations and the emissivity at 1500nm was used for the analysis, deemed the “central wavelength” by the manufacturer.

4.6.6 Normality and Analysis of Variance and Means to Include Different Operators

The results that were presented thus far in the section were the basis for experiments to include other operators. The inclusion of the separate operators is to gage reproducibility for the method described in this research and to identify potential sources of variation, if any, that can

impact the application between different alloys and operators. The significant findings in the statistical analysis can be summarized in 5 points:

1. PSD – 2 and PSD – 3 have statistically similar measurements.
2. PSD – 1 and PSD – 3 encompass a predictable trend of emissivity values.
3. Measurements at 500°C and 600°C are statistically similar and can be related to 400°C.
4. Emissivity values captured utilizing the experiment methodology are not statistically different between runs for a single trained operator.
5. The emissivity of Inconel 718 powder behaves as a graybody (e.g., independent of temperature and wavelength) between the wavelengths of 1080nm and 1640nm and temperatures of 400°C to 600°C.

Considerations from the results of previous sections resulted in using PSD – 1 and PSD – 3 for measurements as the emissive behavior trends were understood, temperature measurements at 450°C and 600°C as 500°C was statistically similar to 600°C while still encompassing a range, and 3 total runs as that was the amount performed by the original operator. The operators were trained by being present while the original operator conducted an experiment including calibration, sample preparation, and ultimately capturing measurements after being described the methodology and afterwards left to conduct the experiments independently. The PSD – 1 powder was difficult to heat even after 60 minutes of heating at the maximum current output of the power supply (60 amps) so the final temperatures reached for each operator and each run is shown in Table 4.16.

Table 4.16 Max temperatures reached during data acquisition for PSD - 1 experiment runs

Runs	Operator 1	Operator 2	Operator 3
1	553°C	548°C	561°C
2	559°C	564°C	580°C
3	553°C	564°C	567°C

Although the sample surface temperature did not reach 600°C, the results are still expected to be valid as it was found that the emissivity values between 500°C and 600°C were not significantly different statistically. The results from the 3 runs of experiments are shown in Table 4.17.

Table 4.17 Results of emissivity values measured from different operators

Operator 1				
Runs	PSD - 1 (450°C)	PSD - 1 (600°C)	PSD - 3 (450°C)	PSD - 3 (600°C)
1	0.512	0.507	0.517	0.535
2	0.516	0.530	0.518	0.525
3	0.512	0.507	0.529	0.530

Operator 2				
Runs	PSD - 1 (450°C)	PSD - 1 (600°C)	PSD - 3 (450°C)	PSD - 3 (600°C)
1	0.520	0.538	0.534	0.535
2	0.513	0.504	0.495	0.52
3	0.471	0.515	0.548	0.539

Operator 3				
Runs	PSD - 1 (400°C)	PSD - 1 (600°C)	PSD - 3 (450°C)	PSD - 3 (600°C)
1	0.546	0.484	0.513	0.535
2	0.475	0.513	0.526	0.527
3	0.525	0.535	0.552	0.54

The results were kept to the third decimal point so the normality test to follow could be more representative of the data, then they were put into a probability plot using MiniTab and the results are shown in Figure 4.27.

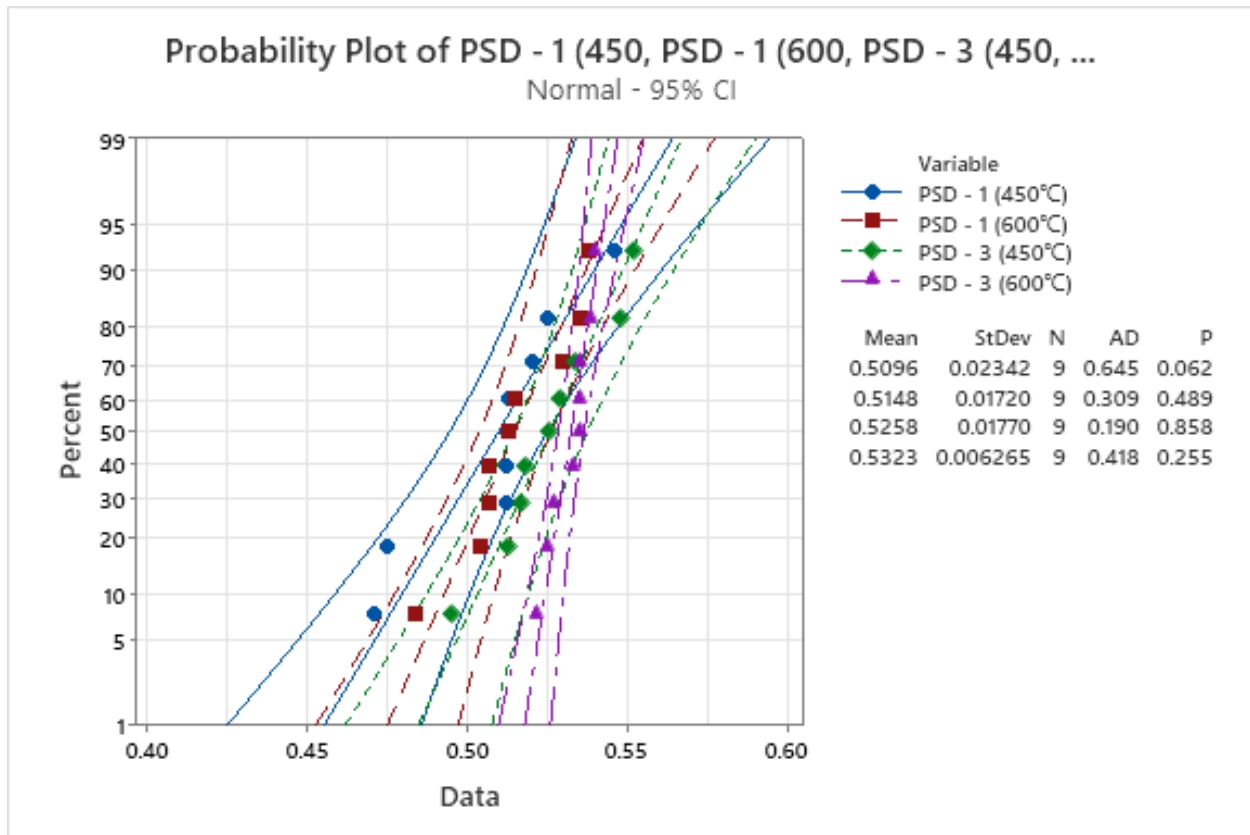


Figure 4.27 Results of Probability Plot

A normality plot was chosen as the requirements for a Gage R & R were not met in measuring the same “part,” as the parts (sample surfaces) had inherent variations within them. Despite this, the normality plot and p-values suggest the measurements from each of the particle distributions and temperatures meet normality requirements. Data that possess normality allow for other types of statistical analyses and are preferred as they are ever-present in nature. Furthermore, an analysis of variance and means was performed in MiniTab and the results are shown in Figure 4.28 and 4.29, respectively. the mean for PSD – 1 was ~0.51 and for PSD – 3 was ~0.53. To further illustrate the study, illustrations plotted from R-studio are shown in Figure 4.28.

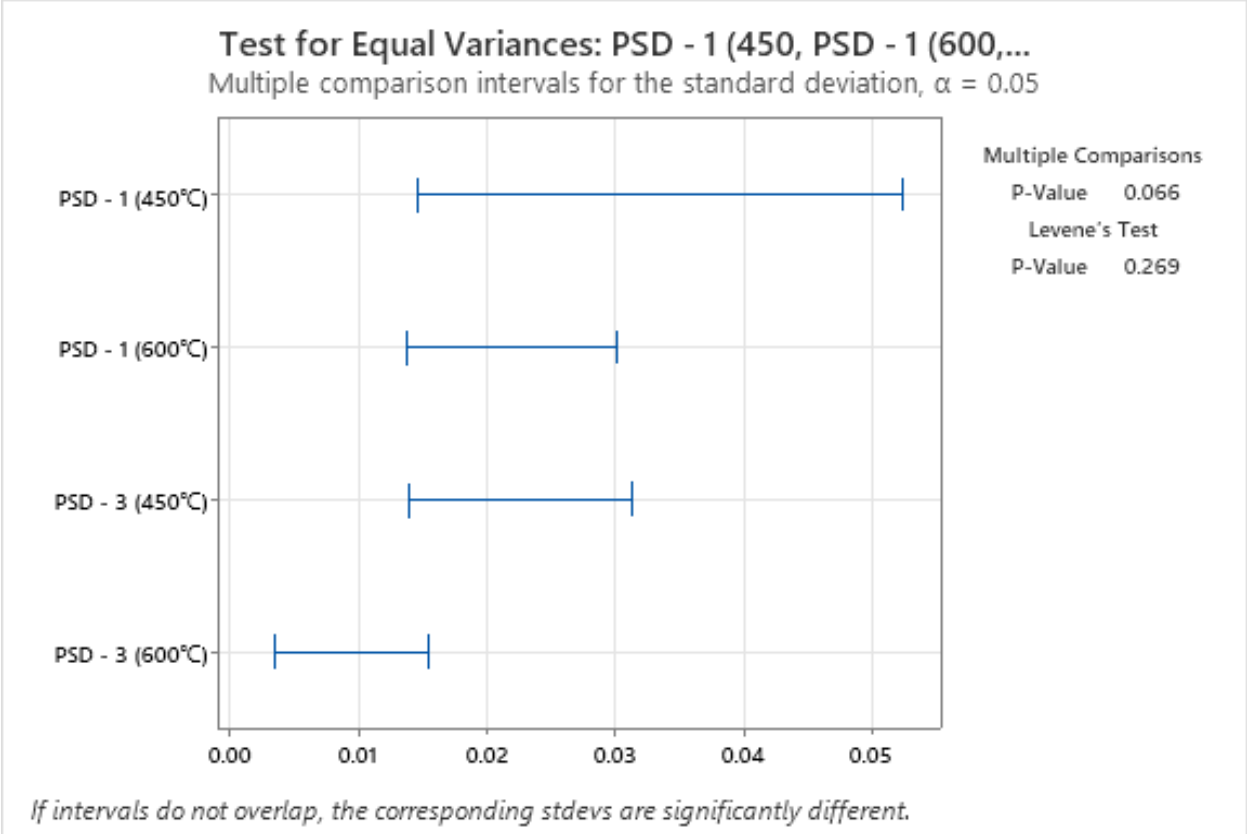


Figure 4.28 Results of Analysis of Variance

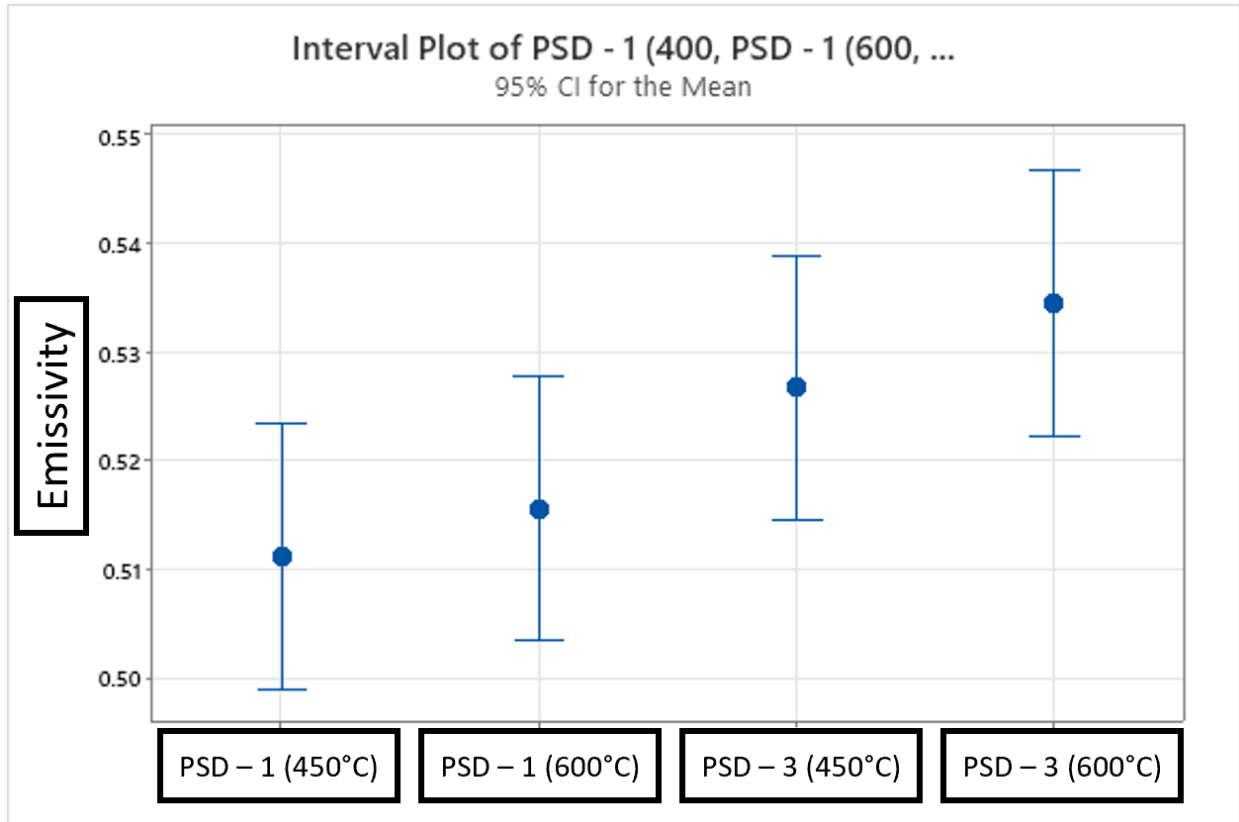


Figure 4.29 Interval Plot for Analysis of Means

The p-value calculated from the One-Way ANOVA was 0.036, suggesting that not all means are equal. To identify the different means, a two-sample t-test was performed and the results are shown in Table 4.18.

Table 4.18 Results of two-sample t-test

	P - adj
PSD - 1 (450°C) - PSD - 1 (600°C)	0.598
PSD - 3 (600°C) - PSD - 1 (450°C)	0.201
PSD - 3 (450°C) - PSD - 3 (600°C)	0.322
PSD - 3 (600°C) - PSD - 1 (450°C)	0.020

The results indicate that the difference is between PSD – 3 at 600°C and PSD – 1 at 450°C, similar to previous sections in which PSD – 1 and PSD – 3 had statistically different means. Although the results for the PSD – 3 at 600°C and PSD – 1 at 450°C were not found to be statistically different, it is important to note the highest variation was for PSD – 1 at 450°C and it is expected this is contributing to the results as it was also the lowest p-value after the PSD – 3 at 600°C and PSD – 1 at 450°C comparison. The evidence described in this and previous sections suggests that the use of this methodology can be used successfully to understand a material's spectral emissive behavior. Conclusions and recommendations for the method including use of the information for successful integration of IR cameras in AM processes and improving the integration of these measurements into the industry are given in Chapter 6.

CHAPTER 5: INTEGRATION OF A MULTI-WAVELENGTH PYROMETER AND L-PBF MACHINE

This chapter describes the integration and use of a MW pyrometer with a laser powder bed fusion system, with the goal of capturing thermal signatures throughout the L-PBF process. Utilizing an Aconity MIDI+ (Aconity 3D, GmbH) and an FMPI SpectroPyrometer (FAR Associates, OH, USA), the integration of these two technologies yields great merit in the realm of in-situ process monitoring. The main objectives are captured in the following statements:

1. Design and fabricate a fixture to mount the multi-wavelength pyrometer optic to the scan head to capture data on a plane.
2. Development of a calibration technique for the pyrometer and its intended application.
3. Demonstrate in-situ monitoring capabilities.

An Aconity MIDI+ was employed for its open architecture and ability to integrate a tertiary scan head that would act as the mounting point for the pyrometer. This allows for both coincidental monitoring of the laser/material interaction and off-axis monitoring of areas of interest on the build plate. The FMPI previously described was used for its ability to obtain emissivity-independent temperature measurements, knowing the emissivity of the target surface may not remain constant.

5.1 INTEGRATION OF TERTIARY SCAN HEAD AND PYROMETER

Successful integration of the FMPI and Aconity MIDI+ includes an understanding of any impact the optical path may have on the measurements. Using an integrating sphere (Labsphere, NH, USA), the mirrors used in the scan head for Aconity's processing lasers, and the FMPI, experiments were performed to account for the influence of the mirrors in the optical path of the pyrometer. An image and illustration of the experimental setup is shown in Figure 5.1 and 5.2 respectively.

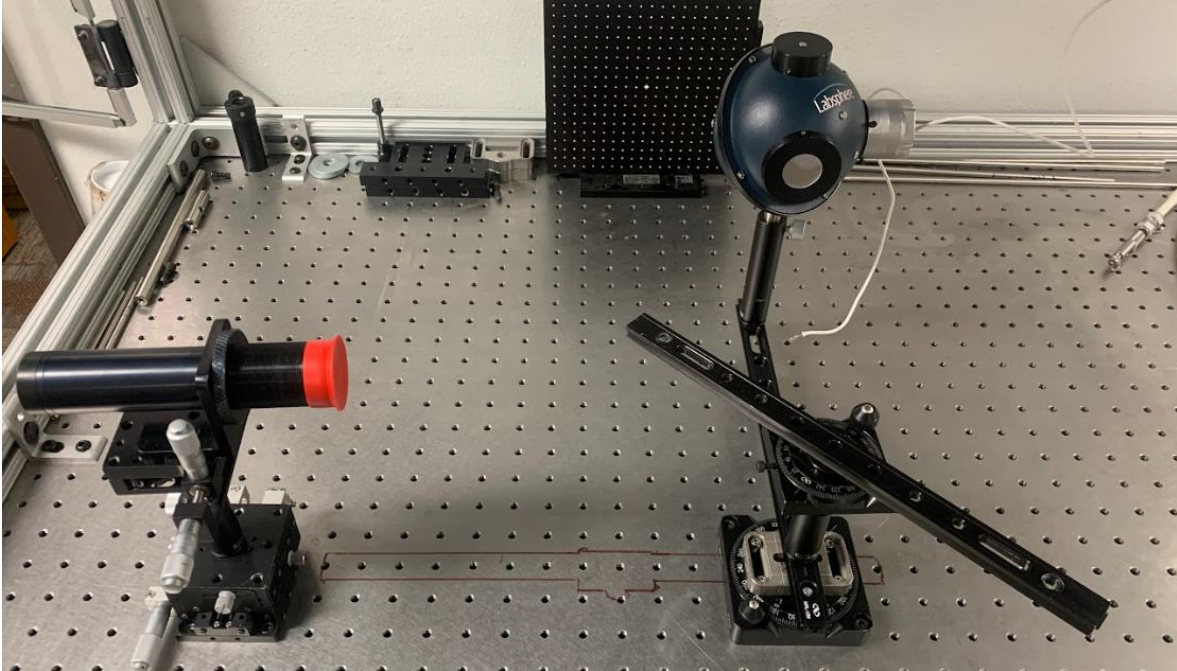


Figure 5.1 Image of mirror reflectivity setup

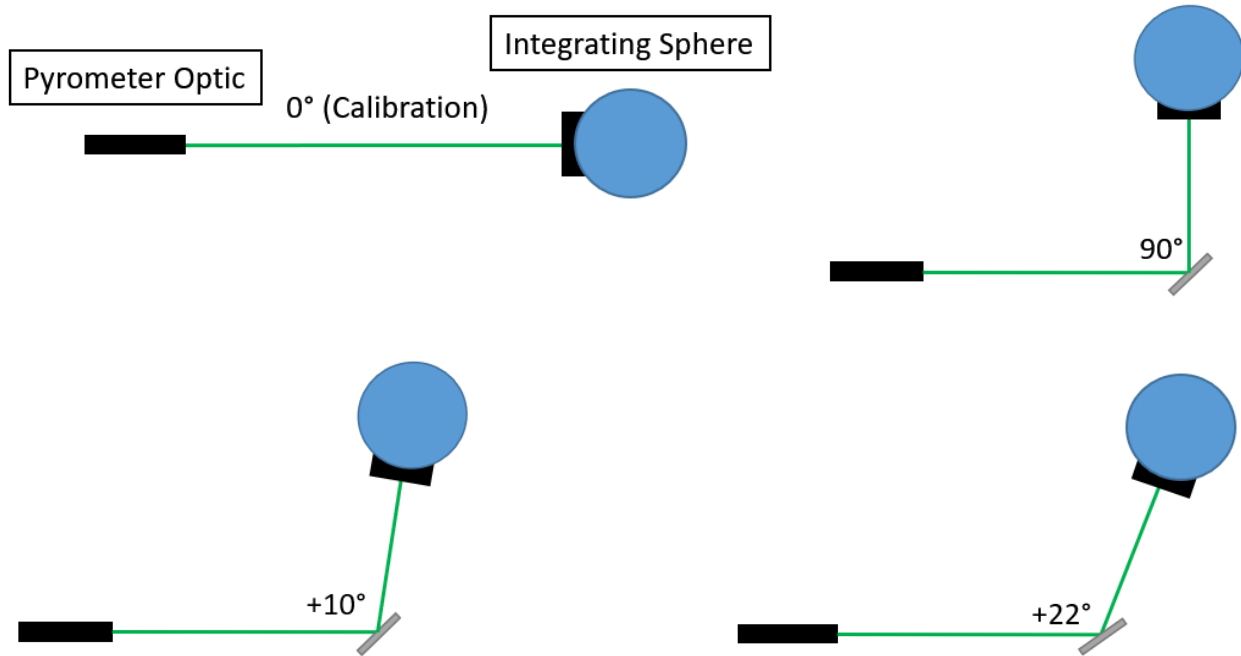


Figure 5.2 Illustration of mirror reflectivity setup

After calibrating the pyrometer and starting at 90° , measurements were taken using the integrating sphere at different angles. The angles at 100° and 112° were chosen to encompass the range of

angles the scan head can reach during processing. The results of the measured intensity are shown in Figure 5.3.

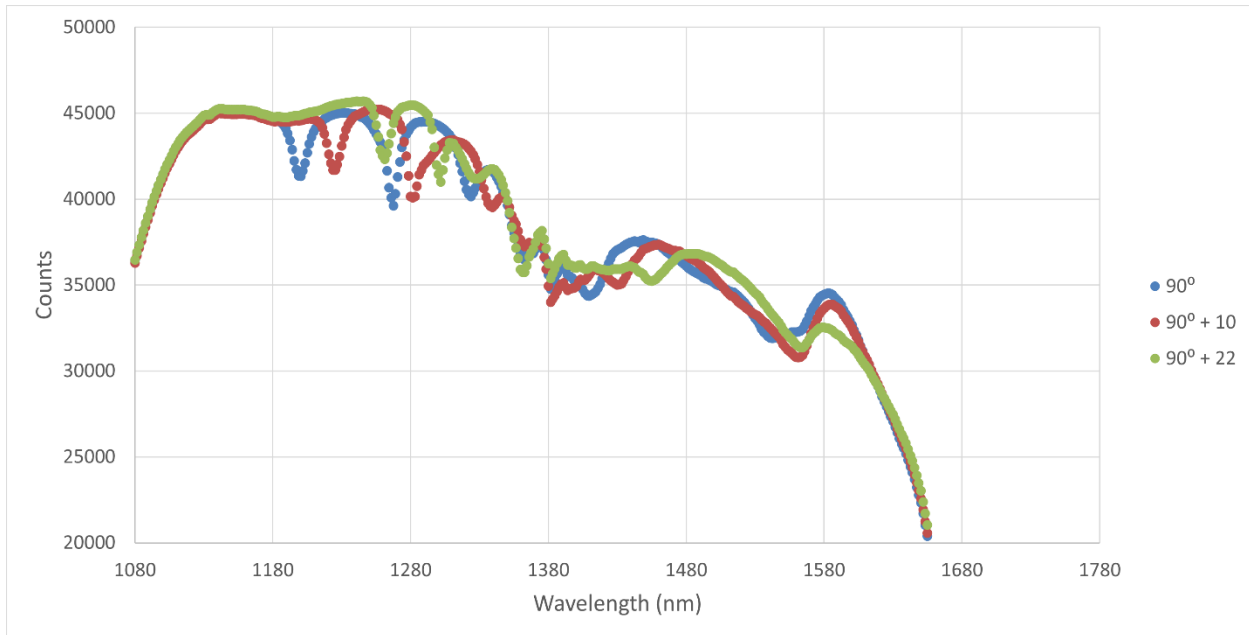


Figure 5.3 Plot of counts v wavelength with mirror at different angles

The results suggested that the intensity captured by the pyrometer was affected by the mirror itself, along with the angle at which measurements are taken. Typically, mirrors are coated with aluminum or silver depending on their applications and cost; silver and aluminum have a solar reflectance of 95% and 91% respectively (Boccas et al., 2006). Similarly, the solar reflectance of mirrors vs. light angle of incidence shows a dependency on angle for Al coated mirrors while the solar reflectance of Ag remains independent of incident angle (Grosjean et al., 2021). The experiment was then replicated with mirrors that had a custom silver coating (Thorlabs, Inc. NJ, USA). The results of the experiment with the custom silver-coated mirrors are shown in Figure 5.4 and an illustration of the experimental setup is shown in Figure 5.5.

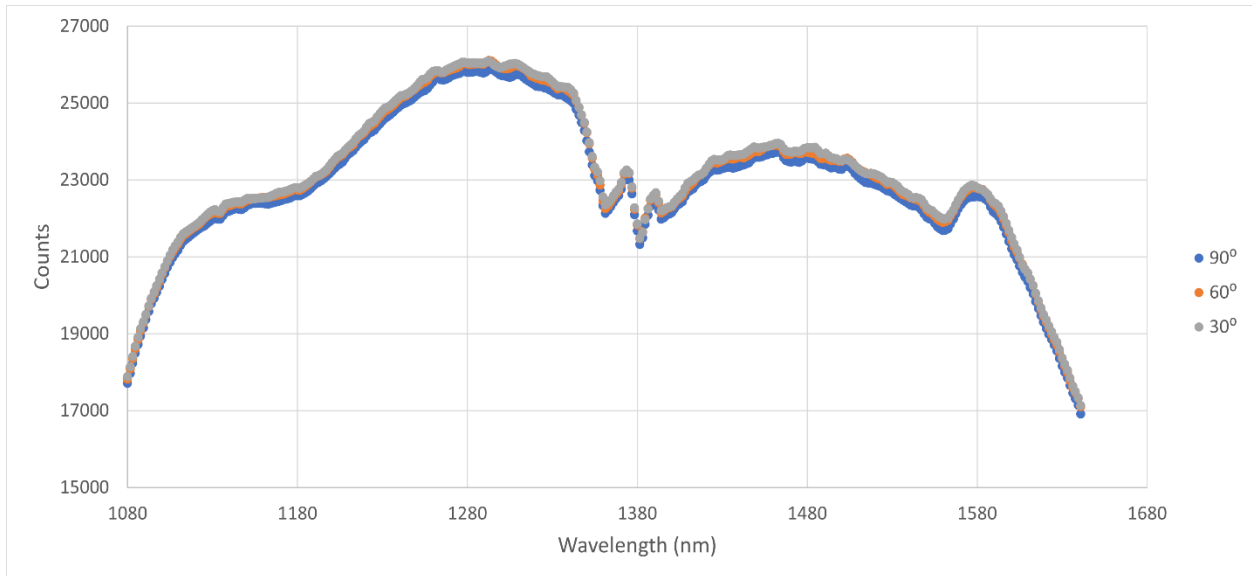


Figure 5.4 Plot of counts v wavelength with custom coating mirrors at different angles

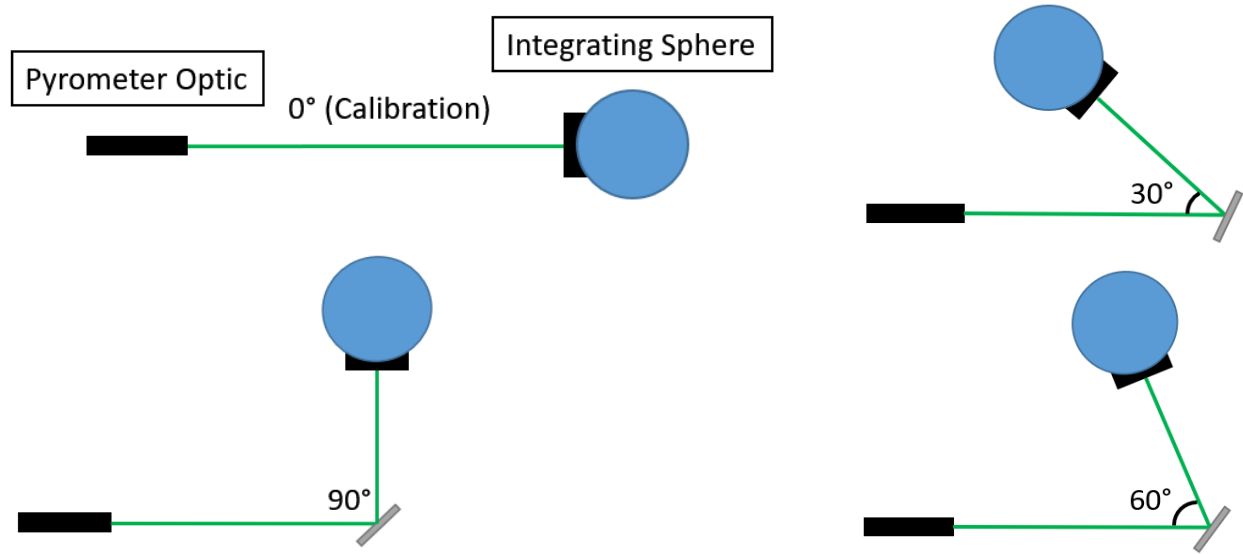


Figure 5.5 Illustration of experimental setup with mirror at different angles

The results show the custom coated mirrors capture the same intensity (counts) at each of the angles tested. With the understanding that the original mirrors have an angular-dependent reflectivity response across the pyrometer’s spectrum, a custom scan head (RAYLASE, GmbH) with custom silver-coated mirrors (Thorlabs, Inc. NJ, USA) was used to include all components

of a typical processing scan head without the laser, to also include a circular opening in the back plate large enough for the FMPI optic to fit through.

Next, the FMPI optic needed to be affixed to the scan head and incapable of moving from the position at which it is to be calibrated. To achieve this, a fixture was designed using Fusion 360 with the first consideration of maintaining laser safety precautions. Using a CAD of the scan head provided by the manufacturer, two openings are highlighted in Figure 5.6.

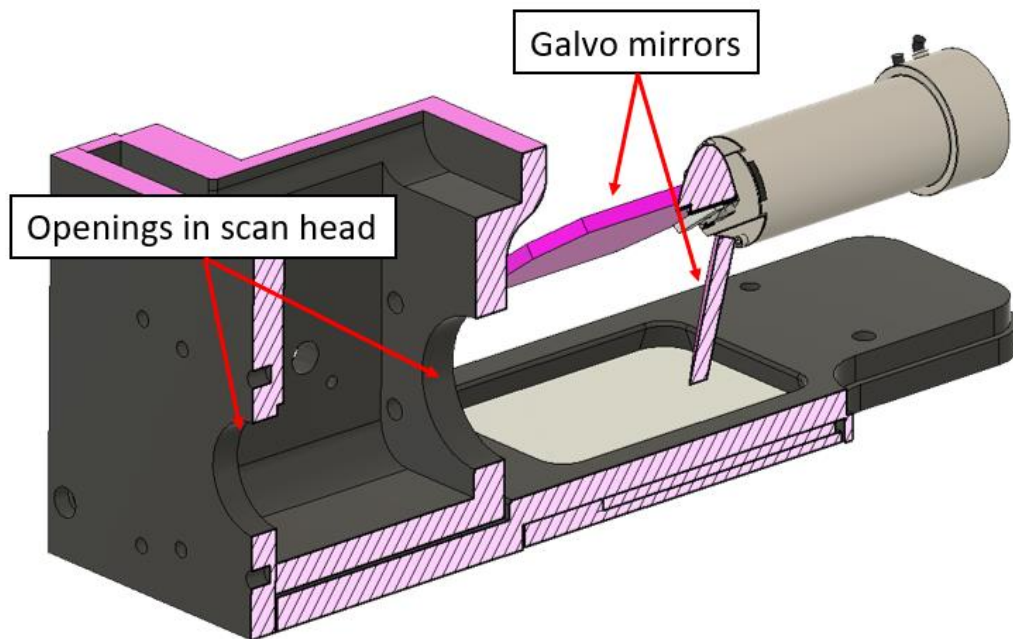


Figure 5.6 CAD of scan head highlighting openings

To account for these, the fixture was designed such that it would create a seal around the opening closest to the galvo mirrors and an enclosed space for the pyrometer optic to be fed through the outermost opening to protect from any stray light coming from the build chamber or through the initial seal. A CAD showing the backplate removed to illustrate where the fixture would be bolted onto is shown in Figure 5.7.

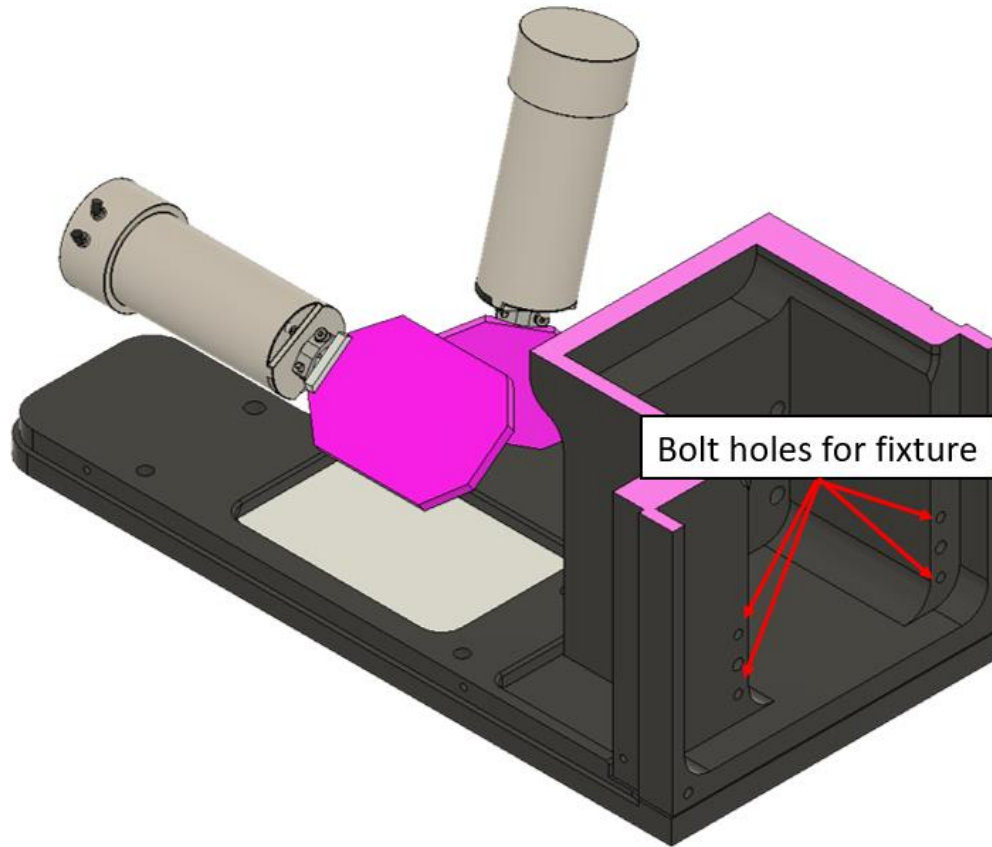


Figure 5.7 CAD of scan head w/ back plate removed

The optic then had to be aligned with the center of the fixture and stationary from its original calibration alignment so threads were added to the inside of the fixture to have the optic mechanically aligned within it. Finally, threads were added to the end of the fixture for an extension tube from Thorlabs (Thorlabs, NJ, USA) that spectral filters could be placed within knowing that the processing laser is a $1070\text{nm} \pm 10\text{nm}$ fiber laser and the pyrometer operates from $1080\text{nm} - 1640\text{nm}$, so measurements may be impacted by the laser or its reflections within the chamber. The final design and CAD of the FMPI fixture is shown in Figure 5.8 while Figures 5.9 and 5.10 show it fully assembled to the scan head.

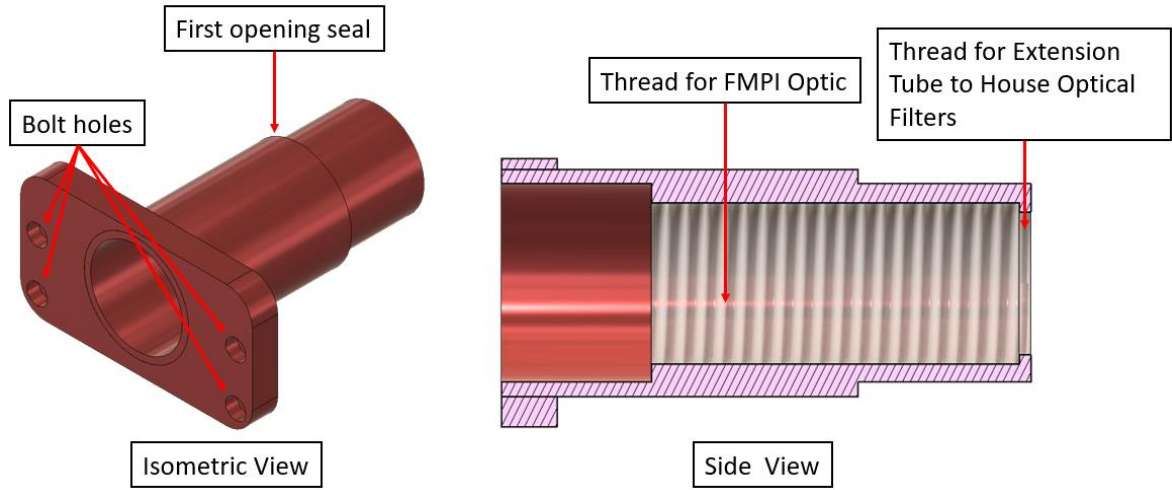


Figure 5.8 CAD of final design of FMPI optic fixture

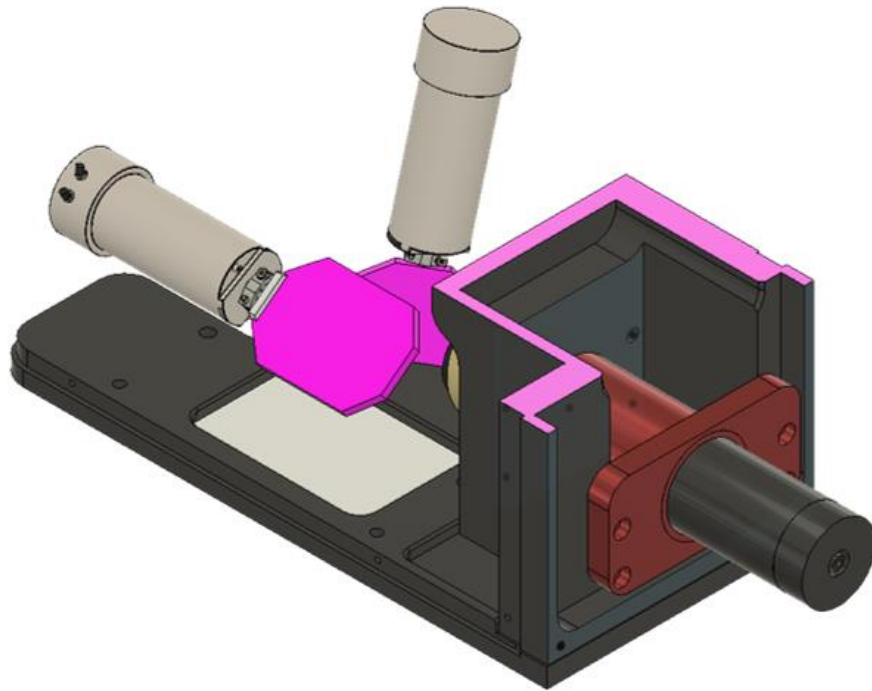


Figure 5.9 CAD of fully assembled fixture with scan head

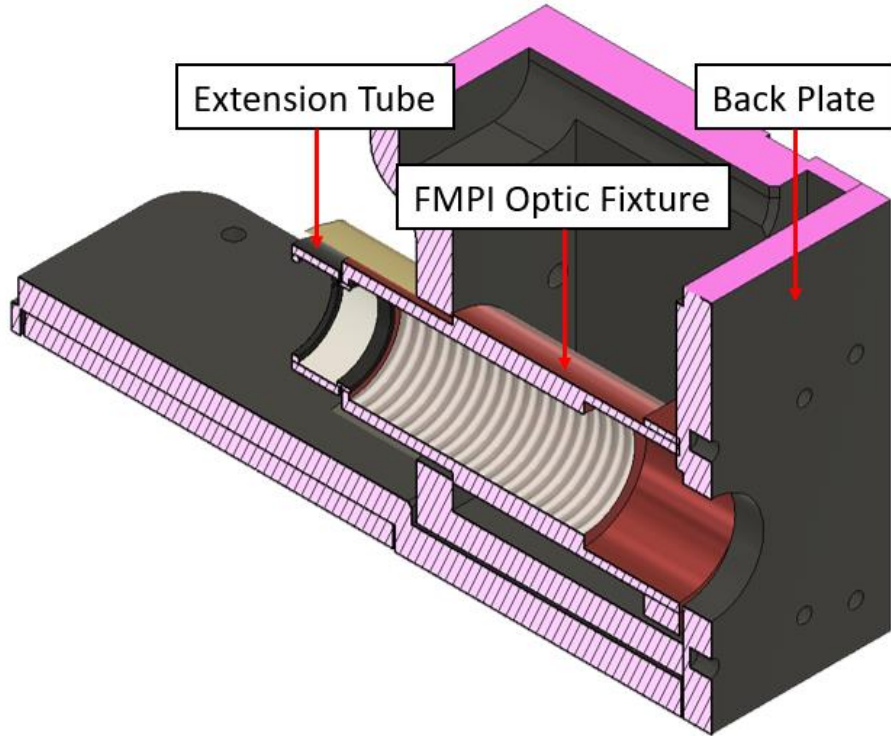


Figure 5.10 Fully assembled FMPI fixture with labels

The fixture was ultimately machined out of aluminum and as two separate bodies to be threaded together for ease of machinability, although it could be made as one continuous piece. The separate components and how they are attached is shown in Figure 5.11.

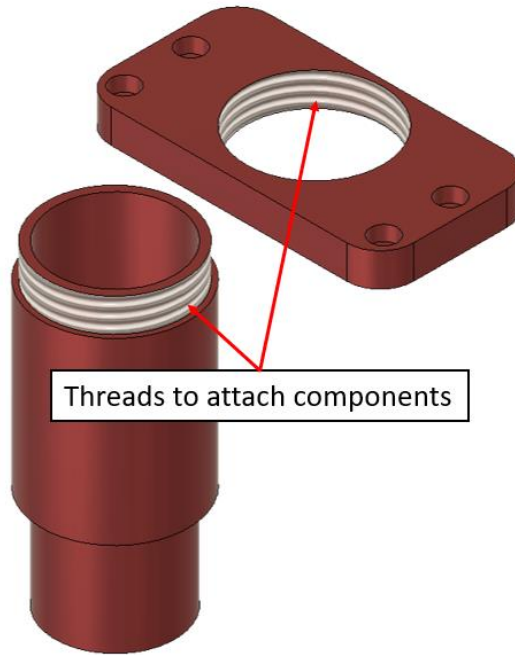


Figure 5.11 CAD of individual FMPI optic fixture components

Once designed and fabricated using aluminum, the fixture was installed upon receiving the scan head with the included custom mirrors. Images of the scan head before and after the installation of the fixture and optic are shown below.

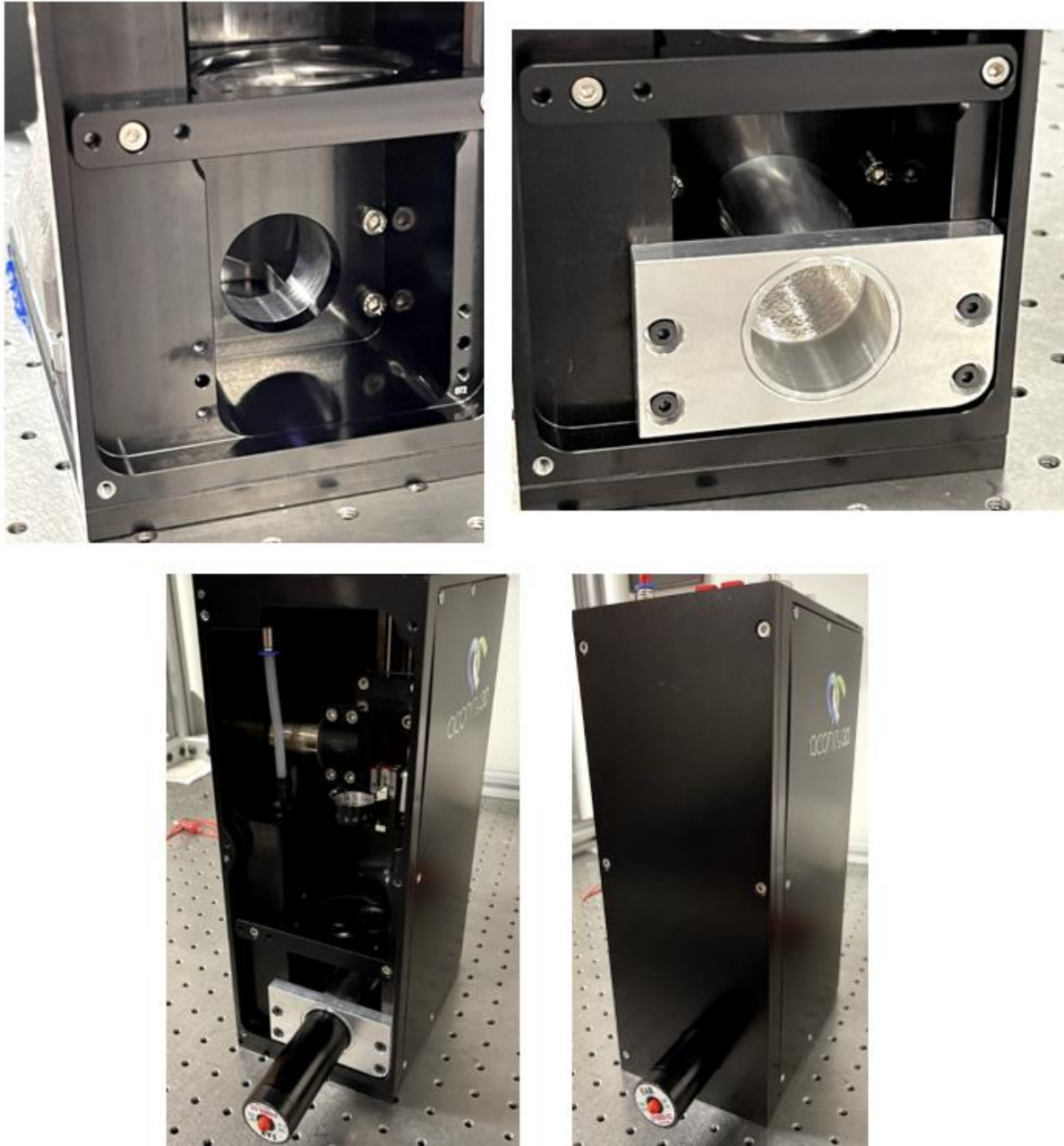


Figure 5.12 Images showing installation of FMPI optic fixture into custom scan head

With this designed fixture, the optic can be interchanged, the fixture can be removed, and extension tubes can be placed with filters in the optical path of the FMPI. Once installed to the machine, the FMPI needed to be calibrated through several obstacles including filters, mirrors, and glasses of

the L-PBF machine to account for any loss in intensity. A calibration technique is described in the next section.

5.2 CALIBRATION

To maintain the accuracy and integrity of the data, a calibration technique was developed for the setup. A similar calibration setup is derived from the technique previously described in section 3.5. An illustration and image of the calibration setup are shown in Figure 5.13.

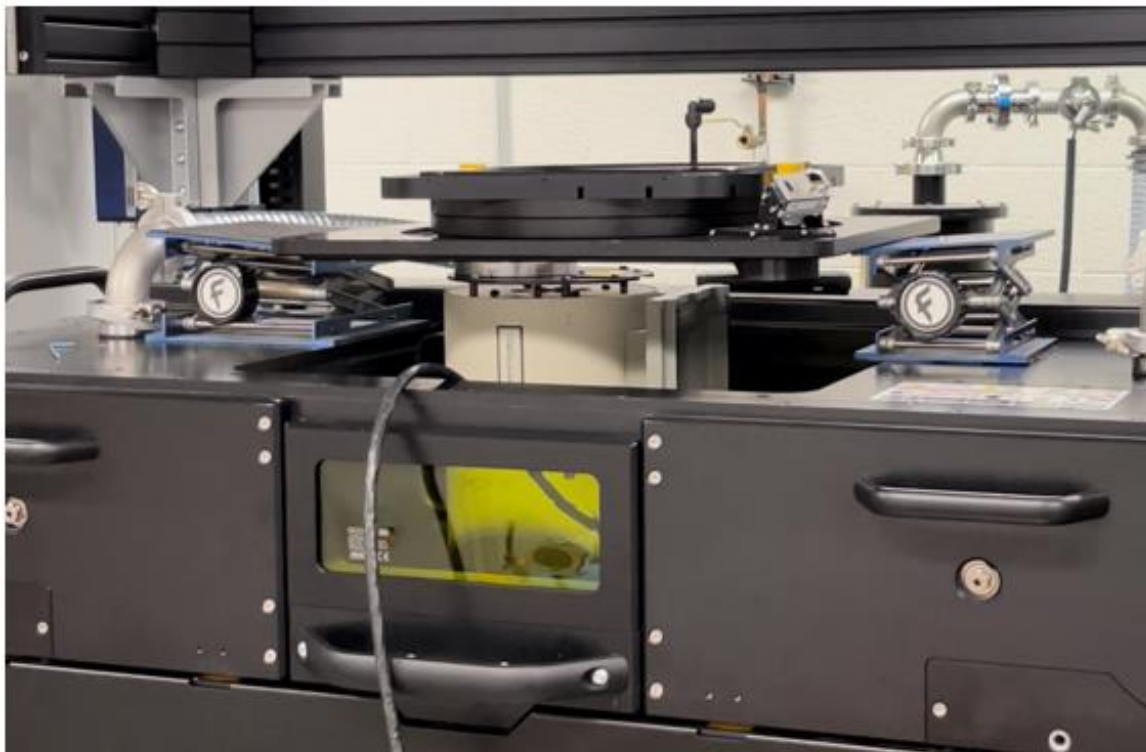
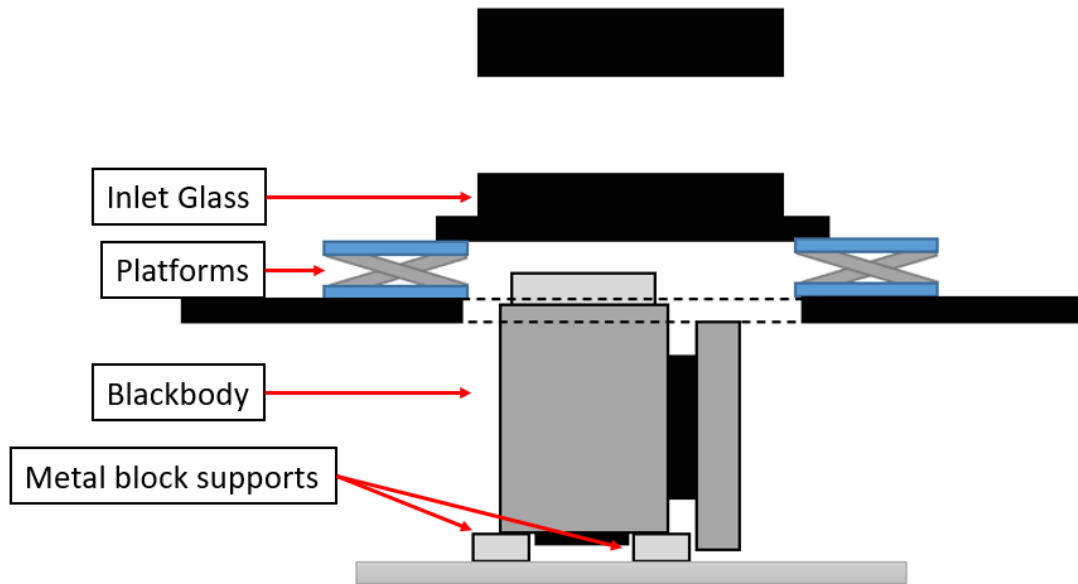


Figure 5.13 Illustration and image of calibration being performed within Aconity MIDI+

Once the blackbody was set up within the build chamber it was set to 1,000°C. The inlet glass was placed above the blackbody source, leveled, then calibrated through the mirrors and optically transmissive glasses that are within the machine. The same calibration technique could then be

performed with optical filters in place. An improvement to be made for a repeatable calibration technique was considered to include blocks of metal with the same dimensions to be placed around the opening to hold the glass at the same height for each calibration.

5.3 DEMONSTRATION OF DATA ACQUISITION

Lastly, to demonstrate the wave band the 1064nm notch filter (Edmund Optics, NJ, USA) works within the calibration process previously described was performed with the filter placed within the extension tube housing and without purging the machine (ie. ambient environment within the chamber). The .DAT file for the calibration was plotted in Excel and shown in Figure 5.14 and a close-up of the results around 1080nm is shown in Figure 5.15.

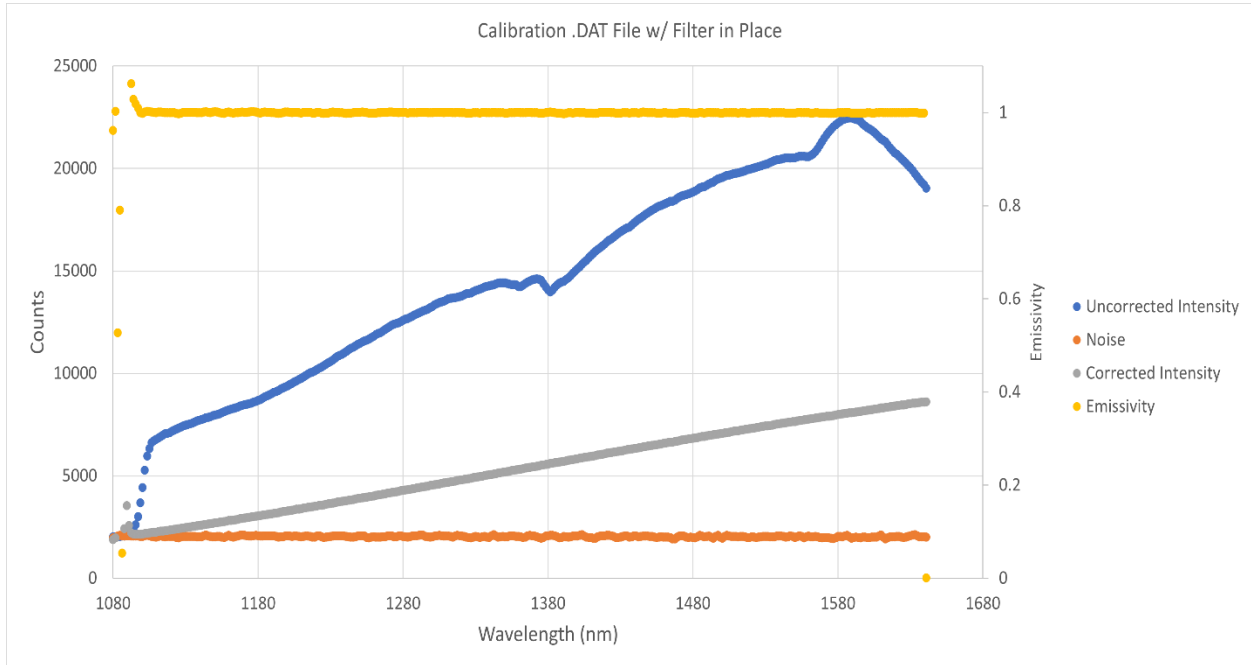


Figure 5.14 .DAT file from calibration with notch filter in place

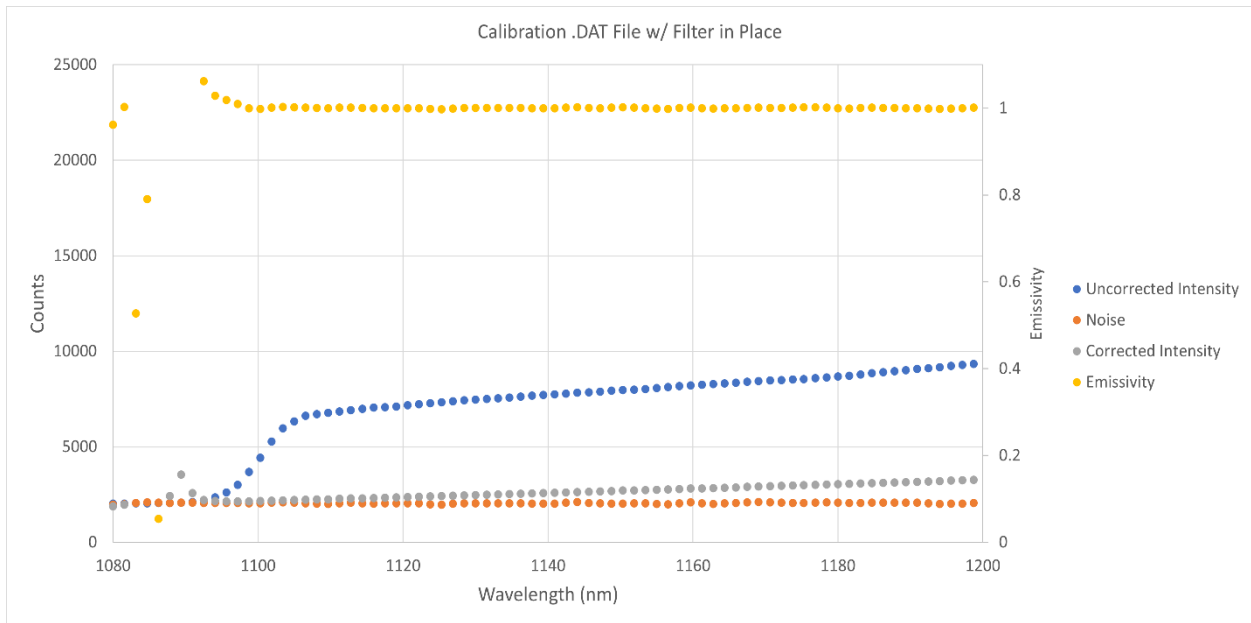


Figure 5.15 Close-up of .DAT file at 1080nm

The peak between 1340nm to 1425nm is the result of the calibration performed in atmosphere and highlights environmental absorption effects due to the presence of humidity (Fowle et al., 1915).

The results indicated the notch filter reduces emissions from the blackbody source up until about 1100nm where they begin to be acquired by the pyrometer. Furthermore, experiments were performed using the same calibration setup but to include laser exposures of a 3mm diameter circle on a plate of Ti-6Al-4V while the pyrometer was aimed coincident with the laser as it is shown in Figure 5.16.

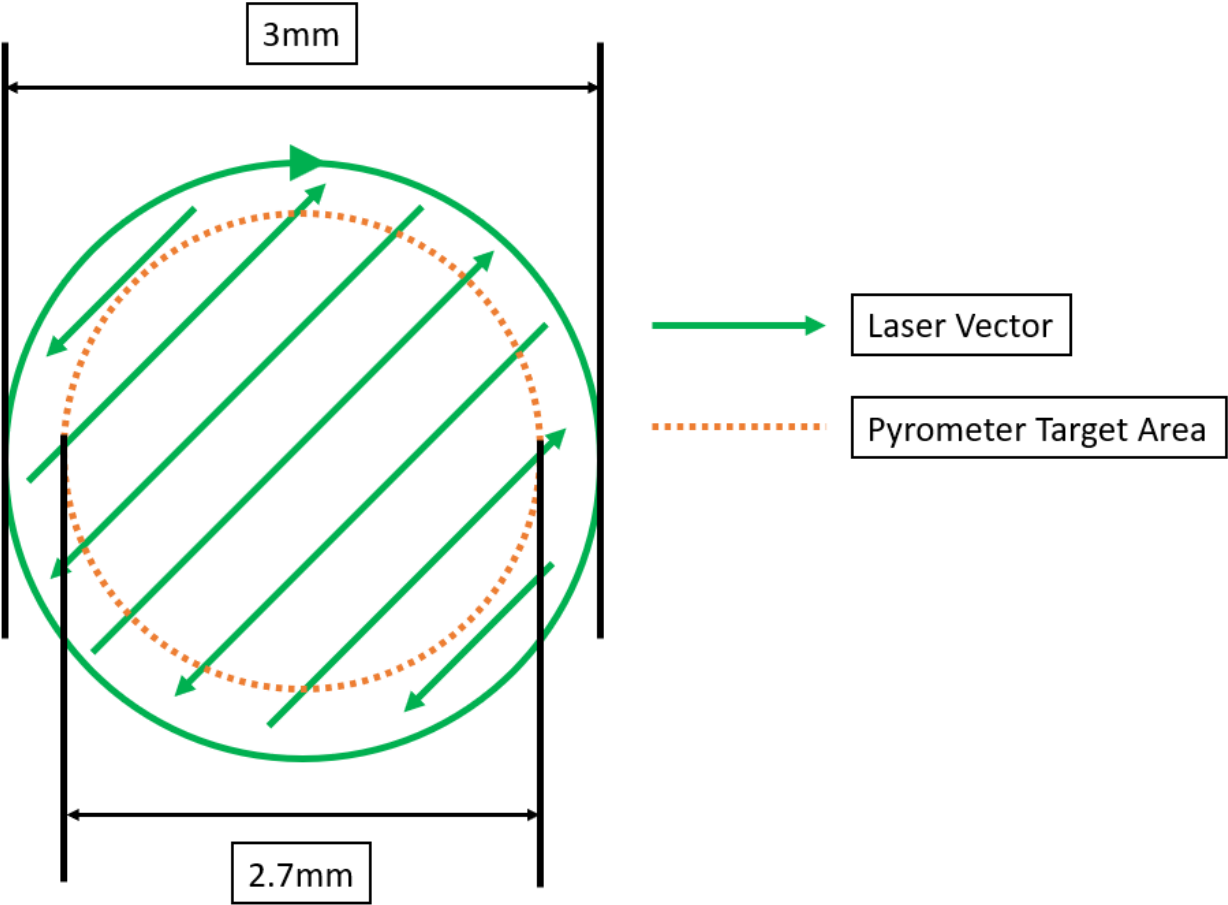


Figure 5.16 Illustration of experiment scan strategy

Laser exposures at 1000W and 1700mm/s were performed in succession (60 layers) and the .DAT files for different temperatures are shown in Figure 5.16 – 5.18.

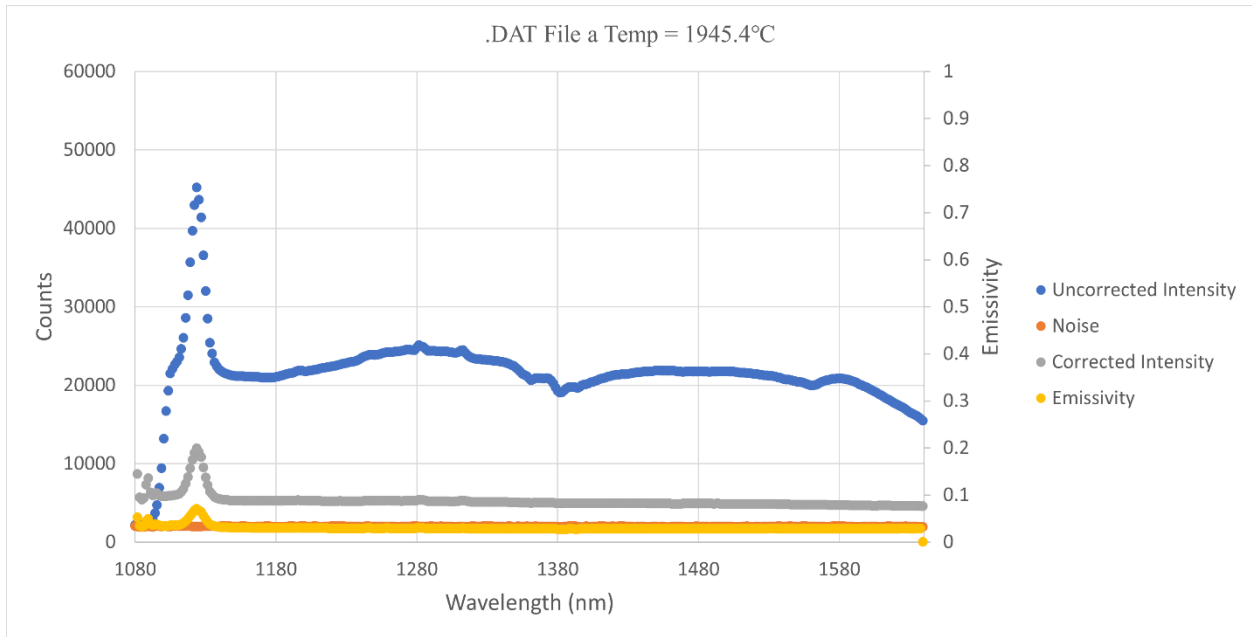


Figure 5.17 Plotted .DAT file of laser experiment at ~1945°C

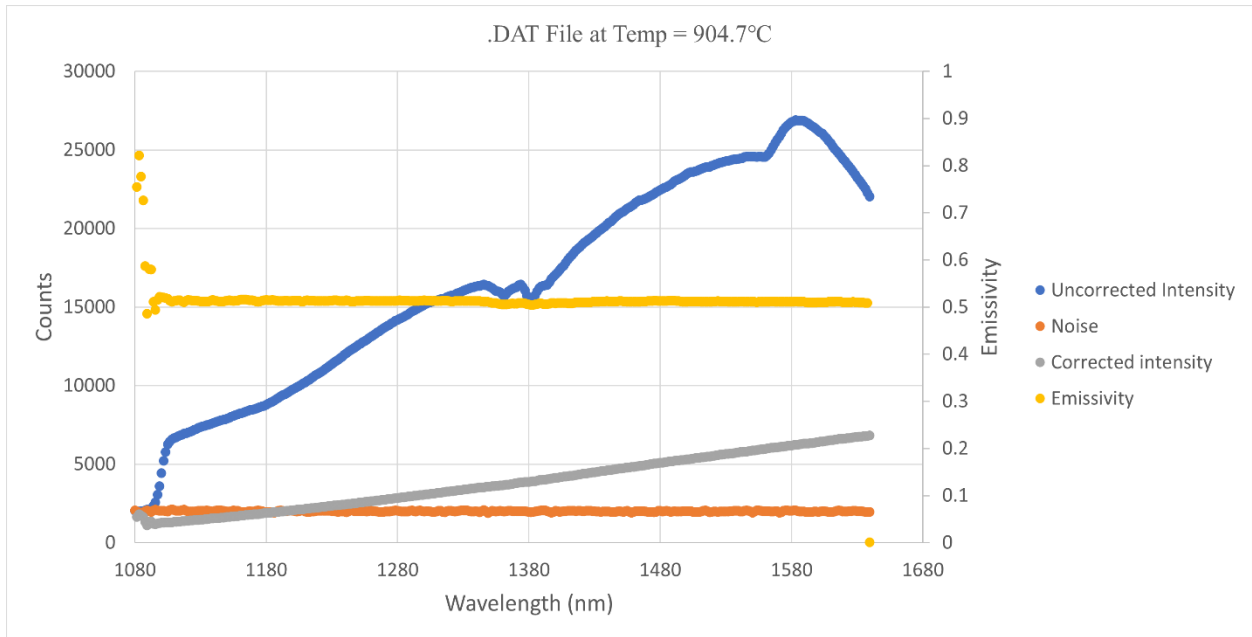


Figure 5.18 Plotted .DAT file of laser experiment at ~905°C

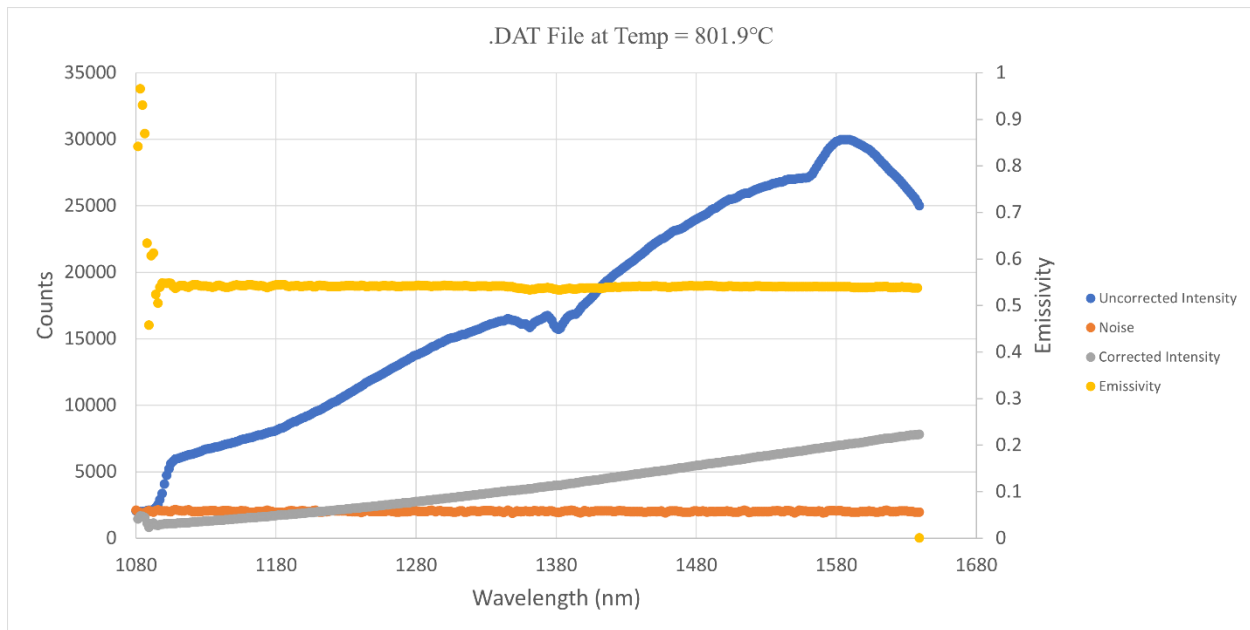


Figure 5.19 Plotted .DAT file of laser experiment at ~802°C

The results from Figure 5.16 suggest that the laser was influencing the results at that time still due to the uncorrected intensity gathered by the pyrometer peaking at ~1124nm rather than at ~1580nm like the results from Figures 5.17 and 5.18, both of which are to be expected from Planck’s Law. Although the laser was influencing the results initially, the results from Figures 5.17 and 5.18 had the same trend in uncorrected intensity as Figure 5.14 that showed the calibration’s .DAT file increasing passed ~1100nm indicating the notch filter was capable of reducing some of the emissions. However, more of the same filters will likely need to be used to reduce the emissions of the laser further to the point they will not produce a .DAT file (<20,000 counts). While filters are an option to mitigate sources of influence, the software can eliminate wavelengths it uses for the temperature calculations by not considering the intensity captured in wavelengths outside of the limit set. This is considered to be a more convenient and cost-free approach to eliminating the influence and will likely be the preferred approach when capturing measurements in-situ. Future experiments will include using an induction heater within the Aconity MIDI+ that can reach

temperatures up to 1,000°C to check the accuracy of the temperature measurements the pyrometer produces. The work in the Aconity MIDI+ is an ongoing effort to capture accurate temperature measurements in-situ. The results presented show promise in its integration thus far and the research presented in this thesis is a contributing factor to its progress in understanding the emissive behavior of metal AM powders. The apparent graybody behavior of Inconel 718 powder implies the accurate use of other non-contact temperature measurement modalities such as two-color pyrometry in which a graybody assumption is necessary. Furthermore, combining the use of the FMPI and other non-contact temperature measurement devices could lead to a real-time calibration or “tolerance” metric of other devices in which the emissivity is necessary for an accurate temperature measurement.

PCHAPTER 6: CONCLUSIONS AND RECOMMENDATIONS

This chapter provides the conclusions of the measurements captured from the methodology presented and recommendations for both future work and in producing accurate temperature measurements. This research considered potential influential factors on measurements such as environmental radiation and target surface, and statistical analysis of results being that there is no previous knowledge or database to be referred to. The research presented highlights the need for further exploration into the emissive behavior of metal powders and a need for the understanding of the environment within which the target is being monitored.

6.1 CONCLUSIONS

The emissivity values presented and the methodology described were analyzed statistically and compared to the TPRC as there is no published source of information on the emissivity of metal powders specifically. The results of the average emissivity for PSD – 1 was approximately 0.50 and for PSD – 2 and PSD – 3 it was approximately 0.54, all of which were found to be higher than those published in the TPRC for “as-received” Inconel 718 which reports an emissivity at 1500nm between 0.35 and 0.45 for 250°C to 750°C. Work done by Boley et al. 2015 refers to absorption coefficients of metals generally increasing with temperature, but often being limited to normal incidence and found to substantially increase when considering metal powder. The TPRC also published emissivity values for “sandblasted” Inconel 718 and although they are not reported for 1500nm, the values at 2000nm for 482°C and 649°C were 0.35 and 0.4 respectively. The values for “electropolished” were 0.2 and 0.3 for the same temperatures and wavelength. The “electropolished” sample has a variation of 0.1 between the range of temperatures while the “sandblasted” sample has a variation of 0.05. This is important as it seems as though the rough surface exhibits a greater independence from temperature. The powder sample surface is akin to a

rough surface, likely suggesting the same trend found with rough surfaces in the TPRC; the powder surface is essentially behaving as a rough surface, and the statistical analysis furthermore suggests the emissivity is independent of temperature. The size distribution of powder spheres and geometry affects the absorption values in that larger spheres of powder on the periphery of small spheres resulting in greater reflections and increased absorption, while a more uniform distribution of powder diameters lends itself to fewer reflections and decreased absorption (Boley et al., 2015). Referring to the particle size distribution analysis performed on the powders and shown in section 4.4, PSD – 1 was found to have a more uniform distribution of powder diameters than PSD – 2 or PSD – 3. Statistical analysis suggested a lack of substantial evidence to suggest the emissivity of PSD – 1 was statistically similar to PSD – 2 and PSD – 3 while the two latter were found to be similar. This is a similar finding to that published in which the uniformity of the powder distribution in PSD – 1 led to a lower emissivity of 0.5 compared to 0.54 for PSD – 2 and PSD – 3. While the variances between the apparent and tap density sample preparation methods were not found to be statistically different, the means were. The tap density sample preparation method mean was found to be only 0.02 higher than that of the apparent density which is expected to be a result of the compaction of the powder for tap density along with not considering the channels within the apparent density sample preparation to be a direct contribution to the “surface roughness” but merely akin to “waviness” which is excluded in surface roughness measurements. Temperature also was not found to have an impact on the measurements; however, the measurements taken at 400°C were found to be higher by ~5.5% and likely attributed to the thermal conductivity of the crucible but still able to be related to measurements at 500°C and 600°C as it was shown in the linear regression test. The apparent density for PSD – 1, as reported by the manufacturer, is $4.74\text{g}/\text{cm}^3$ and the apparent density for PSD – 2 and PSD – 3 are $4.86\text{g}/\text{cm}^3$

and 4.75g/cm^3 respectively. Despite similar density to PSD – 3, PSD – 1 was limited in its thermal conductivity by its distribution, unable to compensate for the gaps between particles due to its uniformity in diameters unlike PSD – 3 which has a range from 45 - 150 μm and a greater distribution as is seen in the CAMSIZER X2 results in section 4.4. The emissivity was found to deviate by <0.02 at larger wavelengths than the central wavelength of the pyrometer (1500nm) for all temperatures. At 400 $^{\circ}\text{C}$, the emissivity deviated by as much as 0.8 between 1500nm and 1080nm. However, at 600 $^{\circ}\text{C}$, the deviation changed to <0.02 between 1500nm and 1080nm. This is likely due to the shift in the intensity peak as the powder is heated. This finding highlights the graybody behavior of Inconel 718 and likely other metal AM powders in which the morphology dominates the emissivity, independent of wavelength or temperature. At 600 $^{\circ}\text{C}$, it is believed that the central wavelength can be assumed equal to the emissivity at 1080nm; however, further verification is needed to say the same for wavelengths of a typical L-PBF processing laser (1064nm) to accurately capture the absorptivity of the powder at those wavelengths.

The significance of the research presented and its impact spans across the AM industry to include the further characterization of metal AM powder, process monitoring, and simulations. A method was developed for the characterization of the spectral emissivity of Inconel 718 powder between the wavelengths of 1080nm and 1640nm and temperatures ranging from 400 $^{\circ}\text{C}$ to 600 $^{\circ}\text{C}$, for which the method can be applied to other alloys. The observed graybody behavior of Inconel 718 between 1080nm - 1640nm and 400 $^{\circ}\text{C}$ - 600 $^{\circ}\text{C}$ would allow research in process monitoring to take advantage of the knowledge to implement thermal radiation thermometry techniques that are emissivity dependent and in the spectral range explored in this work, unto which the values measured and presented here can be input. Also, the spectral emissivity values captured could be used to best simulate the L-PBF process as it has been shown that the absorptivity of metal powder

is different than that of its solid counterpart and current published values of emissivity for metals do not include powder. Absorbance is also commonly referred to in choosing process parameters for L-PBF processing of materials (Brandau et al., 2022). Rather than assuming a trend in absorption or guess-and-check methods, this method provides measurements of emissivity that can yield higher efficiency in process parameter optimization when the emissivity can be approximated to the absorptivity under thermal equilibrium (steady state conditions). Lastly, the integration of a multi-wavelength pyrometer and LPBF machine has potential in obtaining absolute surface temperatures measurements in-situ as the pyrometer produces emissivity-independent temperature measurements and the volatile nature of the process does not allow for assumptions on the emissivity given the dynamics that unfold including fast transitions in phase, chemistry, surfaces, etc. occurring during processing. The methodology presented and described shows promise as being the start of a source of information useful in the additive manufacturing industry. The focus of future work will be to utilize emissivity measurements captured by the method presented for accurate layer-wise temperature measurements via IR camera or other non-contact measurement device capable of outputting temperature with a known emissivity. Similarly, simulations that benefit from absorptivity values could be compared to actual processing results and the accuracy of the measurements further validated.

6.2 RECOMMENDATIONS

For future work, the main recommendations to follow this research can be summarized in the following points:

1. Understand emissive behavior of powder size distributions and alloys to be used in the process.

2. Combine FMPI measurements with process simulations to improve quality and repeatability.
3. Utilize understanding of metal powder emissive behavior for layer-wise, non-contact temperature measurements in PBF (e.g., two-color pyrometry)

The findings presented in this research are a start to a source of information not yet published. More experiments could yield standards to reduce the amount of experiments needed to ensure accurate emissivity (absorptivity) measurements utilizing the FMPI, glovebox, and SiC tube. Although temperatures higher than 600°C could yield benefit in further understanding the emissive behavior of the powder, different methods of heating have not been explored as this could alter the results if reflections or emissions of a heat source are picked up by the pyrometer and so further testing is needed. Improvements to the heater in the form of a new crucible basket filament and redesign of the insulator could yield higher temperatures like those capable of melting Inconel 718, although they have not yet been explored. The apparent graybody behavior of Inconel 718 suggests there may be other metal AM powders exhibiting the same emissive behavior and trends as their morphology dominates their emissivity. Future work will explore other alloys and their behavior using the FMPI to exploit the trends in such a way that accurate in-situ temperature measurements can be captured. This research has laid the groundwork for advancing our understanding of emissivity in powder-based AM processes. As the emissive behavior of various metal AM powders and their morphological influences is explored, future work will strive to develop reliable in-situ temperature measurements, ultimately contributing to the optimization of additive manufacturing processes by building upon these initial findings to help shape the future of this rapidly evolving industry.

REFERENCES

- Abdulhameed, O., Al-Ahmari, A., Ameen, W., & Mian, S. H. (2019). Additive manufacturing: Challenges, trends, and applications. *Advances in Mechanical Engineering*, *11*(2), 1–27.
https://doi.org/10.1177/1687814018822880/ASSET/IMAGES/LARGE/10.1177_1687814018822880-FIG2.JPEG
- Alkahari, M. R., Furumoto, T., Ueda, T., Hosokawa, A., Tanaka, R., & Abdul Aziz, M. S. (2012). Thermal conductivity of metal powder and consolidated material fabricated via selective laser melting. *Key Engineering Materials*, *523–524*, 244–249.
<https://doi.org/10.4028/WWW.SCIENTIFIC.NET/KEM.523-524.244>
- Alvarez, A. (2002). *Subtractive Manufacturing: Past, Present, and Future* | KETIV.
<https://ketiv.com/blog/subtractive-manufacturing-past-present-and-future/>
- Attaran, M. (2017). The rise of 3-D printing: The advantages of additive manufacturing over traditional manufacturing. *Business Horizons*, *60*(5), 677–688.
<https://doi.org/10.1016/J.BUSHOR.2017.05.011>
- Balat-Pichelin, M., Sans, J. L., Bêche, E., Flaud, V., & Annaloro, J. (2017). Oxidation and emissivity of Inconel 718 alloy as potential space debris during its atmospheric entry. *Materials Characterization*, *127*, 379–390.
<https://doi.org/10.1016/J.MATCHAR.2017.02.016>
- Balbaa, M. A., Ghasemi, A., Fereiduni, E., Elbestawi, M. A., Jadhav, S. D., & Kruth, J. P. (2021). Role of powder particle size on laser powder bed fusion processability of AlSi10mg alloy. *Additive Manufacturing*, *37*.
<https://doi.org/10.1016/J.ADDMA.2020.101630>

- Barreira, E., Almeida, R. M. S. F., & Simões, M. L. (2021a). Emissivity of Building Materials for Infrared Measurements. *Sensors 2021, Vol. 21, Page 1961, 21(6)*, 1961. <https://doi.org/10.3390/S21061961>
- Barreira, E., Almeida, R. M. S. F., & Simões, M. L. (2021b). *Emissivity of Building Materials for Infrared Measurements*. <https://doi.org/10.3390/s21061961>
- Bass, M., Stryland, E. W. Van, Williams, D. R., & Wolfe, W. L. (1995). *Handbook of Optics Volume II Devices, Measurements, and Properties 2nd edition*. <https://ui.adsabs.harvard.edu/abs/1995hop2.book.....B/abstract>
- Bayle, F., & Doubenskaia, M. (2008). *Selective laser melting process monitoring with high speed infra-red camera and pyrometer*. 698505-698505–698508. <https://doi.org/10.1117/12.786940>
- Bergman, T. L., Lavine, A. S., Incropera, F. P., & DeWitt, D. P. (2011). *Introduction to Heat Transfer* (6th ed.). John Wiley & Sons.
- Berumen, S., Bechmann, F., Lindner, S., Kruth, J. P., & Craeghs, T. (2010). Quality control of laser- and powder bed-based Additive Manufacturing (AM) technologies. *Physics Procedia*, 5(PART 2), 617–622. <https://doi.org/10.1016/J.PHPRO.2010.08.089>
- Bhatia, A., & Sehgal, A. K. (2021). Additive manufacturing materials, methods and applications: A review. *Materials Today: Proceedings*. <https://doi.org/10.1016/J.MATPR.2021.04.379>
- Bikas, H., Stavropoulos, & P., & Chryssolouris, G. (2016). *Additive manufacturing methods and modelling approaches: a critical review*. <https://doi.org/10.1007/s00170-015-7576-2>

- Boccas, M., Vucina, T., Araya, C., Vera, E., & Ahhee, C. (2006). Protected-silver coatings for the 8-m Gemini telescope mirrors. *Thin Solid Films*, 502(1–2), 275–280.
<https://doi.org/10.1016/j.tsf.2005.07.295>
- Boley, C. D., Khairallah, S. A., & Rubenchik, A. M. (2015). Calculation of laser absorption by metal powders in additive manufacturing. *Applied Optics*, 54(9), 2477.
<https://doi.org/10.1364/AO.54.002477>
- Brandau, B., Da Silva, A., Wilsnack, C., Brueckner, F., & Kaplan, A. F. H. (2022). Absorbance study of powder conditions for laser additive manufacturing. *Materials and Design*, 216. <https://doi.org/10.1016/J.MATDES.2022.110591>
- Britannica, T. E. of E. (2020). *Planck's radiation law | Definition, Formula, & Facts | Britannica*. <https://www.britannica.com/science/Plancks-radiation-law>
- Campbell, I., Bourell, D., & Gibson, I. (2012). *Additive manufacturing: rapid prototyping comes of age*. <https://doi.org/10.1108/13552541211231563>
- Campbell, I., Diegel, O., Kowen, J., Mostow, N., & Wohlers, T. (2022). *Wohlers Report 2022*.
- Cengel, Y. A. (2007). *Heat and Mass Transfer: A Practical Approach* (3rd ed.). McGraw-Hill.
- Cengel, Y. A., & Ghajar, A. (2014). *Heat and Mass Transfer: Fundamentals and Applications* (5th ed.). McGraw Hill.
- Chivel, Y., & Smurov, I. (2010). *On-line temperature monitoring in selective laser sintering/melting*. <https://doi.org/10.1016/j.phpro.2010.08.079>
- Clijsters, S., Craeghs, T., Buls, S., Kempen, K., & Kruth, J. P. (2014). In situ quality control of the selective laser melting process using a high-speed, real-time melt pool

- monitoring system. *The International Journal of Advanced Manufacturing Technology* 2014 75:5, 75(5), 1089–1101. <https://doi.org/10.1007/S00170-014-6214-8>
- Cordero, Z. C., Meyer, H. M., Nandwana, P., & Dehoff, R. R. (2017). Powder bed charging during electron-beam additive manufacturing. *Acta Materialia*, 124, 437–445. <https://doi.org/10.1016/J.ACTAMAT.2016.11.012>
- Craeghs, T., Clijsters, S., Yasa, E., Bechmann, F., Berumen, S., & Kruth, J. P. (2011). Determination of geometrical factors in Layerwise Laser Melting using optical process monitoring. *Optics and Lasers in Engineering*, 49(12), 1440–1446. <https://doi.org/10.1016/j.optlaseng.2011.06.016>
- DeWitt, D. P., & Nutter, G. D. (1988). *Theory and practice of radiation thermometry*. Wiley. <https://www.wiley.com/en-us/Theory+and+Practice+of+Radiation+Thermometry-p-9780471610182>
- Felice, R. A. (2002). *The Spectropyrometer-a Practical Multi-wavelength Pyrometer*. www.pyrometry.com
- Felice, R. A. (2004). Multispectral expert system spectropyrometer and its uses in industry and research. <https://doi.org/10.1117/12.547800>, 5405, 36–47. <https://doi.org/10.1117/12.547800>
- Fernandez, A., Felice, R., Terrazas-Nájera, C. A., & Wicker, R. (2021). Implications for accurate surface temperature monitoring in powder bed fusion: Using multi-wavelength pyrometry to characterize spectral emissivity during processing. *Additive Manufacturing*, 46. <https://doi.org/10.1016/J.ADDMA.2021.102138>
- Forrest, E. C., & Murphy, R. D. (2016). *A Review of In-situ Temperature Measurements for Additive Manufacturing Technologies*. <https://www.osti.gov/servlets/purl/1373235>

- Fowle, F. E., Fowle, & E., F. (1915). The Transparency of Aqueous Vapor. *ApJ*, 42(2), 394.
<https://doi.org/10.1086/142220>
- Gibson, I., Rosen, D., Stucker, B., & Khorasani, M. (2021). *Additive Manufacturing Technologies*.
- Grasso, M., & Colosimo, B. M. (2017). *Process defects and in situ monitoring methods in metal powder bed fusion: A review*. <https://doi.org/10.1088/1361-6501/aa5c4f>
- Grosjean, A., Soum-Glaude, A., & Thomas, L. (2021). *Replacing silver by aluminum in solar mirrors by improving solar reflectance with dielectric top layers*.
- Gusarov, A. V., & Kovalev, E. P. (2009). Model of thermal conductivity in powder beds. *Physical Review B - Condensed Matter and Materials Physics*, 80(2).
<https://doi.org/10.1103/PHYSREVB.80.024202>
- Gutknecht, K., Haferkamp, L., Cloots, M., & Wegener, K. (2020). Determining process stability of Laser Powder Bed Fusion using pyrometry. *Procedia CIRP*, 95, 127–132.
<https://doi.org/10.1016/J.PROCIR.2020.01.147>
- Iams, A. D., Gao, M. Z., Shetty, A., & Palmer, T. A. (2022). Influence of particle size on powder rheology and effects on mass flow during directed energy deposition additive manufacturing. *Powder Technology*, 396, 316–326.
<https://doi.org/10.1016/J.POWTEC.2021.10.059>
- ISO - ISO/ASTM 52900:2015 - Additive manufacturing — General principles — Terminology. (2015). <https://www.iso.org/standard/69669.html>
- Kim, H., Lin, Y., & Tseng, T. L. B. (2018). A review on quality control in additive manufacturing. *Rapid Prototyping Journal*, 24(3), 645–669.
<https://doi.org/10.1108/RPJ-03-2017-0048>

- King, J. L., Jo, H., Shahsafi, A., Blomstrand, K., Sridharan, K., & Kats, M. A. (2018). Impact of corrosion on the emissivity of advanced reactor structural alloys. *Journal of Nuclear Materials*, 508, 465–471. <https://doi.org/10.1016/J.JNUCMAT.2018.05.047>
- Manullang, M. C. T., Lin, Y. H., Lai, S. J., & Chou, N. K. (2021). Implementation of Thermal Camera for Non-Contact Physiological Measurement: A Systematic Review. *Sensors (Basel, Switzerland)*, 21(23). <https://doi.org/10.3390/S21237777>
- Markl, M., & Körner, C. (2016). Multiscale Modeling of Powder Bed-Based Additive Manufacturing. *Annual Review of Materials Research*, 46, 93–123. <https://doi.org/10.1146/ANNUREV-MATSCI-070115-032158>
- Newell, D. J., O’Hara, R. P., Cobb, G. R., Palazotto, A. N., Kirka, M. M., Burggraf, L. W., & Hess, J. A. (2019). Mitigation of scan strategy effects and material anisotropy through supersolvus annealing in LPBF IN718. 764. <https://doi.org/10.1016/J.MSEA.2019.138230>
- Paul, S. C., van Zijl, G. P. A. G., & Gibson, I. (2018). A review of 3D concrete printing systems and materials properties: current status and future research prospects. *Rapid Prototyping Journal*, 24(4), 784–798. <https://doi.org/10.1108/RPJ-09-2016-0154/FULL/PDF>
- Pavlov, M., Doubenskaia, M., & Smurov, I. (2010). Pyrometric analysis of thermal processes in SLM technology. *Physics Procedia*, 5(PART 2), 523–531. <https://doi.org/10.1016/J.PHPRO.2010.08.080>
- Price, S., Cheng, B., Lydon, J., Cooper, K., & Chou, K. (2014). On Process Temperature in Powder-Bed Electron Beam Additive Manufacturing: Process Parameter Effects.

Journal of Manufacturing Science and Engineering, Transactions of the ASME,
136(6). <https://doi.org/10.1115/1.4028485/377626>

Rodriguez, E., Mireles, J., Terrazas, C., ... D. E.-A., & 2015, undefined. (n.d.).

Approximation of absolute surface temperature measurements of powder bed fusion additive manufacturing technology using in situ infrared thermography. *Elsevier*.

Retrieved February 7, 2023, from

<https://www.sciencedirect.com/science/article/pii/S2214860414000256>

Rodriguez, E., Mireles, J., Terrazas, C. A., Espalin, D., Perez, M. A., & Wicker, R. B.

(2015). Approximation of absolute surface temperature measurements of powder bed fusion additive manufacturing technology using in situ infrared thermography. *Additive Manufacturing, Complete*(5), 31–39. <https://doi.org/10.1016/J.ADDMA.2014.12.001>

Slack, G. A., Tanzilli, R. A., Pohl, R. O., & Vandersande, J. W. (1987). The intrinsic thermal conductivity of AlN. *Journal of Physics and Chemistry of Solids*, 48(7), 641–647. [https://doi.org/10.1016/0022-3697\(87\)90153-3](https://doi.org/10.1016/0022-3697(87)90153-3)

Taylor, S., Wright, J. B., Forrest, E. C., Jared, B., Koepke, J., & Beaman, J. (2020).

Investigating relationship between surface topography and emissivity of metallic additively manufactured parts. *International Communications in Heat and Mass Transfer*, 115, 104614.

Transfer, 115, 104614.

<https://doi.org/10.1016/J.ICHEATMASSTRANSFER.2020.104614>

Technical Reference - Surface Roughness - IAI America. (n.d.). Retrieved April 19, 2023, from <https://www.intelligentactuator.com/technical-reference-surface-roughness/>

- Thermophysical Properties of Matter - The TPRC Data Series. Volume 7. Thermal Radiative Properties - Metallic Elements and Alloys.* (1970).
<https://apps.dtic.mil/sti/citations/ADA951941>
- Tofail, S. A. M., Koumoulos, E. P., Bandyopadhyay, A., Bose, S., O'Donoghue, L., & Charitidis, C. (2018). Additive manufacturing: scientific and technological challenges, market uptake and opportunities. *Materials Today*, *21*(1), 22–37.
<https://doi.org/10.1016/J.MATTOD.2017.07.001>
- Vallabh, C. K. P., & Zhao, X. (2022). Melt pool temperature measurement and monitoring during laser powder bed fusion based additive manufacturing via single-camera two-wavelength imaging pyrometry (STWIP). *Journal of Manufacturing Processes*, *79*, 486–500. <https://doi.org/10.1016/J.JMAPRO.2022.04.058>
- VHX-7000 User's Manual 1 Before Using the VHX-7000.* (n.d.).
- Vlasea, M. L., Lane, B. M., Lopez, F. F., Mekhontsev, S., & Donmez, M. A. (2015). *Development of powder bed fusion additive manufacturing test bed for enhanced real time process control* (pp. 527–539). <https://www.nist.gov/publications/development-powder-bed-fusion-additive-manufacturing-test-bed-enhanced-real-time>
- Wu, X., Wei, X., Xu, H., He, W., Li, Y., Pei, B., Li, C., & Han, X. (2021). Emissivity measurement based on deep learning and surface roughness. *AIP Advances*, *11*, 85305.
<https://doi.org/10.1063/5.0055415>
- You, D., Hunter, M., Chen, M., & Chow, S. M. (2020). A Diagnostic Procedure for Detecting Outliers in Linear State-Space Models. *Multivariate Behavioral Research*, *55*(2), 231–255. <https://doi.org/10.1080/00273171.2019.1627659>

Zhang, S., Lane, B., Whiting, J., & Chou, K. (2018). *An Investigation into Metallic Powder Thermal Conductivity in Laser Powder Bed Fusion Additive Manufacturing*.

VITA

Emmanuel Levario was born in Las Cruces, New Mexico and raised in El Paso, Texas. Emmanuel graduated high school from Northwest Early College High School with both a high school degree and an Associate of Arts degree. Emmanuel started his Bachelor's in Metallurgical and Materials Engineering at UTEP in the Fall of 2015, graduating in the Fall of 2019. During his undergraduate studies he served as a barista/manager at a local coffee shop in El Paso. As a graduate student, he was given the opportunity to work in the W.M. Keck Center for 3D Innovation, his first internship to date, and his work centered around learning and furthering the pyrometry sector of research in the lab.

Contact Information: elevario2@miners.utep.edu

This thesis was typed by Emmanuel Levario